Summer 8-31-2016

Numerical simulations of dense granular systems with and without cohesive effects

Lenka Kovalcinova
New Jersey Institute of Technology

ABSTRACT

NUMERICAL SIMULATIONS OF DENSE GRANULAR SYSTEMS WITH AND WITHOUT COHESIVE EFFECTS

by
Lenka Kovalcinova

Granular materials are collections of objects ranging from sand grains that form sand piles or even sand castles to collections of large objects such as a group of meteors in outer space. The considered range of sizes of granular particles is such that the effect of thermal fluctuations is not relevant. However, the interaction between the particles may be very complex, involving inelasticity and friction, in addition to repulsive and possibly attractive interaction forces. These interactions that may be history dependent, make the systems that consist of a large number of particles complex to analyze and difficult to understand using analytical methods. For this reason, most of the work in the field of granular mater, including the main part of this Thesis, is carried out using discrete element/molecular dynamics type simulations.

At the beginning of this work, the energy propagation is considered in a stochastic granular chain in one spatial dimension (1D). The main finding here is that the properties of the stochastic noise influences strongly the process of energy propagation. As it is shown, the issue of the importance of order and randomness remains significant as other aspects of dense granular systems are considered.

Next, the various aspects of 2D and 3D granular systems are discussed, with the focus on a dense regime, where the particles are in almost continuous contact. One important property of the considered systems is the presence of force networks, that describe how interactions between the particles are organized spatially, and how they evolve in time. These mesoscale structures are known to be related on one hand to the microscopic properties relevant on the particle scale, and on the other hand to the global properties of considered systems as a whole.

Consideration of dense granular systems using the tools of percolation theory illustrates the complex process by which these systems go through percolation and jamming transitions when exposed to compression. One significant finding is that these two transitions may coincide or not, depending on the properties of the granular particles. Furthermore, there is an important influence of the force threshold considered, tracing back to the properties of underlying force networks. These networks are analyzed by considering their scaling properties with respect to the system size. Contrary to the published results, it is found that the properties of these networks are not universal: in particular, the force networks that form in the systems comprising frictionless particles are found to belong to a different universality class.

Another approach to analysis of force networks involves consideration of topological measures. In this direction, a novel study involving direct comparison of computational results is carried out analyzing experimental data using the tools of persistence homology, and in particular Betti numbers, that allow to quantify the properties of the force networks, and make comparisons directly between experiments and simulations. This comparison is important in order to identify additional features that have to be included in simulations to allow for meaningful comparison with experiments.

Finally, the influence of the nature of particle interaction on the properties of the system as a whole is considered in more detail. In one direction, the systems are considered to consist of particles that interact by either purely repulsive, or by both repulsive and attractive interactions. It is found that additional attractive interaction (that may be due to cohesive effects in wet granular systems) play an important role in determining the source of energy loss in sheared systems. In another direction, the computational results are extended to 3D, and the connection of modeling methods to the measures describing the system as a whole is discussed.

NUMERICAL SIMULATIONS OF DENSE GRANULAR SYSTEMS WITH AND WITHOUT COHESIVE EFFECTS

by
Lenka Kovalcinova

A Dissertation
Submitted to the Faculty of
New Jersey Institute of Technology and
Rutgers, The State University of New Jersey – Newark
in Partial Fulfillment of the Requirements for the Degree of
Doctor of Philosophy in Mathematical Sciences

Department of Mathematical Sciences
Department of Mathematics and Computer Science, Rutgers-Newark

August 2016

APPROVAL PAGE

NUMERICAL SIMULATIONS OF DENSE GRANULAR SYSTEMS WITH AND WITHOUT COHESIVE EFFECTS

Lenka Kovalcinova

Dr. Lou Kondic, Dissertation Advisor — Date
Professor, Department of Mathematical Sciences, NJIT

Dr. Konstantin Mischaikow, Committee Member — Date
Professor, Department of Mathematics, Rutgers University

Dr. Guillaume Bal, Committee Member — Date
Professor, Department of Applied Physics & Applied Mathematics, Columbia University

---

Dr. Denis Blackmore, Committee Member — Date
Professor, Department of Mathematical Sciences, NJIT

Dr. Richard Moore, Committee Member — Date
Associate Professor, Department of Mathematical Sciences, NJIT

BIOGRAPHICAL SKETCH

Author: Lenka Kovalcinova

Degree: Doctor of Philosophy

Date: August 2016

Undergraduate and Graduate Education:

- Doctor of Philosophy in Mathematical Sciences,
  New Jersey Institute of Technology, Newark, NJ, 2016
- Master of Science in Mathematics,
  Comenius University, Slovakia, 2010
- Bachelor of Science in Mathematics,
  Comenius University, Slovakia, 2008

Major: Mathematical Sciences

Presentations and Publications:

L. Kovalcinova, A. Goullet, L. Kondic, "Scaling properties of force networks for compressed particulate systems," *Physical Review E*, Vol. 93, pp 042903, 2016.

L. Kovalcinova, A. Goullet, L. Kondic, "Percolation and jamming transitions in particulate systems with and without cohesion," *Physical Review E*, Vol. 92, pp 032204, 2015.

L. Kovalcinova, "Importance of topological measures in describing sheared granular systems," *Invited Talk at AMS Sectional Meeting*, Rutgers University, New Brunswick, New Jersey, November 2015

L. Kovalcinova, "Scaling of force networks for compressed particulate systems," *Contributing Talk at APS March Meeting*, San Antonio, Texas, March 2015

L. Kovalcinova, "Characterizing dense granular systems by percolation and statistical properties of force networks," *Contributing Talk at PASI on Particulate Media*, La Plata, Argentina, August 2014.

L. Kovalcinova, "Characterizing dense granular systems by percolation and statistical properties of force networks," *Contributing Talk at APS March Meeting*, Denver, Colorado, March 2015.

Dedicated to
Martin, Diana, Stanislav, Stanislav & Bernarda
Lucia, Zuzana, Pavol & Mária

" I want everybody to be smart. As smart as they *can* be. A world of ignorant people is too dangerous to live in."

-Garson Kanin
Born Yesterday

ACKNOWLEDGMENT

I would like to express a great gratitude to my advisor, Dr. Lou Kondic, for the academic guidance, support and patience during the whole time of my doctoral study.

I am very thankful to Dr. Guillaume Bal, Dr. Konstantin Mischaikow, Dr. Denis Blackmore, and Dr. Richard Moore for the review of my dissertation thesis and for agreeing to be on my thesis committee. I would like to extend additional gratitude specifically to Dr. Guillaume Bal and Dr. Konstantin Mischaikow for the fruitful discussions and guidance during our collaboration.

I am grateful to Dr. Arnaud Goullet for the help and many useful discussions, especially during my initial years at New Jersey Institute of Technology.

I would also like to thank the Department of Mathematical Sciences for creating a good working environment and for the effort that was put to maintain the administrative and financial support for all doctoral students.

Finally, I want to thank my closest family for the emotional and moral support during the time spent at New Jersey Institute of Technology.

This work was funded in part by the NSF Grants No. DMS-1521717 and DMS-0835611.

TABLE OF CONTENTS

TABLE OF CONTENTS
(Continued)

Chapter **Page**

TABLE OF CONTENTS
(Continued)

Chapter **Page**

LIST OF TABLES

Table **Page**

LIST OF FIGURES

LIST OF FIGURES
(Continued)

Figure **Page**

LIST OF FIGURES
(Continued)

Figure **Page**

CHAPTER 1

INTRODUCTION

1.1 Brief History and Applications

In 1930s, Ralph Alger Bagnold was amazed by sand dunes during his explorations of Libyan desert. This fascination resulted in a scientific study of sand dunes in a book "The Physics of Blown Sand and Sand Dunes", [5]. Not long after that, the scientific interest in granular material started to grow and nowadays research in this field belongs to one of the most active and growing research areas.

The reason for such a rapid growth of interest is very simple. Granular material has a vast variety of application areas, ranging from agriculture, pharmaceutical and construction industries, to geophysics and energy production. Inappropriate storing of granules can cause catastrophic events in construction, and spontaneous separation of big and small particles during the mixing can lead to a poor product quality in pharmaceutical industry or agriculture. And yet, almost every product we buy or food we eat, began in granular form.

Granular materials are very complex and thus difficult to describe. Particulate systems can behave like fluids when average particle velocity is high enough, or can take a solid-like form when strong inter-particle forces inside the medium cause particular systems to have a static form that can resist any small stress or pressure increments. If a granular system is very sparse and particles collide very rarely, we say that the system is a granular gas. Granular gases are very common in space - well known example are the rings of Saturn.

However, any of the three forms, fluid-like, solid-like or gas-like particulate systems show very different behavior from fluids, solids and regular gases. Since particles in granular systems are macroscopic, thermal fluctuations may often be

neglected. Particularly for the dense systems, the relevant energy is potential - due to compression of the particles. In addition, the interaction between the particles is inelastic, meaning that the energy is not conserved. Furthermore, inter-particle and particle-boundary friction is often present and it influences the particle-particle and particle-boundary interaction.

1.2 From Energy Propagation to Dense Granular Packings

In this work, we focus on studying dense granular systems and their properties. We start by considering the properties of granular systems in one dimension (1D) and analyze the influence of the disorder. Then, we proceed to more complex systems that can be either disordered, or be partially ordered. In 2D, interesting questions start to emerge, such as the influence of packing fraction on the connectivity of the set of particles inside a particle system (which is rather a trivial problem in 1D), or the mechanical stability. In addition, since the number of particles in 2D systems tends to be large and continuum models are often unreliable, energy propagation and loss is usually measured and characterized using statistical tools.

The natural extension of the 2D systems are the granular assemblies in 3D, where the questions mentioned above are even more relevant to real systems that occur in nature. However, the computational complexity is much larger and therefore we resolve to the careful comparison of the results with those in 2D.

1.3 Overview

In Chapter 2 we focus on the energy propagation through a chain of particles in 1D. We first give a brief overview of the previous work focused on a chain of particles with the same physical properties. Then, we introduce randomness into the particle masses. We discuss the dependence of the final solution for the propagation of the

initial pulse on the magnitude of randomness and the spatial scale on which the randomness varies.

The remaining part of this thesis focuses on 2D and 3D granular assemblies. In Chapter 3, based on our published work [36], we introduce the concept of percolation and jamming and study granular material consisting of purely repulsive particles and compare the results with systems where the particles can be attracted by capillary forces. The attractive capillary force is introduced only between particles that come into contact; such model of the particle-particle interaction is used to describe wet granular materials [29].

In Chapter 4, based on our published work [37], we continue studying dense 2D packings with the focus on the force networks composed of the interparticle forces. The analysis of the networks, and particularly of the number of connected clusters after imposing force thresholds, shows that there is a master curve that characterizes the granular systems with the same set of parameters. However, we show that the scaling is not universal, contrary to the conclusions of previous works on this topic.

Chapter 5 is focused on the phase transition in granular materials that is caused by pure shear. We compare directly the numerical and experimental results by showing the pressure and anisotropy evolution during the shear and find a good match when we add noise to the numerical results. The match between the simulations and experiments is further confirmed by the topological measures counting the number of connected components and loops within the force networks.

In Chapter 6, we analyze the source of energy dissipation in granular materials that can be either dry or wet. For the purpose of this analysis, we compare the numerical and experimental results for the periodically sheared granular system set up so that the particle displacement field is homogeneous during the shear.

Numerical simulations are further extended into 3D in Chapter 7. We compare the results for two force models for strongly compressed granular systems and analyze the pressure evolution during biaxial shear.

In Chapter 8 we conclude the thesis with a summary, conclusions and suggestions for future work.

CHAPTER 2

WAVE PROPAGATION IN STOCHASTIC GRANULAR CHAINS WITH RANDOM MASSES

2.1 Energy Propagation Through Stochastic Particulate Systems in One and Two Spatial Dimensions

2.1.1 Motivation

In this chapter, we discuss the dynamical behavior of 1D granular chain. We first start by reviewing previous works and introduce the analytical techniques used to model the behavior of the energy propagation mathematically.

We point out that there have been several studies describing the 1D chains of particles which have the same physical and geometrical properties. Such chains are described in detail in Nesterenko's book [50]. However, in the context of granular matter there have not been many studies exploring wave propagation in the systems where particles differ by their size, mass and other properties.

In Section 2.1.2 of this chapter, we review previous works that serve as a motivation for the proposed study of randomized particulate systems. The analysis in [50] is reviewed in detail, and we also discuss briefly other studies in this field. In Sections 2.2 - 2.5, we present our analysis of the energy propagation in stochastic 1D systems of particles. Section 2.6 is devoted to the simulations in which we probe the validity of the energy bounds on the wave propagation. This work is carried out in collaboration with Prof. Guillaume Bal.

2.1.2 Background

The granular materials appearing in nature are very complex. In order to describe their behavior, the researchers usually resort to formulating simplified models. For

example, for the purpose of understanding wave propagation in granular systems, one often considers 1D or 2D systems made out of circular particles of the same size.

Let us consider the simplest case, that is, a 1D chain of N aligned circular elastic particles of equal sizes and physical parameters and let us assume that the particles are initially pre-compressed by applying a constant force, F_0, at both ends of the chain. Compression can be modeled by assuming that the particles 'overlap' with the size of the overlap, δ_0, depending on F_0. An initial perturbation is introduced by applying an instantaneous force, F_{inst}, at time $t = 0$ on the left most particle.

Figure 2.1 shows an initially compressed chain perturbed from the left endpoint in the direction of F_{inst} causing the center of the i-th particle, x_i, to translate by a distance u_i. The initial perturbation propagates through the chain of particles and as we show below, the displacement on the i-the particle, u_i, can be described by the wave equation.

In the following analysis, we need to distinguish between two different types of particle overlap in terms of the overlap magnitude relative to the particle size. If the overlap $\delta_0 \ll |u_i - u_{i-1}|$ for each i, we say that the chain is weakly compressed. If, however, $\delta_0 \gtrsim |u_i - u_{i-1}|$, we say that the chain is strongly compressed.

To find the equation of motion of the particles in the chain, we first make an assumption that the particles interact via Hertz law, which yields the force between the particles, as a function of the particle overlap, to be

$$F = \frac{2E}{3(1-\nu^2)}\left(\frac{R_1 R_2}{R_1 + R_2}\right)^{\frac{1}{2}}\Big\{(R_1 + R_2) - (x_2 - x_1)\Big\}^{\frac{3}{2}} \tag{2.1}$$

where E is a Young's modulus, R_1 and R_2 are the radii of the two interacting particles, ν is a Poisson coefficient and x_1, x_2 are the coordinates of the particles. We assume that $x_2 > x_1$.

The model of a contact force based on the Hertzian particle-particle interaction is usually used to model real physical systems such as powders and strongly non-linear

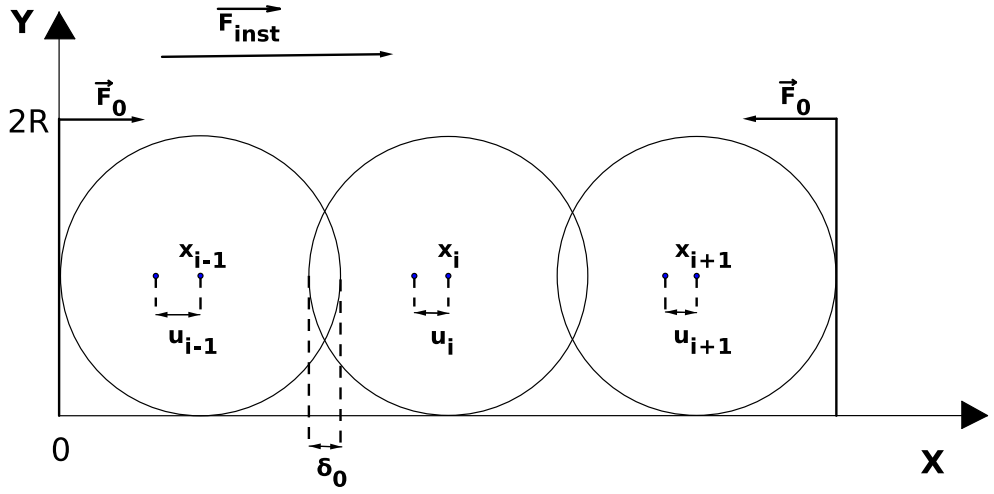

Figure 2.1 1D system of $N = 3$ particles with an initial overlap, δ_0, as a result of constant force, F_0. Initial perturbation propagates from left to right by applying F_{inst} at time $t = 0$. Direction of F_{inst} is indicated in the figure.

systems that cannot be characterized by linear approximation [51]. The constraints for validity of such a compression force model are discussed further in [50]. Here, we give a brief summary:

1. the maximum shear stresses achieved in the vicinity of contact must be less than the elastic limit.

2. the sizes of the contact surface are much smaller than the radii of curvature of each particle.

3. the characteristic time of the problem, τ, is much longer than the oscillation period during which the particle shape varies.

As alluded above, it is important to distinguish between different magnitudes of the initial compression of the particles. Therefore, in the following sections, we consider the limiting solution of the following cases:

1. Long-wave propagation of the initial perturbation for strong initial compression of a chain.

2. Long-wave propagation of the initial perturbation for a weakly compressed chain.

2.1.3 Long-wave Propagation of Initial Perturbation for a Strongly Compressed Chain

In this section, we describe in detail the propagation of the initial pulse (the force applied from the left end of the chain) through the long chain of strongly compressed aligned particles. The assumption that the particles are strongly compressed means that $|u_i - u_{i-1}| \ll \delta_0$. In addition, assuming that the chain is long allows us to make estimates with the errors approaching zero as the number of particles increases.

In the case of strong pre-compression, we need to account for the initial displacement, δ_0, in the equation of motion, that is comparable or even larger than the typical displacement from the impulse. The equation of motion is obtained by using Hertz'a and Newton's laws

$$\begin{aligned} u_{i,tt} &= A(\delta_0 - u_i + u_{i-1})^{3/2} - A(\delta_0 - u_{i+1} + u_i)^{3/2}, \quad N \geq i \geq 2 \qquad (2.2) \\ m &= \frac{4}{3}\pi R^3 \rho_0, \quad A = \frac{E(2R)^{\frac{1}{2}}}{3(1-\nu^2)m} \end{aligned}$$

Since it is assumed that $|u_{i\pm1} - u_i|/\delta_0 \ll 1$, the next step is to take out the common multiplier, δ_0, and expand the first two terms on the right hand side of Equation 2.2 in power series

$$(1+x)^n = 1 + nx + \frac{n(n-1)}{2!}x^2 + ..., \ |x| < 1 \qquad (2.3)$$

with $n = 3/2$ and $x = |u_{i\pm1} - u_i|/\delta_0$.

From the power series expansion, we obtain the following for the displacement of the i-th particle

$$u_{tt,i} = \alpha(u_{i+1} - 2u_i + u_{i-1}) + \beta(u_{i+1} - 2u_i + u_{i-1})(u_{i+1} - u_{i-1}),\ N - 1 > i \geq 2$$

with

$$\alpha = \frac{3}{2}A\delta_0^{1/2}, \qquad \beta = \frac{3}{8}A\delta_0^{-1/2}$$

In a long-wave limit, it is assumed that $\mathcal{L} \gg 2R$ with $\mathcal{L}$ a characteristic spatial size of a wave perturbation. Since we consider the long-wave approximation, differences become differentials and we can put $u_i = u(x_i)$ and analyze further the equation with $u(x)$ a continuous function. We obtain the non-linear wave equation

$$\begin{aligned} u_{tt} &= c_0^2 u_{xx} + 2c_0\gamma u_{xxxx} - \sigma u_x u_{xx}, \\ c_0^2 &= 6A\delta_0^{1/2}R^2, \quad \gamma = \frac{c_0 R^2}{6}, \quad \sigma = \frac{c_0^2 R}{\delta_0} \end{aligned} \tag{2.4}$$

An exact solution of Equation 2.4 can be obtained by first reformulating it into the KdV equation

$$\xi_t + c_0\xi_x + \gamma\xi_{xxx} + \frac{\sigma}{2c_0}\xi\xi_x = 0, \qquad \xi = -u_x$$

which according to [47] has a soliton solution and we arrive at

$$\begin{aligned} \xi - \xi_0 &= \Delta\xi = \Delta\xi_m sech^2\left\{\left(\frac{\sigma\Delta\xi_m}{24c_0\gamma}\right)^{\frac{1}{2}}(x - Vt)\right\} \\ V &= c_0 + \frac{\sigma}{6c_0}\Delta\xi_m, \quad \ell = \left(\frac{24c_0\gamma}{\sigma\Delta\xi_m}\right)^{\frac{1}{2}} \end{aligned} \tag{2.5}$$

where V is the soliton phase velocity and ℓ is the characteristic width.

2.1.4 Equation for a Weakly Compressed Chain

Here, we analyze the case when $|u_i - u_{i-1}| \gtrsim \delta_0$ and approximate the displacement of the i-th particle $u_i \approx u_i + \delta_0$; the approximation just changes the initial values for computing u_i and u_{i+1} by a small value (δ_0). The Equation 2.1 then becomes

$$u_{i,tt} = A(u_{i-1} - u_i)^{3/2} - A(u_i - u_{i+1})^{3/2} \tag{2.6}$$

Since $|u_i - u_{i\pm1}|/\delta_0 \gtrsim 1$, we cannot use the same expansion as in the case of the strong pre-compression. If we denote L to be a length of the particle chain, we have $L \gg 2R$, and the small parameter that can be used for the expansion and further approximations is $\epsilon = 2R/L$.

Similarly as for the strongly compressed chain, we expand $|u_{i\pm1} - u_i|$ in terms of ϵ. We again assume that $u_i = u(x)$ in the limit of $L \to \infty$ where $u(x)$ is a continuous function of space and compare the terms of the same order. After some algebra and by neglecting higher order terms, we obtain the following (see [49])

$$\begin{aligned} \xi_{tt} &= \left\{ c^2 \xi^{\frac{3}{2}} + \beta \xi_{tt} - b \xi^{-\frac{1}{2}} \xi_x^2 \right\}_{xx} \\ \beta &= \frac{a^2}{12}, \qquad b = \frac{a^2 c^2}{32} \\ \xi &= -u_x \end{aligned}$$

where $a = 2R$ and $c^2 = Aa^{5/2}$. The last expression leads to the solution in the case of weakly compressed chain.

In our analysis presented in the next section, we propose the model of the particle interactions for the granular chain with the random masses and arrive at the solution for the equation of motion. Similarly to the approach used, in this section we use the perturbation theory and expansion of the equation in a small parameter to explore the non-linear behavior of a particle chain.

2.1.5 Further Studies

The analytical work [50] reviewed in the previous section serves as a basis for our further mathematical and computational analysis. We begin with a brief overview of the studies of granular systems and several interesting concepts that were introduced in order to obtain a better understanding of the behavior of granular chains. Although not all of these ideas are used in our research, we find that it is important to mention them for completeness. We, however, put an emphasis on the studies of disordered granular material in our review.

Perhaps among the first attempts to extend the Nesterenko's work [50], are studies that analyze the dynamics in the set of aligned granular chains where the particles have additional interactions with the neighboring particles from the adjacent chains; the initial impulse of perturbation now propagates in both directions along the x and y axis.

The work in [64] presents the problems related to applications, and introduces interesting questions and analysis of the propagation of the initial impact in granular chains with buried impurities. Another study focuses on the impact of voids on the speed of propagation of initial perturbation [67] and numerical simulations in [44, 64] show the presence of a soliton-like behavior and backscattering in granular chains and when light impurities are present. Further numerical studies which include friction [59] and dissipation [14] in the model of particle interaction confirm that also in these cases the backscattering of the initial perturbation is present.

However, the aforementioned studies focus mainly on the identical particles. In the following, we overview the numerical and analytical studies that are closer to the reality - stochastic (disordered) systems. The wave propagation presented in [45] focuses on disordered and dissipative chains with power law repulsive potential particle-particle interaction. The initial perturbation propagates from the chain of identical particles to a polydisperse chain of particles with random masses, and the

velocity of the wave and maximum energy decays exponentially with the distance traveled. Further experimental observations in [19] show the additional formation of the secondary solitary waves in composite granular materials.

One of the most recent studies of wave propagation in random granular chains is carried out in [46] where the model of particle-particle interaction is Hertzian. The randomness is introduced either in the distribution of the masses, Young's modulus or particle size. The transfer between kinetic and potential energy is investigated and the results are compared between the cases with different randomized parameters. According to [46], there is an exponential and power law decay regime of the amplitude of the perturbation. The type of the decay regime was found to depend on the amplitude of the randomness.

In the light of the different models and experimental / numerical setups, we point to the useful detailed review [63] of previous analytical, experimental and numerical findings. The review focuses on the difference between the solitary waves in the continuum and discrete media such as granular matter. The conclusion of this review is that the main difference is in the formation of secondary solitary waves in the discrete case.

We conclude this overview of the existing results by pointing out that although a significant amount of research on 1D particle chains and 2D disordered systems has been carried out, there is no good understanding of the influence of randomness on the wave propagation and it is not clear whether continuum models can be formulated in such a case. We proceed to discuss the introduction of randomness in the following section.

2.2 Discrete Wave Equation

In this section, we analyze stochastic granular chain. Since randomness is very common in the nature, we always observe granular materials with particles that

do not tend to be of the same geometrical and physical properties. Therefore, as a natural extension, we study granular chain involving random parameters and propose appropriate models. Specifically, we introduce the randomness by assuming that particle have random masses.

In what follows, we derive the equation of motion in the chain of particles interacting by linear (Hookian) interaction. The choice of a Hookian interaction between particles is motivated by simplicity in comparison with Hertzian interaction and furthermore by a possible extension to $2D$, where Hooke's law is known to be a good approximation of a non-plastic particle interaction.

Let us consider a 1D chain of particles with random masses and the propagation of the initial impulse from left to right. Before we continue with the analysis, we introduce the following notation.

Notation:

- N number of particles
- L length of the chain of particles
- x_i position of i-th particle
- $\frac{L}{N} = h$ distance between two particles
- $u(x_i)$ displacement of the i-th particle from the equilibrium position. We suppose that $u(x_i)$ is also time dependent, but omit the explicit notation for a simplicity.
- $m(1 + \epsilon\mu_i)$ mass of the i-th particle

We assume that the randomness is introduced by a random variable μ_i and ϵ is a small parameter.

There are two forces that act on the i-th particle. Below, we denote the force between the particles i and $i+1$ by F_{i+1} and F_{i-1} is the force between particles i and $i-1$. From the Hooke's law

$$\begin{aligned} F_{i+1} &= k(u(x_{i+1}) - u(x_i)) \\ F_{i-1} &= k(u(x_{i-1}) - u(x_i)) \\ F_{tot} &= F_{i+1} + F_{i-1} \end{aligned}$$

where F_{tot} is the total force acting on the i-th particle. By applying the Newton's second law we obtain the equation continuous in time and discrete in space

$$\begin{aligned} u(x_i)_{tt} m(1+\epsilon\mu_i) &= k\{u(x_{i+1}) - u(x_i)\} + k\{u(x_{i-1}) - u(x_i)\} \\ &= k\{u(x_{i+1}) - 2u(x_i) + u(x_{i-1})\} \end{aligned} \tag{2.7}$$

We assume the zero boundary conditions so that we have

$$u(x_0) = u(x_N) = 0 \tag{2.8}$$

Next, we rescale mass, time, length and k:

$$\begin{aligned} m &= m'M \\ t &= t'T \\ x &= x'L \\ \Rightarrow k &= k'\frac{M}{T^2} \\ h &= h'L \Rightarrow h' = \frac{1}{N} \end{aligned}$$

and so we obtain

$$\partial_{t't'} u(x_i')(1+\epsilon\mu_i) = \frac{k'}{m'N^2} \frac{u(x_{i+1}') - 2u(x_i') + u(x_{i-1}')}{h'^2}$$

To have a simpler and shorter notation, we denote:

$$\begin{aligned} u(x_i) &= u_i \\ u(x_i + h) &= u_{i+1} \\ u(x_i - h) &= u_{i-1} \end{aligned}$$

Dropping the "prime", and choosing k' such that $k'/m'N^2 = 1$ we have

$$\begin{aligned} \partial_{tt} u_i (1 + \epsilon \mu_i) &= \frac{u_{i+1} - 2u_i + u_{i-1}}{h^2} \\ u_0 &= u_N = 0 \end{aligned} \tag{2.9}$$

2.3 Energy Estimates

Before we continue with the analysis of the Equation 2.9, there are several questions we need to answer. What is the influence of the "discreteness" on the right hand side of the Equation 2.9? What are the conditions, under which we could expect that the limit $h \to 0$ is justified? It is quite simple to see that we will obtain the wave equation if we can go to the limit $h \to 0$. However, we need to analyze what happens if we cannot pass to the limit $h \to 0$, especially when the randomness of the masses is large enough to influence the wave propagation in the particle chain. Another question is what is a magnitude of randomness, ϵ, for which we cannot assume that $h \to 0$ for the approximation of the equation of motion by wave equation.

The approach we use to answer these questions consists of these steps:

1. We expand the Equation 2.9 in ϵ and compare the terms of the same order.

2. We bound the total energy of each term of the expansion and validate our expansion in ϵ.

3. We compare h and ϵ terms and set the condition for the existence of continuum limit $h \to 0$.

Following the sketched approach, we first assume that $\epsilon \ll 1$ so that we can expand u_i in terms of ϵ

$$u_i = u_i^0 + \epsilon u_i^1 + \epsilon^2 u_i^2 + \dots \tag{2.10}$$

and substitute u_i into Equation 2.9

$$\begin{aligned}(1+\epsilon\mu_i)\partial_{tt}\{u_i^0 + \epsilon u_i^1 + \epsilon^2 u_i^2 + \dots\} &= \frac{1}{h^2}\{u_{i-1}^0 + \epsilon u_{i-1}^1 + \epsilon^2 u_{i-1}^2 \dots\} \\ &- \frac{2}{h^2}\{u_i^0 + \epsilon u_i^1 + \epsilon^2 u_i^2 + \dots\} \\ &+ \frac{1}{h^2}\{u_{i+1}^0 + \epsilon u_{i+1}^1 + \epsilon^2 u_{i+1}^2 + \dots\}\end{aligned}$$

After comparing the terms of the same order in ϵ we introduce a new system of equations with continuous second derivative in time and finite differences in space and consider only the terms up to $O(\epsilon)$ to obtain the two following equations with zero boundary conditions

$$\begin{aligned}\partial_{tt} u_i^0 &= \Delta_h u_i^0 \\ u_0^0 &= u_N^0 = 0\end{aligned} \tag{2.11}$$

$$\begin{aligned}\partial_{tt} u_i^1 + \mu_i \partial_{tt} u_i^0 &= \Delta_h u_i^1 \\ u_0^1 &= u_N^1 = 0\end{aligned} \tag{2.12}$$

where the discrete operator $\Delta_h u_i^k$ is defined as follows

$$\Delta_h u_i^k = \frac{u_{i+1}^k - 2u_i^k + u_{i-1}^k}{h^2}$$

Next, we find the energy bounds on all of the terms $u^k, k = 0, 1, \dots$ in the expansion specified by Equation 2.10. After bounding u^0 and u^1, we analyze the terms of higher order in ϵ at once by setting $v = u - u^0 - \epsilon u^1$ and bounding v. After

that we proceed to solve only Equation 2.11 and Equation 2.12 and find the necessary relationship between ϵ and h to pass the limit $h \to 0$.

The first step is to prove that the energy in the system is conserved. To show this, we write down the "discrete" version of the potential energy. We denote by E the total energy of the particle chain

$$Eu = \frac{h}{2}\sum_{i=1}^{N}(1+\epsilon\mu_i)(\partial_t u_i)^2 + (\nabla_h u_i)^2 \tag{2.13}$$

where the discrete operator ∇_h has the form

$$\nabla_h u_i = \frac{u_{i-1} - u_i}{h}$$

Using the classical approach to prove constant energy for the continuous case we show that the time derivative of the energy vanishes. The time derivative is given by

$$\begin{aligned} \partial_t Eu &= \frac{h}{2}\sum_{i=1}^{N}(1+\epsilon\mu_i)\partial_t(\partial_t u_i)^2 + \partial_t(\nabla_h u_i)^2 \qquad (2.14)\\ &= \frac{h}{2}\sum_{i=1}^{N} 2(1+\epsilon\mu_i)(\partial_{tt}u_i)(\partial_t u_i) + 2(\partial_t\nabla_h u_i)\nabla_h u_i \end{aligned}$$

The second term in the sum can be treated by summation by parts

$$\begin{aligned} h\sum_{i=1}^{N}(\partial_t\nabla_h u_i)\nabla_h u_i &= (\partial_t u_N)\nabla_h u_N - (\partial_t u_1)\nabla_h u_1 - h\sum_{i=1}^{N}(\partial_t u_i)\nabla_h\nabla_h u_i \qquad (2.15)\\ &= -h\sum_{i=1}^{N}(\partial_t u_i)\Delta_h u_i \end{aligned}$$

The first two terms on the right hand side in the Equation 2.15 are automatically zero in the case of zero boundary conditions. We substitute the identity from Equation 2.15 into Equation 2.14

$$\begin{aligned} \partial_t Eu &= \frac{h}{2}\sum_{i=1}^{N} 2(1+\epsilon\mu)(\partial_{tt}u_i)(\partial_t u_i) - 2(\partial_t u_i)\Delta_h u_i\\ &= \frac{h}{2}\sum_{i=1}^{N} 2(\partial_t u_i)\{(1+\epsilon\mu)(\partial_{tt}u_i) - \Delta_h u_i\} \end{aligned}$$

By using Equation 2.9, the last expression vanishes and therefore we can infer that the energy is conserved.

For the zero-th order term in the Equation 2.11 we have by the computations analogous to the above

$$\begin{aligned} Eu^0 &= \frac{h}{2}\sum_{i=1}^{N}(\partial_t u_i^0)^2 + (\nabla_h u_i^0)^2 \\ \Rightarrow \partial_t Eu^0 &= 0 \end{aligned}$$

For the energy of u^1 we have

$$\begin{aligned} Eu^1 &= \frac{h}{2}\sum_{i=1}^{N}(\partial_t u_i^1)^2 + (\nabla_h u_i^1)^2 \\ \partial_t Eu^1 &= \frac{h}{2}\sum_{i=1}^{N}\partial_t(\partial_t u_i^1)^2 + \partial_t(\nabla_h u_i^1)^2 \\ &= \frac{h}{2}\sum_{i=1}^{N}2(\partial_t u_i^1)(\partial_{tt} u_i^1) - 2(\partial_t u_i^1)\Delta_h u_i^1 \end{aligned}$$

and by using the Equation 2.12 in the last expression we obtain

$$\begin{aligned} \partial_t Eu^1 &= -\frac{h}{2}\sum_{i=1}^{N}2(\partial_t u_i^1)\mu_i(\partial_{tt} u_i^0) \\ &\leq \sqrt{2}\sqrt{Eu^1}||\partial_{tt}u^0||.||\mu||_\infty \end{aligned} \tag{2.16}$$

In the last expression, we used the Cauchy-Schwartz inequality

$$\begin{aligned} \sqrt{\sum_{i=1}^{N}(\partial_t u_i^1)^2} &\leq \sqrt{\sum_{i=1}^{N}(\partial_t u_i^1)^2 + (\nabla u_i^1)^2} \\ &= \sqrt{\frac{2}{h}E\partial_t u^1} \end{aligned} \tag{2.17}$$

and the following identity

$$\sqrt{\sum_{i=1}^{N}(\partial_{tt} u_i^0)^2} = \sqrt{\frac{1}{h}}||\partial_{tt}u^0||$$

We can rewrite the time derivative of the energy of the first order term, u^1, in to following way

$$\begin{aligned} \partial_t E u^1 &= \partial_t (\sqrt{E u^1})^2 \\ &= 2\sqrt{E u^1}\partial_t \sqrt{E u^1} \end{aligned} \tag{2.18}$$

and substitute this expression into Equation 2.16 to obtain the energy bound on u^1

$$\begin{aligned} \partial_t E u^1 &\leq \sqrt{2}\sqrt{E u^1}||\partial_{tt} u^0||.||\mu||_\infty \\ \Rightarrow \partial_t \sqrt{E u^1} &\leq \sqrt{\frac{1}{2}}||\partial_{tt} u^0||.||\mu||_\infty \\ \sqrt{E u^1} &\leq \sqrt{\frac{1}{2}}\int_0^t ||\partial_{\tau\tau} u^0||.||\mu||_\infty d\tau \end{aligned} \tag{2.19}$$

Following the same approach we can make an estimate for $\partial_t u^1$. Taking the time derivative of Equation 2.12 for u^1 and carrying out the same calculations, we have

$$\sqrt{E\partial_t u^1} \leq \sqrt{\frac{1}{2}}\int_0^t ||\partial_{\tau\tau\tau} u^0||.||\mu||_\infty d\tau \tag{2.20}$$

This estimate will be very useful later, when we will have to estimate the bound for the terms of order of ϵ^2.

Let us now consider the contribution of the higher orders, denoted by v_i. We have

$$v_i = u_i - u_i^0 - \epsilon u_i^1$$

We assume that the higher order terms in v_i will be bounded and will not influence the equation of motion and thus can be neglected. We need to find the restrictions on ϵ such that the higher order terms contained in v_i can be neglected. To do this,

we ask for which values of ϵ, $v_i < C$ for some constant C. From the Equation 2.9

$$\begin{aligned} \partial_{tt}[(1+\epsilon\mu_i)(v_i+u_i^0+\epsilon u_i^1)] &= \Delta_h(v_i+u_i^0+\epsilon u_i^1) \\ \Rightarrow (1+\epsilon\mu_i)\partial_{tt}v_i+\epsilon^2(\partial_{tt}u_i^1)\mu_i &= \Delta_h v_i \end{aligned}$$

Recall that we denote the discrete space derivative $\nabla_h u_i^k = (u_{i-1}^k - u_i^k)/h$. To estimate the energy of v, we use the same approach as before for the energy bounds of u^1 and u_t^1

$$\begin{aligned} \partial_t Ev &= \partial_t\left[\frac{h}{2}\sum_{i=1}^{N}(1+\epsilon\mu_i)(\partial_t v_i)^2+(\nabla_h v_i)^2\right] \\ &= -\frac{h}{2}\sum_{i=1}^{N}2\epsilon^2\mu_i(\partial_t v_i)\partial_{tt}u_i^1 \\ &\leq 2\epsilon^2\sqrt{E\partial_t u^1}\sqrt{Ev}||\mu||_\infty \\ &\leq 2\epsilon^2\sqrt{Ev}||\mu||_\infty\sqrt{\frac{1}{2}}\int_0^t||\partial_{\tau\tau\tau}u^0||.||\mu||_\infty d\tau \end{aligned}$$

In the last inequality we used the inequality from Equation 2.20. Next, we approximate the upper bound for $\sqrt{Ev}$

$$\begin{aligned} \sqrt{Ev} &\leq \epsilon^2||\mu||_\infty^2\sqrt{\frac{1}{2}}\int_0^t\int_0^T||\partial_{\tau\tau\tau}u^0||d\tau dT \\ &\leq \epsilon^2||\mu||_\infty^2\int_0^t\int_0^T\sqrt{E\partial_{\tau\tau}u^0}d\tau dT \end{aligned}$$

In the last expression we have dependence only on the u_i^0 terms. Moreover, we already know that the energy of u^0 is constant, so taking the initial conditions of u^0 to be

$$u_i^0(0) = k(i)$$

$$\partial_t u_i^0(0) = j(i)$$

we have that

$$Eu^0 = \sum_{i=1}^{N} (j(i))^2 + (\nabla_h k(i))^2$$

and furthermore

$$\begin{aligned} \partial_t j(i) &= \nabla_h^2 k(i) \\ \partial_{tt} j(i) &= \partial_t \nabla_h^2 k(i) = \nabla_h^2 j(i) \\ \partial_{tt} \nabla_h k(i) &= \nabla_h^3 k(i) \end{aligned}$$

by substituting for the u^0 term

$$\begin{aligned} \sqrt{E \partial_{tt} u^0} &= \sqrt{\frac{h}{2} \sum_{i=1}^{N} (\nabla_h^2 j(i))^2 + (\nabla_h^3 k(i))^2} \\ &\leq \sqrt{\frac{1}{2}} (||\nabla_h^2 j|| + ||\nabla_h^3 k||) \end{aligned}$$

For the final estimate of the energy bound on v we have

$$\sqrt{Ev} \leq \epsilon^2 ||\mu||_\infty^2 \sqrt{\frac{1}{2}} \int_0^t \int_0^T ||\nabla_h^2 j|| + ||\nabla_h^3 k|| d\tau dT \tag{2.21}$$

Our goal now is to set conditions on ϵ and h such that we can neglect the terms of higher order in ϵ. In other words we want $O(Ev) < O(\epsilon)$. After bounding the energy of v we can analyze a simpler set of differential equations, Equation 2.11 and Equation 2.12.

From a careful examination of Equation 2.21, we see that we have these orders of h in Equation 2.21

$$\nabla_h^2 j = O\left(\frac{1}{h^2}\right), \qquad \nabla_h^3 k = O\left(\frac{1}{h^3}\right)$$

This is of course the worst case scenario, when the second and third derivatives of the initial conditions are not continuous. If we put a condition on smoothness of j

and k, we obtain different orders of h for $\nabla_h^2 j$ and $\nabla_h^3 k$. Thus to make our estimate more general, we now assume that

$$\nabla_h^2 j = O(h^m), \qquad \nabla_h^3 k = O(h^l)$$

where $m \geq -2$ and $l \geq -3$. Without a loss of generality we can suppose that $m \geq l$. For the estimate of the order of Ev we have

$$\sqrt{Ev} \;\; = \;\; O(\epsilon^2 h^l)$$

As mentioned earlier, we want the order of Ev to be smaller than ϵ. Therefore, our condition on ϵ and h is

$$\begin{aligned} \epsilon^2 h^l &\ll \epsilon \\ \Rightarrow \epsilon &\ll h^{-l} \end{aligned}$$

If we have smooth initial conditions, $l = 0$, our estimate is trivially $O(\sqrt{Ev}) = O(\epsilon^2) \ll 1$. Later, when we analyze the influence of randomness on the wave propagation, we obtain another constraint on ϵ and h.

2.4 Solution by Continuous Estimate

After finding the energy bounds on all terms from Equation 2.10, we can now focus on solving only Equations 2.11 and 2.12 while we assume that $\epsilon \ll h^{-l}$. Equation 2.11 is deterministic and in the limit of $h \to 0$ we obtain the wave equation. More interesting case is the second equation that contains the random term μ_i.

We begin the analysis by first replacing u_i by a continuous function. For a sufficiently smooth function $U(x,t)$ and μ, we have

$$u_i = U(x,t)|_{x=ih} \tag{2.22}$$

$$\mu_i = \mu(x)|_{x=ih} \tag{2.23}$$

By a sufficiently smooth function $U(x,t)$ we mean that $U(x,t)$ is assumed to be C^4 in space and C^2 in time. These assumptions will help us to estimate the error that we make by replacing the original function u_i by its continuous estimate, $U(x,t)$. The equation of motion for the continuous estimate $U(x,t)$ is

$$\begin{aligned}(1+\epsilon\mu(x))\partial_{tt}U(x,t) &= \nabla_h U(x,t) \\ &= \partial_{xx}U(x,t)+O(h^2)\end{aligned}$$

which implies that we have the wave equation when $h \to 0$ with zero boundary conditions

$$\begin{aligned}(1+\epsilon\mu(x))\partial_{tt}U(x,t) &= \partial_{xx}U(x,t) \\ U(0,t) &= U(Nh,t)=0\end{aligned} \tag{2.24}$$

2.4.1 Error from the Continuous Estimate

Let us denote the discrete derivative of the continuous function $U(x,t)$ by

$$\Delta U(x,t) = \frac{U(x+h,t)-2U(x,t)+U(x-h,t)}{h^2} \tag{2.25}$$

To find the error from the continuous estimate we need to compute the error we make in each term u_k of Equation 2.9 when replacing u_i at $x=ih$ by $U(x,t)$. In the following computations we omit variable t in the notation of $U(x,t)$ and write $U(x)$ instead. It should be kept in mind, however, that $U(x)$ depends on time as well. We denote the error from continuous estimate $Err(x)$ at $x=ih$. To find the error, we subtract the corresponding terms of the continuous Equation 2.24 from the discrete Equation 2.9

$$\begin{aligned}Err(x) &= |(1+\epsilon\mu_i)\partial_{tt}u_i-(1+\epsilon\mu)\partial_{tt}U(x)|+|\Delta u_i-\partial_{xx}U(x)| \\ &= (1+\epsilon\mu)|\partial_{tt}U(x)-\partial_{tt}U(x)|+|\Delta U(x)-\partial_{xx}U(x)| \\ &= |(\partial_{xx}-\Delta)U(x)|\end{aligned} \tag{2.26}$$

To estimate the error in terms of $(\partial_{xx} - \Delta)U(x)$ we use the Taylor expansion of $U(x)$ in h centered at point $x = ih$

$$\begin{aligned} U(x+h) &= U(x) + \sum_{k=1}^{3} \frac{1}{k!}\partial_x^k U(x)h^k + \frac{4h^4}{4!}\int_0^1 (1-\tau)^3 \partial_x^4 U(x+th)d\tau \\ U(x-h) &= U(x) + \sum_{k=1}^{3} \frac{1}{k!}\partial_x^k U(x)(-h)^k + \frac{4h^4}{4!}\int_0^1 (1-\tau)^3 \partial_x^4 U(x-th)d\tau \end{aligned}$$

and plugging back into Equation 2.26 we have

$$\begin{aligned} (\partial_{xx} - \Delta)U &= \partial_{xx}U - \frac{2\partial_{xx}Uh^2 + \frac{h^4}{3!}\int_0^1 (1-\tau)^3 \partial_x^4 \{U(x+th) + U(x-th)\}d\tau}{h^2} \\ &= -\frac{h^2}{3!}\int_0^1 (1-\tau)^3 \partial_x^4 \{U(x+th) + U(x-th)\}d\tau \end{aligned}$$

The above yields that

$$Err(x) \sim O(h^2) \tag{2.27}$$

We can observe that the error estimate, Equation 2.27, does not depend on ϵ, since the random term vanishes in Equation 2.26.

2.4.2 Influence of Randomness on the Continuous Solution

We introduce continuous estimate for terms u^0 and u^1

$$u_i^0 = U^0(x,t)|_{x=ih} \tag{2.28}$$

$$u_i^1 = U^1(x,t)|_{x=ih} \tag{2.29}$$

The equations for U^0 and U^1 up to the order h^2 are the continuous versions of Equations 2.11 and 2.12

$$\begin{aligned} \partial_{tt}U^0 &= \partial_{xx}U^0 \\ U^0(0,t) &= U^0(Nh,t) = 0 \end{aligned} \tag{2.30}$$

and

$$\begin{aligned} \partial_{tt}U^1 + \mu\partial_{tt}U^0 &= \partial_{xx}U^1 \\ U^1(0,t) &= U^1(Nh,t) = 0 \end{aligned} \tag{2.31}$$

We proceed to analyze the influence of randomness on the term U^1, since the term U^0 is not influenced by μ. The well-known solution to the non-homogeneous wave equation suggests the solution to the Equation 2.31

$$U^1(x,t) = -\frac{1}{2}\int_{x-t}^{x+t}\int_0^t \partial_{tt}U^0(y,t-s)\mu(y)dyds \tag{2.32}$$

If $\partial_{tt}U^0 \equiv 1$, then

$$U^1 = -\frac{1}{2}\int_{x-t}^{x+t}(t-|x-y|)\mu(y)dy \qquad |x-y| < t \tag{2.33}$$

Now let us suppose that masses of particles vary on a spatial scale given by η. We have

$$\mu = \mu\left(\frac{x}{\eta}\right)$$

Since μ is a random variable, U^1 is also a random variable and we can find its variance and thus expected value

$$E(U^1(x,t))^2 = \frac{1}{4}\int_{-\infty}^{\infty}\int_{x-t}^{x+t}(t-|x-y|)(t-|x-z|)\mathrm{M}\left(\frac{y-z}{2\eta}\right)dydz \tag{2.34}$$

where M is the correlation function corresponding to the random variable μ. After substitution $f = (y+z)/2$, $g = (y-z)/2$

$$\begin{aligned} E(U^1(x,t))^2 &= \frac{1}{4}\int_{-\infty}^{\infty}\int_{-\infty}^{\infty}(t-|x-f-g|)(t-|x-f+g|)\mathrm{M}\left(\frac{g}{\eta}\right)2dfdg \\ &= \frac{1}{2}\int_{-\infty}^{\infty}\int_{-\infty}^{\infty}\eta(t-|x-f-g'\eta|)(t-|x-f+g'\eta|)\mathrm{M}(g')dfdg' \\ &\sim O(\eta) \end{aligned}$$

(In the last equation, we put $g' = g/\eta$). The variance is of order η and if we assume that μ has a Gaussian distribution, we see, that

$$U^1 \sim \sqrt{\eta} N(0,1) \tag{2.35}$$

where $N(0,1)$ denotes the standard normal distribution.

The interesting comparison now comes from the error that arises from the approximation of u by a continuous function U. We have seen that the error we make by this estimate is $O(h^2)$ and including the error from neglecting the terms of the order of ϵ^2, we have the error of order $O(h^2+\epsilon^2)$. Also, we know that $U^1 \sim \sqrt{\eta} N(0,1)$. Thus

$$u \sim U^0 + \epsilon\sqrt{\eta} N(0,1) + O(h^2 + \epsilon^2) \tag{2.36}$$

To see the influence of randomness, the error from the continuous estimate must be smaller than the order of U^1. The following must hold

$$h^2 + \epsilon^2 \ll \epsilon\sqrt{\eta} \tag{2.37}$$

which yields

$$\begin{aligned} h^2 &\ll \epsilon\sqrt{\eta} \\ \epsilon^2 &\ll \epsilon\sqrt{\eta} \\ \frac{h^2}{\sqrt{\eta}} \ll \quad \epsilon \quad &\ll \sqrt{\eta} \end{aligned} \tag{2.38}$$

The last result gives us constraints on the parameters ϵ, η and h. In the case when $h \sim \eta$ we can observe that each particle in the granular chain has different mass. Therefore, if the randomness in masses of particles is on the scale of h we have the following

$$h^{3/2} \ll \epsilon \ll \sqrt{h} \tag{2.39}$$

In other words, the Equation 2.39 tells us that for ϵ in the range between $h^{3/2}$ and $\sqrt{h}$ the energy propagation in the chain can be described by the Equation 2.36 for the case when the randomness varies on the particle scale.

2.5 Solution to the Discrete Equation

To solve the discrete Equation 2.12 for u_1 we proceed to find the Green's function

$$\begin{aligned}(\partial_{tt} - \Delta_h)G(x,\xi,t,t') &= \delta(x-\xi)\delta(t-t') \\ &= \delta(ih-jh)\delta(t-t')\end{aligned}$$

For convenience, we will denote the Green's function $G(x,\xi,t,t')$ as $G(x)$. We use the Fourier transform

$$\begin{aligned}&\int_{-\infty}^{\infty} \partial_{tt}G(x)e^{-2\pi ix\xi} - \frac{1}{h^2}\int_{-\infty}^{\infty}(G(x-h)e^{-2\pi ix\xi}dx \\ &+2\frac{1}{h^2}\int_{-\infty}^{\infty} G(x)e^{-2\pi ix\xi}dx - \frac{1}{h^2}\int_{-\infty}^{\infty} G(x+h)e^{-2\pi ix\xi}dx \\ &= \int_{-\infty}^{\infty}\delta(ih-jh)\delta(t-t')e^{-2\pi ix\xi}dx\end{aligned}$$

and

$$\delta(t-t') = \partial_{tt}\hat{G} - \frac{1}{h^2}(e^{2\pi ih\xi} + e^{-2\pi ih\xi} - 2)\hat{G} \tag{2.40}$$

Since $(e^{\pi ih\xi} - e^{-\pi ih\xi})/2 = i\sin(\pi h\xi)$, we have

$$\partial_{tt}\hat{G} + \frac{1}{h^2}4\sin^2(\pi h\xi)\hat{G} = \delta(t-t') \tag{2.41}$$

The last equation can be solved using the classical approach where we first find the homogeneous solution for the following equation and then find the particular solution

to the Equation 2.41

$$\partial_{tt} y + \frac{1}{h^2} 4 \sin^2(\pi h \xi) y = 0$$
$$y = 0$$
$$\partial_t y = 0$$

Homogeneous solution takes the form

$$y_1 = \left[\sin \frac{2(\sin \pi h \xi)}{h} \right] t \quad \text{and} \quad y_2 = \left[\sin \frac{2(\cos \pi h \xi)}{h} \right] t \tag{2.42}$$

Let us denote $k = 2(\sin \pi h \xi)/h$. To find the Green's function, we need to impose the zero initial conditions and the superposition of these two independent solutions

$$\begin{aligned} u_1 &= A \sin kt + B \cos kt \\ u_2 &= C \sin kt + D \cos kt \\ u_1(0) &= 0 \\ u_2'(0) &= 0 \end{aligned}$$

From the above, we find $B = 0$ and we can put $A = 1$, since A is a free variable. Similarly, we have $C = 0$ and without a loss of generality we can put $D = 1$. The Wronskian of u_1 and u_2 is

$$\begin{aligned} w &= u_1 u_2' - u_1' u_2 \\ &= -k(\sin kt)^2 - k(\cos kt)^2 \\ &= -k \end{aligned}$$

For the Fourier transform of the Green's function

$$\hat{G}(t, t') = \begin{cases} -\frac{\sin kt \cos kt'}{k} & 0 \le t < t' < \infty \\ -\frac{\sin kt' \cos kt}{k} & 0 \le t' < t < \infty \end{cases} \tag{2.43}$$

We find the inverse Fourier transform and immediately obtain Green's function for the original problem

$$G(x,\xi,t,t') = \begin{cases} -\int_{-\infty}^{\infty} e^{2\pi i x\xi'} \frac{\sin\frac{2\sin\pi h\xi'}{h} t \cos\frac{2\sin\pi h\xi'}{h} t'}{\frac{2\sin\pi h\xi'}{h}} d\xi' & 0 \le t < t' < \infty \\ -\int_{-\infty}^{\infty} e^{2\pi i x\xi'} \frac{\sin\frac{2\sin\pi h\xi'}{h} t' \cos\frac{2\sin\pi h\xi'}{h} t}{\frac{2\sin\pi h\xi'}{h}} d\xi' & 0 \le t' < t < \infty \end{cases}$$

We will, however, continue the discussion by presenting the numerical simulations that consider different types of the randomness. We will focus on the magnitude of the random term, μ_i , and the randomness in the spacial scale.

2.6 Numerical Simulation of the Pulse Propagation in One Dimensional Chain with Random Masses

Granular 1D chain of particles with the power law potential interaction, random masses and diameters was previously investigated numerically in [45]. It was found that the maximum kinetic energy of the initial impulse decayed exponentially with the distance traveled. This observation was confirmed in [46] and it was found that the exponential decay depended on the magnitude of the randomness. Here, we investigate the propagation of an initial impulse through a granular chain with random masses where the particles interact via the linear (Hookian) spring as described in Section 2.2. Due to a different type of the particle interaction, our results do not exhibit the same behavior as those in [45, 46] and we find an approximate solution to the wave propagation of the impulse.

To confirm the analytical solution and its range of validity derived in the previous section, we perform numerical simulations and find the influence of the magnitude (parameter ϵ) and spatial scale (parameter η) of the randomness of masses on the propagation of an impulse through a granular chain. The numerical scheme used in simulations is 4th order accurate. We solve the Newton's equations of motion for each particle, where the number of particles is set to $N_p = 1000$. The particles are assumed to be perfectly elastic so that here is no dissipation.

To investigate the influence of the randomness of masses and its spatial distribution, we vary η. Given the value of η we assume that every ηN_p consecutive particles have the same mass chosen from the random distribution $\epsilon N(0,1)$. It is implicitly assumed that $\eta N_p \geq 1$.

To prevent the particle separation, we start form the initial condition where the particle chain is weakly pre-compressed. Every particle has a small overlap with its neighboring particles that is equal to the $10^{-7}d$, where $d = 1/N_p$ is the rescaled particle diameter. The scales used in our model are the chain length, L, average particle mass, m, and the binary collision time, τ_c (described in detail in Appendix A).

The impulse is propagating in the chain from the left and is introduced at time $T = 0$ as an overlap of the 10 left most particles with their neighbors; the initial overlap of the first and second particle is equal to $0.06d$ and for the remaining particles the magnitude of overlap decays exponentially up to the value $10^{-7}d$. During the simulations, we fix the endpoints of the chain. No energy losses are introduced and the total energy is conserved.

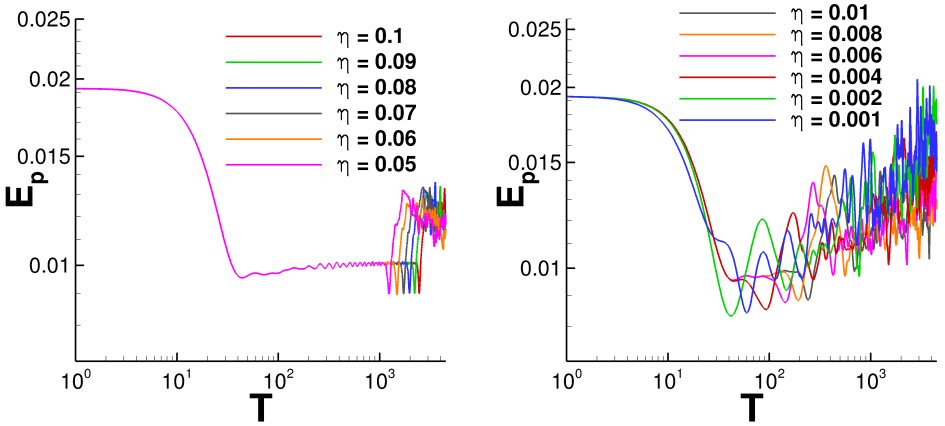

(a) (b)

Figure 2.2 Potential energy of the particle chain as a function of time, T; the value of E_p is displayed for (a) $\eta \in [0.05, 0.1]$ and (b) $\eta \in [0.001, 0.01]$ for $\epsilon = 0.1$, $N_p = 1000$.

Figure 2.2 shows the evolution of the potential energy, denoted by E_p, in time, T, for different values of the parameter η. We fix the value of $\epsilon = 0.1$; the choice of ϵ was motivated by the effort to display different regime for different values of η. According to Equation 2.36, the influence of the randomness of the masses is proportional to $\epsilon\sqrt{\eta}$.

The initial decrease of E_p in Figure 2.2 corresponds to the change of the potential energy to the kinetic energy, E_k. After the change of E_p to E_k, we observe different regimes for different values of η. When $\eta \in [0.05, 0.1]$, the wave travels through the chain with the small perturbations in E_p that correspond to the exchange of the kinetic and potential energy on the particle scale up to a time $T \approx 2 \times 10^3$. The first dip in E_p at $T \approx 2 \times 10^3$ corresponds to the backscattering wave that forms due to the first change in the particle masses. For the randomness of the masses on the smaller spatial scale, $\eta \in [0.001, 0.01]$, the potential energy, E_p, exhibits a random behavior immediately after the exchange of the E_p and E_k at $T \approx 50$. When $\eta \in [0.01, 0.05]$ (not shown), the evolution of E_p resembles the behavior for the case $\eta \in [0.05, 0.1]$ with larger fluctuations after the first dip occurs.

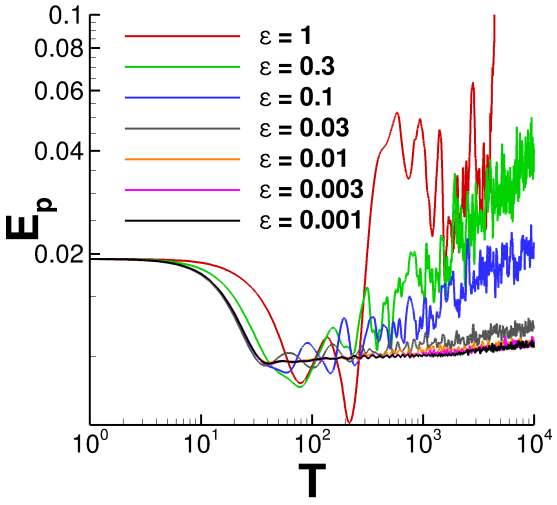

Figure 2.3 Potential energy of the particle chain as a function of the time, T, for different values of ϵ with $\eta = 0.001$ and $N_p = 1000$.

From Inequality 2.38 we have that when $\epsilon = 0.1$ the value of η has to be $\eta \gg 0.1$ and $\epsilon \gg 10^{-6}/\sqrt{\eta}$ to observe wave propagation described by Equation 2.36. In fact, our results in Figure 2.2 show that the regime where $\eta \in [0.001, 0.01]$ is different from the regime when $\eta \in [0.05, 0.1]$, consistently with the bounds on ϵ and η that guarantee the wave propagation with additional stochastic term (Equation 2.36). Careful parameter analysis and quantification of the influence of noise on wave propagation is still needed and should be a part of the future work.

Figure 2.3 shows the evolution of E_p for the fixed value of $\eta = 0.001$ which for $N_p = 1000$ particles means that every particle has a different mass. According to Equation 2.36, the particle displacement, u, has an additional noise (stochastic) term of the order of $\epsilon\sqrt{\eta}N(0,1)$ when $h^2/\sqrt{\eta} \ll \epsilon \ll \sqrt{\eta}$ and the continuous estimate of u becomes $u \sim U_0 + \epsilon\sqrt{\eta}N(0,1)$. Therefore we expect the fluctuations of E_p to be of order $\epsilon\sqrt{\eta}$ as well. The results in Figure 2.3 show a strong dependence of the noise in E_p on the value of ϵ (the value of η is fixed) consistently with our estimate. These preliminary observations will be further analyzed and quantified as a part of future work.

2.7 Conclusions

In this chapter, we analyze how a perturbation propagates through a stochastic chain of particles. A randomness of various noise amplitude and characterized by different spatial scale is introduced in particle masses. We find the energy bounds on the higher order terms in the expansion of the equation of motion. We present the approximate solution of the stochastic wave equation and the energy bounds are used to find the constraints on the solution validity.

The validity of the wave approximation is investigated in simulations. The potential energy of the chain shows the dependence on the randomness and we find

the agreement with the constrains on ϵ and η . The detailed analysis of the influence of ϵ and η will be a part of the future work.

CHAPTER 3

PERCOLATION AND JAMMING PROPERTIES OF TWO DIMENSIONAL GRANULAR SYSTEMS

3.1 Introduction

In Chapter 2 we consider one dimensional chain of particles and find, that added randomness has a large influence on the impulse propagation in the chain. Moreover, we find that the decay of the impulse magnitude strongly depends on the randomness on the spatial scale (varying the η parameter). In this chapter, that is based on our published work [36], we continue to analyze particle systems with randomness involved in the particle masses, while keeping the density of the material constant (so that the particle sizes differ). The granular systems considered here are two dimensional and we start from the stress free state where there is no contact between the particles.

In particular, we focus on percolation and jamming transitions for particulate systems exposed to compression. For the systems built of particles interacting by purely repulsive forces in addition to friction and viscous damping, it is found that these transitions are influenced by a number of effects, and in particular by the compression rate. In a quasi-static limit, we find that for the considered type of interaction between the particles, percolation and jamming transitions coincide. For cohesive systems, however, or for any system exposed to even slow dynamics, the differences between the considered transitions are found and quantified.

The dense systems of particles interacting by either purely repulsive potentials, such as dry granular particles, or by both repulsive and attractive ones, such as wet granulates, appear virtually everywhere, from nature to a variety of applications bridging the scales from nano to macro. The structure of the force field by which the particles interact may be very complex, in particular on meso-scales where this force

field is nonuniform and forms force networks. These networks are of relevance not only to granular systems, but to many other ones, such as foams and colloids. Their properties have been recently explored using a variety of different approaches, ranging from theoretical and computational ones based on exploring local structure of force networks [55], networks type of approaches [6, 30], and topological methods [3, 35, 38].

While percolation has been considered for dense particulate systems [1, 4, 40, 65], much more is known about static and ordered lattice-based systems [58, 69], for which two types of percolation are discussed – rigidity and connectivity percolation [2, 27]. However, lattice models do not account for nonlinear effects at particle contacts, such as friction and viscous damping, or for dynamics, so it is unclear whether the results obtained for lattice systems apply to particulate ones [27]. For the latter, the connection between percolation (connectivity) and jamming (rigidity) transitions was discussed recently for both non-cohesive and cohesive frictionless systems, and it was found (for the systems considered) that these two transitions in general differ [40, 65]. However, these conclusions were reached by considering rather specific interaction models (over-damped dynamics), and the question whether they hold in general, and whether they also follow from the models commonly used to simulate physical granular particles, is still open.

In this chapter, we discuss the relation between percolation and jamming for frictional and frictionless particles in two spatial dimensions, both with and without cohesion. We consider slowly compressed systems that go through percolation and jamming and discuss how these transitions depend on the system properties. The motivation for considering compression is that it is a simple protocol that avoids the complexities associated with shear, and allow us to focus the discussion. However, consideration of any dynamics, including compression, naturally leads to the questions related to the rate-dependence of the results, and, as we will see, to new insight into percolation and jamming transitions for evolving particulate systems.

The chapter is organized as follows. In Section 3.2 we present the simulation techniques. In Section 3.3 we define reference system and present our findings: first for purely repulsive systems in Section 3.3.1, and then for cohesive ones in Section 3.3.2. Section 3.4 is devoted to summary, conclusions, and future outlook of the current work.

3.2 Numerical Simulations

We perform discrete element simulations using a set of circular particles confined in a square domain. Initially, the system particles are placed on a square lattice and are given random velocities; we have verified that the results are independent of the distribution and magnitude of these initial velocities. The discussion related to possible development of spatial order as the system is compressed can be found in [38], and the issue of spatial isotropy of the considered systems is considered later in the text.

In our simulations gravity is not considered, and the diameters of the particles are chosen from a flat distribution of width r_p. System particles are soft inelastic disks and interact via normal and tangential forces, including static friction, μ (as in [35, 38]). The particle-particle (and particle-wall) interactions include normal and tangential components. The force model used to simulate the interaction between particles that are in collision is described in detail in Appendix A. Cohesive forces that form when particles collide and are present up to a specific separating distance when cohesive bridge breaks, are modeled as outlined in Appendix B.

To carry out the simulations, we use the following isotropic compression protocol. First, we slowly compress the domain, starting at the packing fraction 0.63 and ending at 0.90, by the moving walls built of monodisperse particles with diameters of size d_{ave} placed initially at equal distances, d_{ave}, from each other. The wall particles move at a uniform (small) inward velocity, v_c, equal to $v_0 = 2.5 \cdot 10^{-5}$

(in the units of d_{ave}/τ_c; time scale τ_c is a binary collision time, described in detail in Appendix A), or a fraction of it, as we explore the influence of compression speed. Due to compression and uniform inward velocity, the wall particles (that do not interact with each other) overlap by a small amount. When the effect of compression rate is explored, v_c is decreased, or the compression stopped to allow the system to relax. In order to obtain statistically relevant results, we simulate a large number of initial configurations (typically 20), and average the results. Due to the compression being slow, we do not observe any different behavior close to the domain boundaries compared to the rest of the domain.

We integrate Newton's equations of motion for both the translational and rotational degrees of freedom using a 4th order predictor-corrector method with time step $\Delta t = 0.02$ (Appendix A). Our reference system is defined by $N_p = 2000$ polydisperse particles ($r_p = 0.2$), with $k_n = 4 \cdot 10^3$, $e_n = 0.5$, $\mu = 0.5$, and $k_t = 0.8k_n$ [25]; the (monodisperse) wall particles have the same physical properties. Larger domain simulations are carried out with up to $N_p = 20,000$ particles. If not specified otherwise, cohesion is not included.

3.3 Results

3.3.1 Purely Repulsive Systems

Figure 3.1(a) shows an example of the reference system at $\rho = 0.90$, with the particles color-coded according to the total normal force, normalized by the average normal force, $\langle \mathrm{F^n} \rangle$ (we focus only on the normal forces in this chapter). If the system contains a set of particles in contact that connects top/bottom or left/right wall, then there is contact percolation. We will also consider force percolation by focusing on the particles sustaining force larger than a given force threshold and ask how the percolation properties are influenced by a non-vanishing threshold.

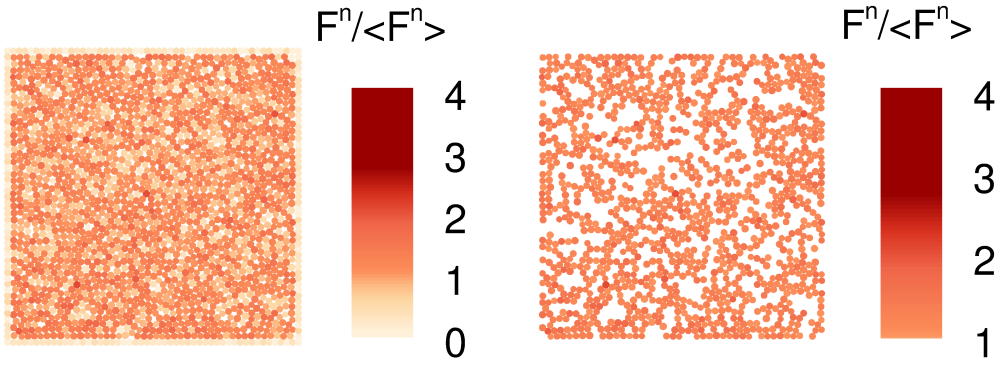

(a) (b)

Figure 3.1 An example of a reference system for different force thresholds at $\rho = 0.9$: (a) $\bar{F} = 0$ and (b) $\bar{F} = 1$.

As an example, Figure 3.1(b) shows the same system as in Figure 3.1(a) with force threshold $\bar{F} = 1$. While the system shown in Figure 3.1(a) clearly percolates (contact percolation), it is not immediately obvious whether the system shown in Figure 3.1(b) does.

In describing percolation properties, we use the following quantities, all based on averaging over multiple realizations: $P(\rho, \bar{F})$, the percolation probability; $\bar{F}_p$, the percolation force threshold, defined by $P(\rho, \bar{F}_p) = 0.5$; and $P_c(\rho)$, the contact percolation probability, defined as $P_c(\rho) = P(\rho, 0)$. In addition, we will use Z, the coordination number, measuring average number of contacts per particle; a sharp increase of the Z curve is typically associated with the jamming transition, see, e.g. [43]. We note that the listed quantities also depend on the number of particles, N_p, and on the compression speed, v_c; this dependence will be discussed later in the chapter. For the simplicity of notation, we do not include this dependence explicitly in the notation.

Figure 3.2(a) shows $P(\rho, \bar{F})$, for the reference system. We see that, starting at $\rho \approx 0.77$, there is a percolation transition; note that if we vary $\bar{F}$ and keep ρ fixed, this transition is rather sharp for large ρ's and more spread out for $\rho \in [0.77, 0.81]$.

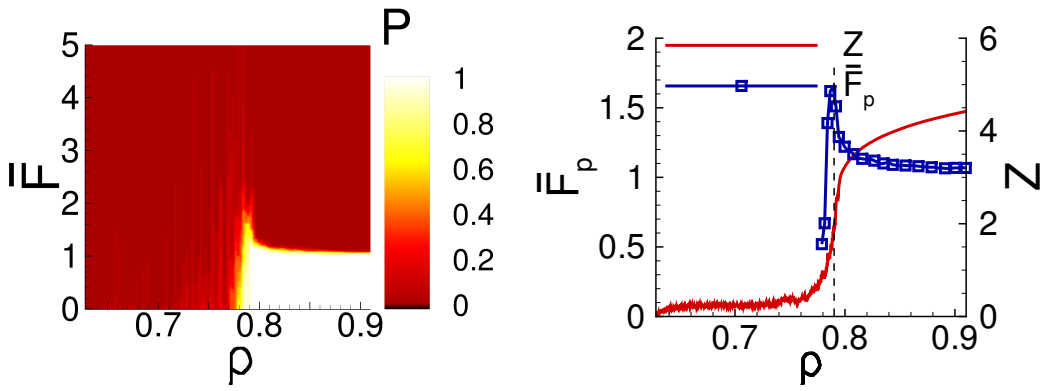

(a) (b)

Figure 3.2 Reference system, averaged over 20 realizations: (a) the percolation probability, $P(\rho, \bar{F})$ and (b) $\bar{F}_p$ vs. Z.

To describe various transitions that take place as the system is compressed, we define: ρ_J, at which jamming, defined here as the ρ at which the Z curve has an inflection point, takes place (later in the text we also show that at ρ_J rapid increase in pressure (measured at the domain boundaries) occurs, supporting this definition of ρ_J); and ρ_p, at which contact percolation, defined as $P_c(\rho_p) = 0.5$ occurs. Figure 3.2(b) shows Z and $\bar{F}_p$; we find from the data shown that $\rho_J \approx 0.79$ (the vertical dashed line in the figure). Note that just below ρ_J, there is a strong force network that percolates, as shown by large $\bar{F}_p$. The dominant maximum of $\bar{F}_p$ calls for consideration of another transitional ρ at which this maximum occurs: however, we find that this transition is always sandwiched between ρ_p and ρ_J, so we will not discuss it in more details here.

Figure 3.3(a) shows Z and P_c for the reference system. While there is some noise in the results, one can still obtain an accurate value for $\rho_p \approx 0.776$. [For this, and all other results involving ρ_p and ρ_J, uncertainty of the results is such that the results are accurate up to three significant digits: for ρ_J we use standard error to estimate uncertainty, and for ρ_p we estimate the range over which $0.4 \leq P_c(\rho) \leq 0.6$.] Therefore, the results for our reference system suggest that $\rho_p < \rho_J$, and the question is whether this finding is robust with respect to the changes of the system parameters

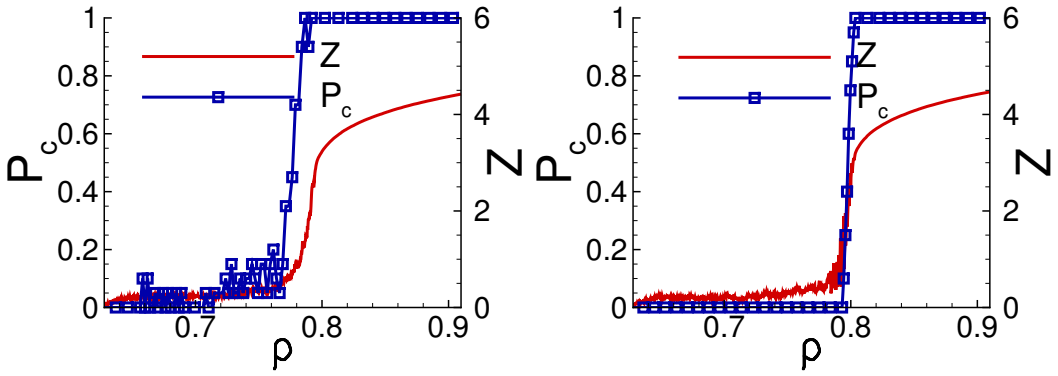

Figure 3.3 Reference system: the percolation probability, P_c, and Z.

and of the protocol used. Before proceeding, we note that although there are some differences between realizations, for all of them we find consistently (for the considered system) that ρ_p and ρ_J differ by a non-vanishing amount.

Regarding the system parameters, we start by discussing the influence of polydispersity, measured by r_p, and friction coefficient, μ. Table 3.1 shows the results for ρ_p and ρ_J, and we observe that both ρ_p and ρ_J are monotonously decreasing functions of these two parameters; in particular the results for ρ_J are consistent with the ones from literature (see [35] and the references therein). The finding that is perhaps more relevant for the present discussion is that the difference between ρ_p and ρ_J remains as r_p and μ are varied.

Next we discuss the influence of system size; note that this issue has been discussed extensively in the context of random percolation (see e.g. [69]). Here, the context is more complicated since the system considered is dynamic, and one has to decide on coupling of relevant spatial and temporal scales. We have considered two scenarios for the systems of different size: one where the rate of the change of ρ is kept constant, and the one where the compression speed (v_c) is fixed. While the details of the results vary depending on the choice of the scenario, we find that the difference between ρ_p and ρ_J remains non-zero (and typically increases as a function of L) for the both scenarios and for the system sizes defined by $L = 50,\ 75,\ 100,\ 150$:

Table 3.1 Influence of μ, r_p and v_c on ρ_p and ρ_J for the Continuously Compressed Systems (the parameters that are not specified correspond to the reference case).

μ						
	0.0	0.1	0.2	0.3	0.4	0.5
ρ_J	0.827	0.812	0.802	0.797	0.796	0.789
ρ_p	0.815	0.799	0.792	0.784	0.781	0.776

r_p					
	0.0	0.1	0.2	0.3	0.4
ρ_J	0.804	0.797	0.789	0.7834	0.782
ρ_p	0.786	0.784	0.776	0.771	0.766

v_c/v_0					
	0.0	0.02	0.05	0.1	1.0
ρ_J	0.798	0.799	0.798	0.792	0.789
ρ_p	0.798	0.794	0.791	0.786	0.776

Figure 3.4 shows the dependence of ρ_p and ρ_J behavior on the system size using two aforementioned protocols. Figure 3.4(a) shows results for the fixed compression rate; the compression velocity, v_c, is increased with L so that the rate v_c/L is constant. Figure 3.4(b) shows ρ_p, ρ_J when we keep v_c constant as L increases. For both protocols – fixed compression rate and speed – we observe increased difference between ρ_p and ρ_J as L is increased.

Since the reference system is exposed to a non-vanishing compression rate, there is also the question of rate-dependence, as already alluded above. To explore this issue, we carry out simulations with progressively smaller speed of compression, using $v_c = v_0/10, v_0/20$ and $v_0/50$. We find that the P_c transition becomes sharper as v_c decreases, indicating that ρ_p is affected by v_c; in general, for a fixed ρ, the particles

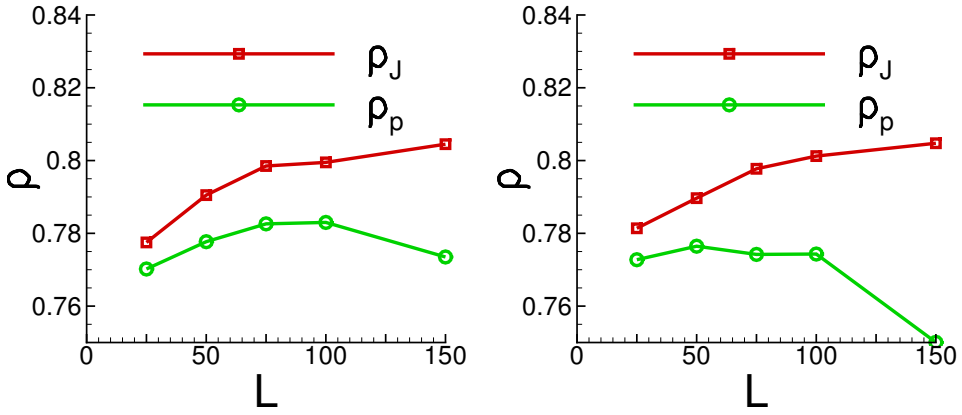

Figure 3.4 Influence of the system size on ρ_p and ρ_J for (a) fixed compression rate and (b) fixed compression speed.

are less likely to percolate for smaller v_c and therefore ρ_p increases as v_c decreases. Both ρ_p and ρ_J are shown in Table 3.1. While both ρ's increase as v_c decreases, the crucial finding is that the difference between them becomes smaller for slower compression. The question remains whether ρ_p and ρ_J collapse to a single value in the limit $v_c \to 0$. To answer this, we consider a modified protocol such that we interject relaxation steps in our compression (we reference this protocol by $v_c = 0$). More precisely, after compressing the system by $\delta\rho = 0.001$, we check whether there is a percolating cluster. If not, we proceed with compression; if yes, the system is relaxed until percolation disappears, and then the system is further compressed. We carry out this procedure until such ρ_p that percolating cluster does not disappear after relaxation (for all considered simulations, the system always percolates above ρ_p found using relaxation protocol, or in other words, percolation is never found to disappear as a system is further compressed). Figure 3.3(b) shows P_c and Z for the relaxed system, suggesting much smoother and sharper evolution of P_c through ρ_p. Table 3.1 shows that for the reference system and $v_c = 0$, ρ_p and ρ_J collapse to the same point, within the available accuracy. We have reached the same finding for the other systems listed in Table 3.1, including monodisperse frictionless system - while this particular

system is known to show different behavior due to partial crystallization [35], it still leads to $\rho_p = \rho_J$. We have also verified that the finding $\rho_p = \rho_J$ still holds when different system sizes are considered.

This finding of collapse of percolation and jamming transitions appears to be different from the one in [65], where it was found that ρ_p and ρ_J differ. The source of the difference seems to be the use of over-damped dynamics in [65]; this effect apparently keeps the particles together and leads to percolation even for small ρ's.

We find, however, that, within the particle interaction model considered, based on (constant) coefficient of restitution, e_n, the finding $\rho_p = \rho_J$ persists even for very small $e_n \approx 0$, suggesting that the finding reported here is robust, within the framework of the implemented particle interaction model.

While the findings obtained in quasi-static limit are of main interest, one should note that in the context of particulate matter, percolation and jamming transitions typically involve dynamics, even if very slow one. Close to ρ_J, the relevant time scales diverge in the limit of infinite system size, and therefore, one could expect that for any sufficiently large system, even very slow dynamics may lead to (arbitrarily small) differences between ρ_p and ρ_J. Therefore, it should not be surprising if differences are found between ρ_p and ρ_J for slowly evolving spatially extended particulate systems.

To close our discussion focusing on repulsive systems, we discuss whether the implemented compression protocol may induce an anisotropy, possibly influencing the results. For this purpose, we compute the stress tensor and the distribution of the angles of contacts between the particles. For brevity, we consider here only the compression by v_0. The stress anisotropy, τ_a, is defined by

$$\tau_a = \frac{\sigma_1 - \sigma_2}{\sigma_1 + \sigma_2} \tag{3.1}$$

with σ_1, σ_2 the principal eigenvalues of the Cauchy stress tensor σ, specified by

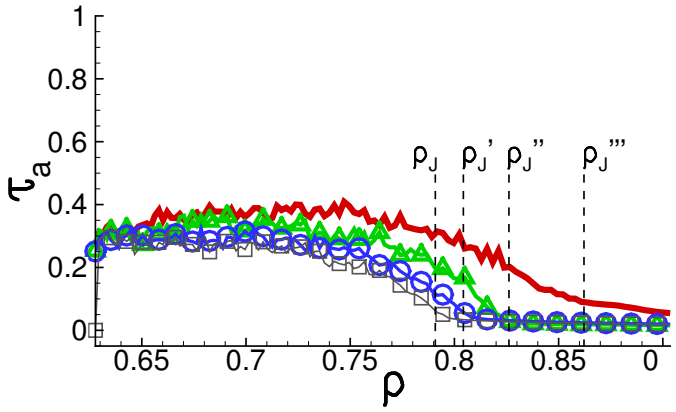

Figure 3.5 Anisotropy of the stress tensor of $r_p = 0.2, \mu = 0.5$ (squares), $r_p = 0.0, \mu = 0.5$ (circles), $r_p = 0.2, \mu = 0.0$ (triangles) and $r_p = 0.0, \mu = 0.0$ (thick line) systems as a function of packing fraction, ρ. Respective jamming transitions, $\rho_J, \rho_J', \rho_J'', \rho_J'''$, are depicted by a dashed line.

$$\sigma_{ij} = 1/(2A) \sum_{c_k,p} (F_i r_j + F_j r_i) \tag{3.2}$$

as a sum over all inter-particle contacts c_k for all particles p; (wall particles as well as the contacts of interior particles with the wall particles are not included here). Here, A is the total area of the system, r_i, r_j are the x and y components of the vector pointing from the center of particle p towards the particle contact c_k. F_i, F_j denote the x, y components of the inter-particle force at the contact c_k.

Figure 3.5 shows τ_a as a function of ρ. We depict jamming transitions, $\rho_J, \rho_J', \rho_J''$ and ρ_J''' by dashed lines for $\mu = 0.5, r_p = 0.2$ (reference system), $\mu = 0.5, r_p = 0.0$, $\mu = 0.0, r_p = 0.2$ and $\mu = 0.0, r_p = 0.0$, respectively.

While far below the jamming (and percolation) transitions, the anisotropy measured by τ_a may be present, close to ρ_p and ρ_J, $\tau_a \ll 1$ for all systems considered, showing that the systems are essentially isotropic for the packing fractions of relevance here. Above jamming points, τ_a is even smaller.

Figure 3.6 shows the distribution of contact angle, ϕ, for the reference system, the parts (a), (b), and for the $\mu = 0.0$, $r_p = 0.0$ system, the parts (c), (d).

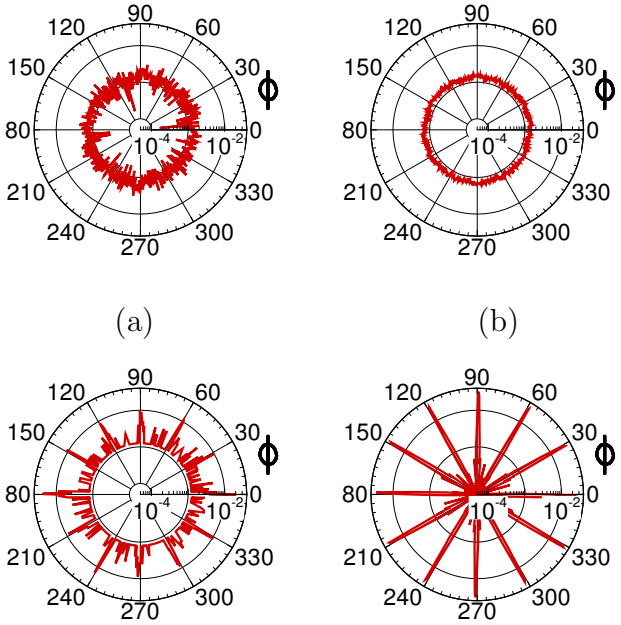

Figure 3.6 Distribution of the angles of contacts for the reference (a), (b) and $r_p = 0.0$, $\mu = 0.0$ system (c), (d). In these polar plots, the azimuthal coordinate, ϕ, corresponds to the angle between the line connecting the centers of contacting particles and the $+x$ axis, and the radial one to the probability of observing given ϕ.

Most importantly, this figure shows symmetric distribution of ϕ's. In addition, by comparing the results of the reference case with the ones obtained for monodisperse frictionless, we also observe the influence of partial crystallization on the latter, for large packing fractions.

3.3.2 Cohesive Systems

Here, we discuss the effect of cohesion on percolation and jamming. We have considered few different 'strengths' of cohesion (specified by the distance, s_c), at which capillary bridges break; for brevity here we present results only for 'weak' cohesion, specified by small distance at which capillary bridges break, $s_c \approx 0.0028 \ll 1$ (see Appendix B). We focus on the relaxed reference system. Figure 3.7(a) shows that the percolation transition occurs very close to (the starting value) $\rho = 0.63$. The

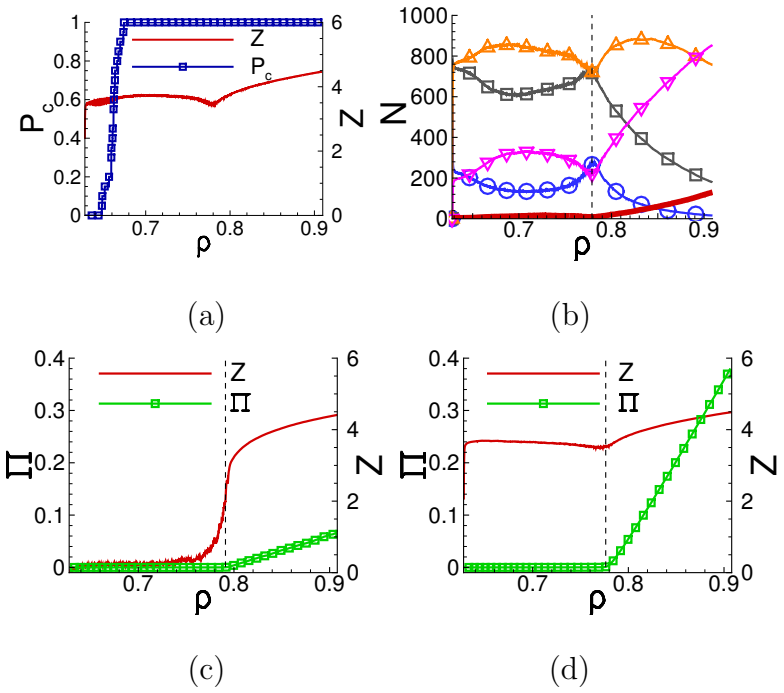

Figure 3.7 (a), (b) Cohesive relaxed system. (c), (d) Pressure on the walls, Π, and Z. Dashed lines correspond to ρ_J (and to ρ_p in (c)); in (a), ρ_p is shown by dotted line.

Z curve remains at high values for all considered ρ's, but we note that there is a kink in the Z curve at $\rho \approx 0.783$. The kink and consecutive increase of Z suggest that the system undergoes a transition. To verify that this transition corresponds to ρ_J, we consider the pressure on the system walls, Π. Figure 3.7(c and d) shows this pressure (force/length, in dimensionless units) for both the reference system, and for the cohesive one. We see that for the reference system an increase of Π occurs at ρ_J (inflection point of the Z curve). Figure 3.7(d) shows that an increase in Π and the kink in the Z curve occur at the same $\rho = \rho_J = 0.783$.

Clearly, the difference between ρ_J and ρ_p is significant for the considered cohesive system, consistently with the earlier work [40]. As expected, we find similar results for the systems characterized by larger s_c (results not shown for brevity). The strong influence of weak cohesion on the ρ_p and ρ_J suggests that for any

non-vanishing cohesion, one would find differences between ρ_P and ρ_J, with this differences disappearing only in the limit of $s_c \to 0$. As soon as there is no attractive force, the difference between ρ_p and ρ_J vanishes even in the limit of inelastic collisions, $e_n \to 0$.

One may ask about the origin of the 'kink' in the Z curves for the cohesive system. An intuitive explanation is as follows: as compression starts, the particles immediately get in contact, form mini-clusters (consisting of a small number of particles), leading to rather large Z; due to the presence of cohesive forces, relaxation does not lead to breakup of the existing contacts. Therefore, as long as ρ is small, the mini-clusters do not break; as ρ grows, however, collisions start separating particles, leading to breakup of the mini-clusters and decreasing Z. At some point, when ρ becomes sufficiently large so that all particles are effectively in contact, Z starts growing again, and at the same ρ, Π starts increasing. To support this description, Figure 3.7(b) shows the number of particles (N_p) with $2, \ldots, 6$ contacts (cn). We observe that as ρ_J is approached from below, the $cn = 4,\ 5$ curves have negative slope, suggesting breakup of the clusters (this breakup is presumably also partially responsible for the positive slope of $c_n = 2,\ 3$ curves for the same values of ρ); at ρ_J these trends reverse.

3.4 Summary and Conclusions

Percolation and jamming transitions of evolving particulate systems are non-trivial. We find that these transitions for repulsive particles interacting by a commonly used interaction model coincide for quasi-static systems; this finding, together with the results reported in [65], where these transitions are found to differ for particles following over-damped dynamics, suggests that the considered transitions may be influenced significantly by the type of interaction between the particles. Furthermore, our finding is that any, even very slow dynamics may lead to the differences of the

packing fractions at which percolation and jamming occur. Therefore, in particular close to jamming, a careful exploration will be needed in order to distinguish the effects due to dynamics and due to, e.g., the type of interaction between the particles. In the same vein, we are also finding that even minor cohesive effects have a strong influence in particular on percolation transition.

CHAPTER 4

SCALING OF THE FORCE NETWORKS IN TWO DIMENSIONAL GRANULAR MATERIALS

4.1 Introduction

Particulate materials are relevant in a variety of systems of practical relevance. It is well known that macroscopic properties of these systems are related to the force networks - the mesoscale structures that characterize the internal stress distribution. The force networks are built on top of the contact networks formed by the particles. These contact networks have been studied using a number of approaches, see [2, 58] for reviews. However, the properties of force networks, that form a subset of the contact networks based on the interaction force, are not slaved to the contact one: a single contact network can support infinite set of possible force networks, due to indeterminacy of the interaction forces. These force networks have been analyzed using a variety of approaches, including distributions of the force strengths between the particles [48, 56], the tools of statistical physics [41, 57, 66, 78], local properties of the force networks [55, 71, 72], networks-based type of analysis [6, 30, 77], as well as the topology-based measures [3, 4]. Of relevance to the present work are the recent results obtained using algebraic topology [35, 38, 39] that have shown that in particular frictional properties of the particles play an important role in determining connectivity properties of the considered force networks. For illustration, Figure 4.1 shows an example of the experimental system (discussed in more details later in the chapter), where the particles are visualized without (a) and with (b) cross-polarizers; in the part (b) force networks are clearly visible.

The recent work [52] suggests that properties of these force networks are universal. In other words, the finding is that, when properly scaled, the distributions

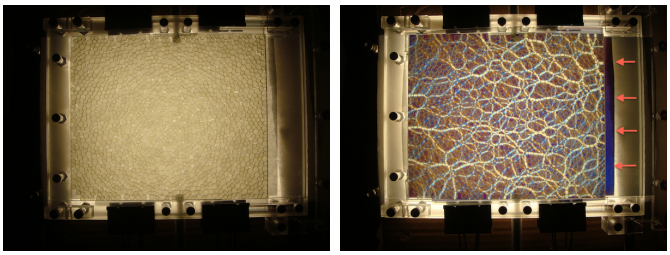

(a) (b)

Figure 4.1 Experimental images of two-dimensional system of photoelastic particles, obtained (a) without and (b) with cross-polarizer. The arrows indicates the side of the container where pressure is applied. The images are taken from [37]

of force clusters (defined as groups of particles in contact experiencing the force larger than a specified threshold) collapse to a single curve. In [52] it has been argued that this universality finding is independent of the particle properties like polydispersity and friction, or anisotropy of the force networks induced by shear [53]. The influence of anisotropy on the exponents describing scaling (and universality) properties of force networks was further considered using q-model [54], where it was found that anisotropy may have a strong influence on the scaling exponents.

In this chapter, that is based on our published work [37], we further explore the generality of the proposed universality in the setup where anisotropy is not relevant. We use discrete element simulations described in Chapter 3 with the details of the force model given in Appendix A. The exploration of the scaling validity is motivated in part by the following 'thought' experiment. Consider a model problem of perfectly ordered monodisperse particles that under compression form a crystal-like structure. In such a structure, each particle experiences the same total normal force, $\mathrm{F^n}/\langle \mathrm{F^n} \rangle = 1$ (normalized by the average force). If we choose any force threshold $\bar{F} \leq 1$, we obtain only one (percolating) cluster that includes all the particles. For any $\bar{F} > 1$, there are no particles. As an outcome, the mean cluster size, $\bar{S}(\bar{F})$ (including the percolating cluster), is a Heaviside function regardless of the system size, and $S(\bar{F})$, a mean cluster size without the percolating cluster, is zero everywhere. Considering

the scaling properties of the S-curve for different system sizes is therefore trivial and the scaling exponents (discussed in detail in the rest of the chapter) are not well defined. Furthermore, the fractal dimension, D_f, related to the scaling exponents [69], leads trivially to $D_f = D$, where D is the number of physical dimensions. Clearly, the scaling properties of such an ideal system are different compared to the ones expected for a general disordered system. Therefore, we found at least one system where 'universality' does not hold.

One could argue that such perfect system as discussed above is not relevant to physical setups, so let us consider a small perturbation - for example a system of particles of the same or similar sizes, possibly frictionless, that are known to partially crystallize under compression [35, 38]. For such systems, $\bar{S}(\bar{F})$ is not a Heaviside step function, but it may be close to it. Therefore, there is an open question whether these systems (that partially crystallize) still lead to 'universal' force networks. One significant result of this work is that this is not the case. Going further, we will also show that the systems of frictionless particles, even if they do not crystallize partially, still lead to non-universal force networks.

The remaining part of this chapter is organized as follows. In Section 4.2, we describe computations of scaling parameters in Section 4.2.1 and discuss the results for the scaling exponent, ϕ, and the fractal dimension, D_f, in Section 4.2.2; outline the influence of the structural properties of considered systems in Section 4.2.3; discuss the influence of compression rate and different jamming packing fractions in Section 4.2.4, and then present the results for the other scaling parameters, ν and f_c in Section 4.2.5. We conclude this section by presenting the results of physical experiments that were motivated by the computational results in Section 4.2.6. Section 4.3 is devoted to the conclusions.

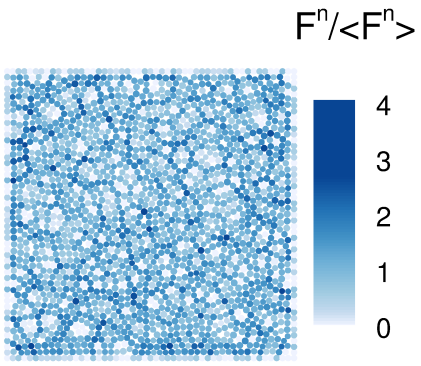

Figure 4.2 Reference system at $\rho = 0.9$.

4.2 Force Networks and Scaling Laws

In Chapter 3, we discussed the percolation and jamming transitions that take place as the system is exposed to compression. We identified the packing fractions at which these transitions occur as ρ_c (percolation) and ρ_J (jamming). For the present purposes, the most relevant finding is that for the repulsive systems, ρ_c and ρ_J are very close and, in the limit of quasi-static compression, the two transitions coincide and $\rho_c = \rho_J$.

In this chapter we focus on the systems such that $\rho > \rho_c$, and in particular on the properties of the force networks. Figure 4.2 shows an example of a compressed packing, with the particles color coded according to the total normal force, $\mathrm{F^n}$, normalized by the average normal force, $\langle \mathrm{F^n} \rangle$ (we will focus only on the normal forces in the present work). The properties of these networks depend on the force threshold, $\bar{F}$, such that only the particles with $\bar{F} \leq (\mathrm{F^n}/\langle \mathrm{F^n} \rangle)$ are included. We will now proceed to use the tools of percolation theory to study cluster size distribution and mean cluster size as $\bar{F}$ varies, considering force networks to be composed of the particles and inter-particle forces that can be thought of as nodes and bonds, consecutively.

We start by introducing the cluster number, n_s, representing the average (over all realizations) number of clusters with s particles; note that n_s depends on ρ and $\bar{F}$. From the percolation theory [69], we know that n_s at the percolation force threshold, f_p, can be characterized by the following scaling law

$$n_s \propto s^{-\tau}, \tag{4.1}$$

with the Fisher exponent τ. The percolation force threshold, f_p, is defined here as the one for which percolation probability is larger than 0.5, as in Chapter 3.

Using n_s, we can define the mean cluster size, $S(\bar{F})$, as

$$S(\bar{F}) = \frac{\sum_s' s^2 n_s}{\sum_s' s n_s} \tag{4.2}$$

where $\sum_s'$ denotes the sum over the non-percolating clusters of size s.

The scaling law for the mean cluster size, $S(\bar{F})$, is according to [69] given by

$$S(\bar{F}) = A\, N^{\phi} \mathcal{M}_2 \left(B\, (\bar{F} - f_c) N^{\frac{1}{2\nu}} \right), \tag{4.3}$$

where A, B are the coefficients independent of the system size, ϕ, ν are two critical exponents with $\phi = (3-\tau)/(\tau-1)$ and f_c is a critical force threshold found from collapse of rescaled S curves as described later. Note that f_p and f_c do not necessarily agree; we will discuss this issue later in the text. Here, N is the total number of contacts in the system, (excluding the contacts with the wall particles), and $\mathcal{M}_2(\cdot)$ is the second moment of the probability distribution of cluster size s. The question is whether there is an universal set of parameters $\phi,\ \nu$ such that the $S(\bar{F})N^{-\phi}$ curves obtained for different systems, collapse onto a single curve.

4.2.1 Computing Scaling Parameters

To find the exponents ϕ, ν and the parameter f_c, we follow the procedure similar to the one described in [52]. For a given simulation, we find the cluster number, n_s, for

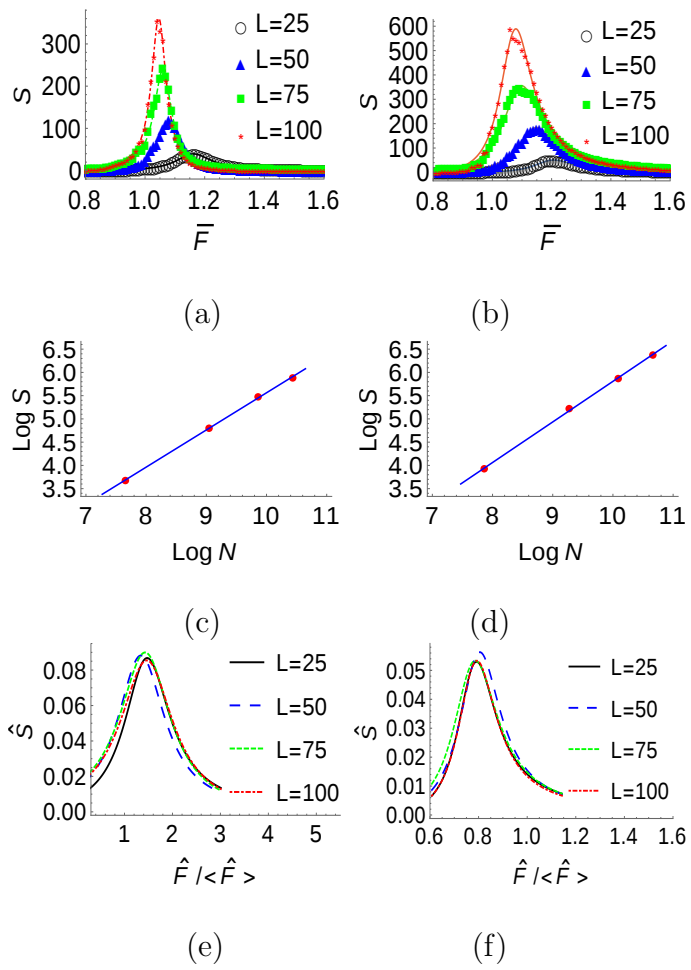

Figure 4.3 (a) Reference and (b) $r_p = 0.0, \mu = 0.0$ system at $\rho = 0.9$ showing (top to bottom) mean cluster size S; magnitude of the peak of S versus the total number of contacts, N, for different system sizes, L; and collapse of the rescaled curves, $\hat{S}$ vs. force threshold, $\hat{F}$, normalized by the rescaled average force, $\langle \hat{F} \rangle$ (see the text for definitions of the rescaled quantities). Note different range of axes in (a) and (b).

cluster size, s, ranging from $s = 1$ up to $s = N_p$, given a force threshold $\bar{F}$. The cluster search is performed over the range $\bar{F} \in [0, 5]$ with 501 discrete levels. Then, the mean cluster size, $S(\bar{F})$, is computed using Equation (4.2). The computation of n_s and $S(\bar{F})$ is performed for the systems characterized by (wall length) $L = 25,\ 50,\ 75,$ and 100, and for the discrete set of ρ's, such that $\rho > \rho_c$.

Figure 4.3(a) (top) shows an example of our results for $S(\bar{F})$ for various L's for the reference system at $\rho = 0.9$, averaged over 120 realizations. As expected, the magnitude of the peak of $S(\bar{F})$ is an increasing function of L: according to percolation

theory [69], $S \propto L^{\beta}$, $\beta > 0$ at the percolation threshold. We note from Figure 4.3(a) (top) that f_p (corresponding to the peak of the $S(\bar{F})$ curves [69]) is a decreasing function of L. For all systems and system size considered in the present work, the values of f_p are in the range $[1.05, 1.25]$.

From the magnitude of the peaks of $S(\bar{F})$, one can determine the optimal critical exponent ϕ; for $\mathcal{M}_2$ to be a "universal" curve regardless of the system size, $N^{-\phi}$ and $S(\bar{F})$ have to balance each other as L varies. The exponent ϕ is obtained from the linear regression through the peaks of $\log S(\bar{F})$ as a function of $\log N$. Figure 4.3 (middle) shows the values of peaks as a function of N in a log-log scale and a fit leading to a value of $\phi = 0.80 \pm 0.03$ within the 95% confidence interval.

Using the optimal value for ϕ, the remaining two parameters, f_c and ν, are determined by attempting to collapse the average $S(\bar{F})$ curves, such as the ones shown in Figure 4.3 (top), around the maxima. We define the (large) range of values of f_c and ν over which the search is carried out: $f_c \in [0.5, 2.5], \nu \in [0.5, 14]$ with a discretization step 10^{-2}. The search range for both parameters is chosen in a way such that we always find optimal values of f_c and ν; we verified that our results do not change if we assume larger range. For each L, we find the interval of force thresholds, $\bar{F} \in [a_L, b_L]$, for which $S(\bar{F}) \geq S_{\max}/8$, where $S_{\max} = \max\{S(\bar{F})\}$. The results are not sensitive to this specific choice of a_L and b_L. For each pair f_c, ν we take the common subinterval $[a', b'] = \cap[a'_L, b'_L]$ where $a'_L = (a_L - f_c)N^{1/(2\nu)}, b'_L = (a_L - f_c)N^{1/(2\nu)}$ are rescaled endpoints of the interval $[a_L, b_L]$.

The optimal values of f_c and ν are found by minimizing the error, err, defined by

$$err = \frac{1}{M} \sum_{m<n} \sum_{i=0}^{M-1} \left| \hat{S}_{L_m}(\hat{F}_i) - \hat{S}_{L_n}(\hat{F}_i) \right| . \tag{4.4}$$

$$\tag{4.5}$$

Here $L_m, L_n \in \{25, 50, 75, 100\}$ are different system sizes, $\hat{F}_i = \bar{F}_i N^{-1/(2\nu)} + f_c$

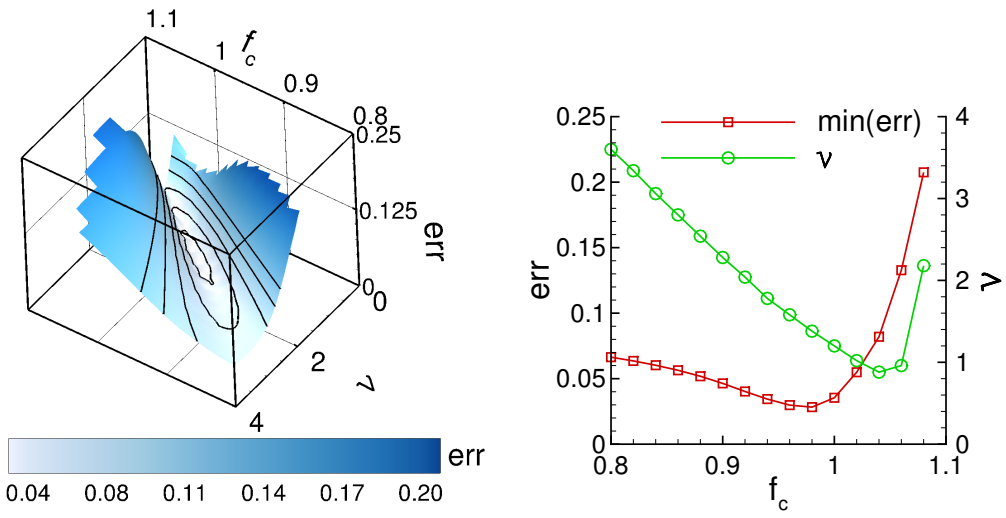

(a) (b)

Figure 4.4 Error plot for the reference system at $\rho = 0.9$: (a) *err* as a function of f_c and ν; the black lines are slices through different values of *err* and (b) minimum of *err* (red line with squares) as a function of f_c; here for each f_c value we choose ν that minimizes *err*; the used values of ν are shown by the green line with circles.

and $\hat{S}_{L_m}(\hat{F}_i) = S_{L_m}(\hat{F}_i N^{-\phi})$. We choose $\hat{F}_i = a' + id_F$ with discretization step $d_F = (b' - a')/(M-1)$ and $i = 0 \ldots (M-1)$ with total of $M = 100$ discretization points.

Note that the expression for *err* does not depend on the size of the interval over which the collapse of the curves is attempted.

Figure 4.3 (bottom) shows the collapse of the S curves as a function of the rescaled force threshold normalized by the average force threshold, $\hat{F}/\langle\hat{F}\rangle$; visual inspection suggests that indeed a good collapse was found and we continue by discussing the error using the optimal values of f_c, ν.

Figure 4.4(a) plots the contour of *err* as a function of f_c and ν for the reference system at $\rho = 0.9$. More precise information can be reached from Figure 4.4(b) that shows *err* and ν, that minimizes *err*, as a function of f_c. We find that *err* reaches a well defined minimum at $f_c \approx 0.98$ for $\nu \approx 1.38$.

4.2.2 The Scaling Exponent ϕ and the Fractal Dimension

Before discussing how the results for ϕ, ν, and f_c depend on the properties of the particles, we mention an alternative approach to compute ϕ. According to [69], ϕ is related to the fractal dimension, D_f, of the percolating cluster at the percolation threshold, f_p, as $1+\phi = D_f$. We compute D_f from the mass of the percolating cluster, using the Minkowski-Bouligand (or box counting) method. For each realization and each ρ, we divide the domain into square sub-domains of the size r, with r ranging from particle size up to L ($\approx$ 500 discretization steps are used). The number of sub-domains/squares, $\mathcal{N}(r)$, that we need in order to cover the area occupied by the percolating cluster scales as

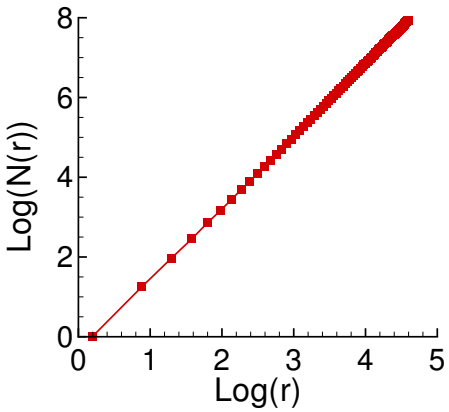

Figure 4.5 Number of subdomains covering the percolating cluster, $\mathcal{N}(r)$, as a function of the distance, r in log-log scale for the reference case at $\rho = 0.9$.

$$\mathcal{N}(r) \sim r^{D_f}. \tag{4.6}$$

To have a sufficiently large r, we compute D_f for the largest system size considered, with $L = 100$. Figure 4.5 shows r and $\mathcal{N}(r)$ in a log-log scale for the reference case and for $\rho = 0.9$ and $L = 100$. We find a good fit with $D_f = 1.783 \pm 0.016$. The value of D_f is computed as an average slope over 120 realizations and the error on D_f is computed as standard deviation.

For the present case, we find that D_f and ϕ are consistent; it is encouraging to see that the two independent procedures lead to the consistent results. Note also that the error in D_f is smaller than the one for ϕ; this is due to the fact that D_f is based on the properties of the percolating cluster that typically involves large number of particles, while the calculation of ϕ is based on smaller clusters. Therefore, the quality of data used for calculating D_f is in general much better.

We note that the values obtained for ϕ are significantly lower than those given in [52] (reported value $\phi \sim 0.9$), which is outside of the confidence interval for ϕ and D_f computed here. While it is difficult to comment on the source of this difference, it may have to do with the manner in which ϕ is computed in [52] - only a single domain size with $\approx 10,000$ particles was used, and then this domain was split into subdomains, with the largest subdomains discarded. The remaining subdomains contain relatively small number of particles, leading to potential inaccuracy of the results. Figure 4.6 shows the independently computed values for ϕ and D_f for the systems considered, and for the packing fractions above jamming, $\rho > \rho_J$; note that each of the considered systems (that differ by frictional properties and polydispersity) jams at different ρ_J, listed in the caption of Figure 4.6. Figure 4.6(a) shows that for the reference system, D_f and $1 + \phi$ are in general consistent for all ρ's considered, with slightly larger discrepancies close to ρ_J.

Figure 4.6(b) shows the results for D_f and $1+\phi$ for the $r_p = 0.0,\ \mu = 0.5$ system. Similarly as for the reference case, the values of $1+\phi$ and D_f are consistent (the results for ϕ and D_f, together with the values of ν and f_c are also given in Tables 4.1 and 4.2). However, for the frictionless systems, shown in Figure 4.6(c - e), we find that there is a notable discrepancy between $1+\phi$ and D_f. By comparing frictional and frictionless results, we note that the discrepancy comes from considerably smaller values of D_f for the frictionless ones. This is significant, since D_f can be computed very accurately

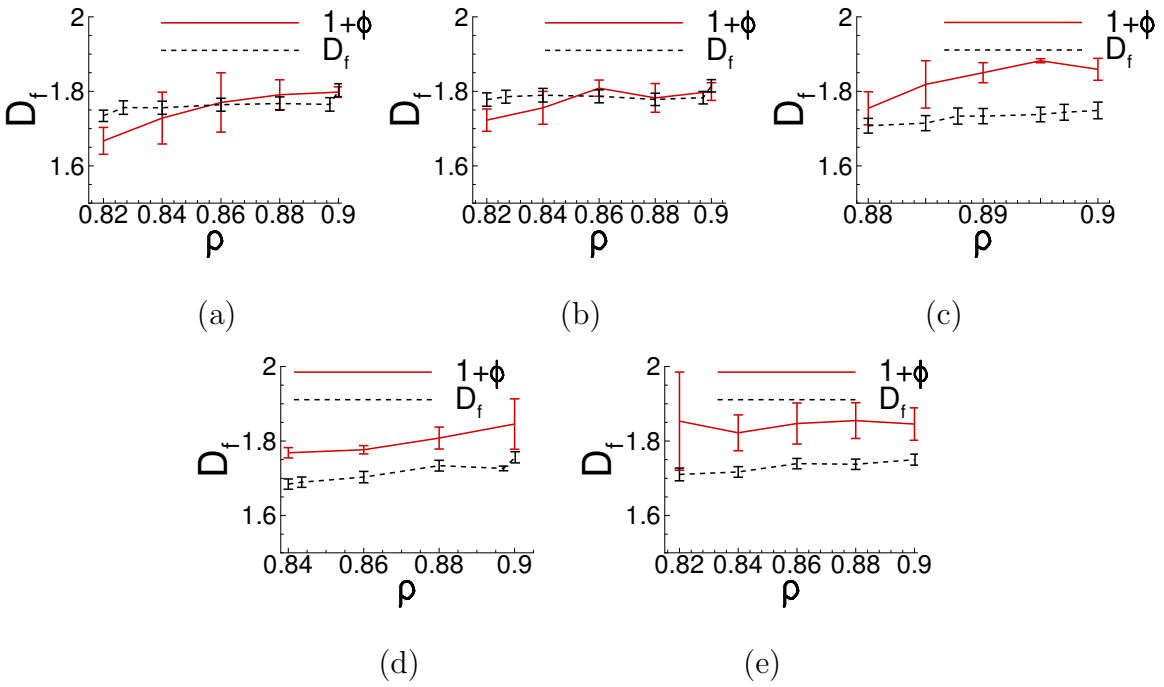

Figure 4.6 Fractal dimension, D_f, and scaling exponent $1 + \phi$ as a function of ρ: (a) $r_p = 0.0$, $\mu = 0.5$ (b) $r_p = 0.2$, $\mu = 0.5$ (reference system) (c) $r_p = 0.0$, $\mu = 0.0$, (d) $r_p = 0.2$, $\mu = 0.0$ and (e) $r_p = 0.4$, $\mu = 0.0$. For D_f, the error bars represent standard error; for ϕ, the error bars are derived from the accuracy of the fit, as explained in the text. The jamming packing fractions for the considered systems are $\rho_J =$ 0.804, 0.789, 0.861, 0.827 and 0.805, respectively (see Chapter 3).

for all packing fractions, showing clearly strong influence of friction on the fractal dimension.

4.2.3 Influence of the Friction and Particle Structure on the Properties of Force Networks

The obvious question is what is the source of such a large difference between frictional and frictionless systems? Is it the partial crystallization that may occur for frictionless systems, or the differences in underlying force networks that are independent of the geometric order? We note that the issue of the connection between the properties of force networks, inter-particle friction and particle ordering was considered in the literature on the level of force probability density function, see, e.g. [9, 41, 76] and also studied by using persistence analysis [38]; the influence of friction on jamming

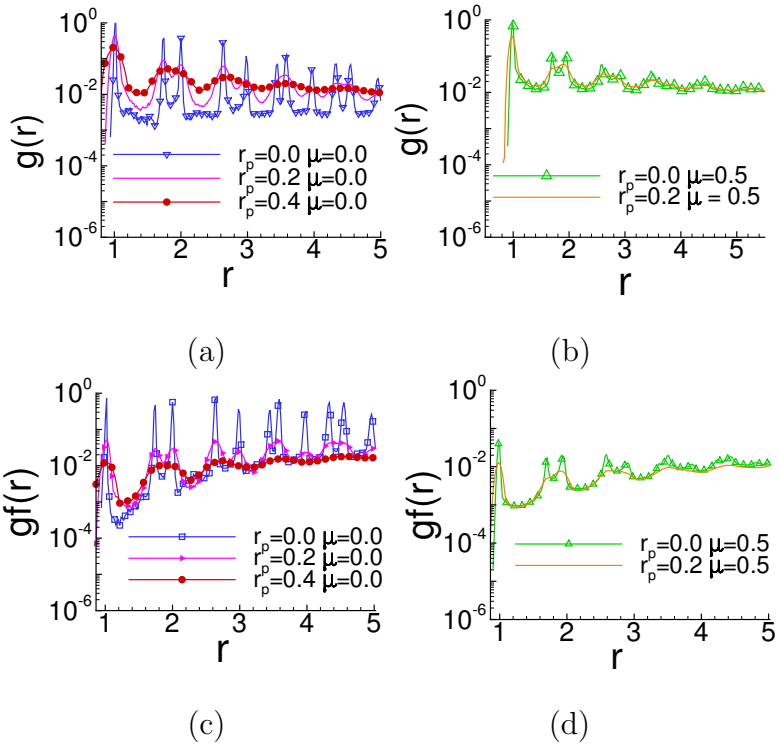

Figure 4.7 Pair correlation function, $g(r)$, and force correlation function, $g_f(r)$, at $\rho = 0.9$ for (a) frictionless systems, and (b) frictional systems.

transition was considered as well, see Chapter 3, or e.g. [8, 15, 81]. In the present context, the results given in this and the preceding section show that, in fact, friction itself (and not packing structure alone) is responsible for the breakup of universality.

We proceed by discussing the influence of friction and polydispersity on the structural properties of the considered systems. To start with, we focus on the level of crystallization in frictionless and frictional systems. For the largest packing fraction, $\rho = 0.9$, for all considered systems, we compute the pair correlation function, $g(r)$; the level of ordering of force networks is found from the force correlation function given by

$$g_f(r) = \frac{\sum_i \sum_{j>i} \delta\left(r_{ij} - r\right)\left(F_i - < F >\right)\left(F_j - < F >\right)}{\sum_i \sum_{j>i} \delta\left(r_{ij} - r\right)} \tag{4.7}$$

where F_i denotes the total normal force on i-th particle and r_{ij} is the distance between the particles i, j. Figure 4.7 shows $g(r)$ and $g_f(r)$, averaged over 120 realizations. We

observe a pronounced first peak of $g(r)$ and $g_f(r)$ and a clearly split second peak, which is a sign of crystallization [74], for frictionless systems with $r_p = 0.0, 0.2$. For $\mu = 0.0$ and large polydispersity parameter, $r_p = 0.4$, and for frictional systems, the first peak of $g(r)$ and $g_f(r)$ is less pronounced and clearly there is a smaller long-range correlation for both $g(r)$ and $g_f(r)$. We note that a choice of $r_p = 0.4$ for $\mu = 0.0$ guarantees that the system is not crystallized, and we can thus separate clearly the influence of the structural order and the influence of friction on our results.

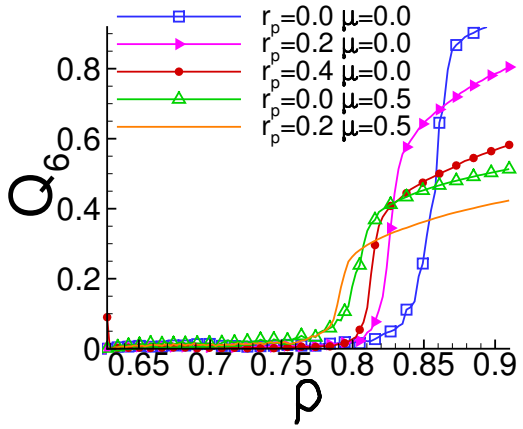

Figure 4.8 Order parameter showing distribution of the angles between contacts.

Next we discuss Q_6, that measures the distribution of the angles between contacts, defined by

$$Q_6 = \frac{1}{N_p} \sum_i \frac{1}{C_i - 1} \sum_{k=1}^{C_i - 1} \cos(6\theta_k). \tag{4.8}$$

Q_6 is a measure of the six-fold symmetry between contacts: here N_p is the total number of particles, C_i is the number of contacts for the i-th particle, and θ_k is the angle between two consecutive contacts. Note that Q_6 is equal to 1 for a perfect hexagonal crystal. Figure 4.8 shows the results averaged over all realizations. For small ρ's, Q_6 is small for all systems, but then, as the systems go through their respective jamming transitions, Q_6 grows. For $\rho > \rho_J$, we observe that the frictionless systems, in particular the monodisperse one, are the most ordered, consistently with

the results obtained by considering $g(r)$ and $g_f(r)$. We also confirm our conclusion that the frictionless $r_p = 0.4$ system does not posses a structural order and is characterized by Q_6 that is similar to the ones found for the frictional systems.

To conclude this section, we find that frictionless systems that are built of strongly polydisperse particles do not lead to an ordered structure under slow compression. These systems, while disordered, lead to force networks that are non-universal in the sense that their fractal dimension, D_f, and the scaling exponent, ϕ, are not consistent. This being said, one could ask whether ordered frictional systems lead to universality. As suggested in the Introduction, this is not expected to be the case. To confirm this expectation, we carried out additional simulations where we arranged frictional particles on a hexagonal lattice and exposed them to the same compression protocol (figures not shown for brevity). We find that the simulations carried out with different system sizes produce inconsistent results, showing lack of universality, as expected.

The other scaling parameters for these systems are discussed further below in Sec. 4.2.5. Before that, we discuss some additional aspects related to the comparison of the scaling exponent ϕ and the fractal dimension.

4.2.4 Further Discussion of the Results for ϕ and Fractal Dimension

Here we discuss briefly two effects that could potentially influence the results presented so far: non-vanishing compression rate, and the differences in ρ_J for the systems considered.

In Chapter 3, we showed that the compression speed influences percolation and jamming transitions, so it is appropriate to ask whether our scaling results are influenced by non-vanishing compression rate. For this reason, we also consider relaxed systems, where we stop the compression and relax the particles' velocities every $\Delta\rho = 0.02$, following the same protocol as presented in Chapter 3. We then

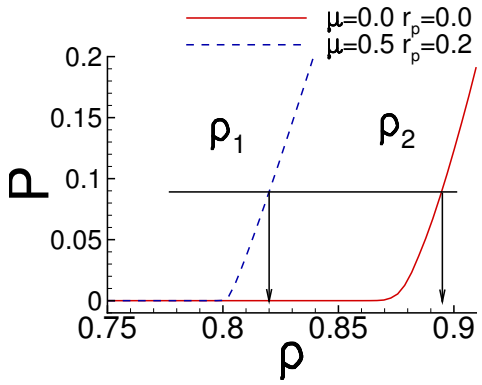

Figure 4.9 The pressure, P, on the the domain boundaries as a function of ρ for the reference and for $r_p = 0.0, \mu = 0.0$ system; ρ_1, ρ_2 correspond to the same pressure in reference and $r_p = 0.0, \mu = 0.0$ system, respectively.

compute $1 + \phi$ and D_f using the same approach as discussed so far, and find that the values are consistent with the ones presented (figures not given for brevity). This finding is not surprising since here we focus on the systems above their jamming transitions. For such ρ's, consistently with the results given in Chapter 3, there does not seem to be any rate dependence of the results, at least for the slow compression considered here.

We further examine whether the inconsistency of the results for ϕ and D_f for the frictionless systems might arise from the proximity to the jamming transition. As noted above, ρ_J differs significantly between the considered systems, and it reaches particularly large values for the frictionless ones. Since we are comparing different systems, we need to confirm that they are all in the same regime, so sufficiently far away from ρ_J. As a measure, we consider here the (dimensionless) pressure, P (computed as the average force per length) on the domain boundaries. For the sake of brevity, we focus on two representative systems here, the reference one, and the $r_p = 0.0, \mu = 0.0$ system. Figure 4.9 shows P as a function of ρ for these two systems, averaged over all realizations. Since the reference system jams for much smaller ρ, P starts growing earlier. For definite comparison, consider a particular packing fraction, $\rho_1 = 0.82$ for the reference system: at this ρ, P is non-zero, and Figure 4.6

and Table 4.1 show that ϕ and D_f are consistent. Consider now $r_p = 0.0, \mu = 0.0$ system at the packing fraction $\rho_2 = 0.895$ that corresponds to the same pressure. At this ρ, Figure 4.6(c) shows inconsistent values of ϕ and D_f. We conclude that the difference in the results obtained from two different methods - scaling versus fractal dimension - for frictionless monodisperse system does not arise from the proximity to a jamming transition.

4.2.5 Continuation of the Discussion of Scaling Parameters

We continue with the discussion of remaining scaling parameters, f_c and ν, found by minimizing *err* (the distance between the $\hat{S}$ curves) for different L's. Table 4.1 shows f_c and ν as a function of ρ for the considered frictional systems. While the value of f_c is almost constant, ν shows the same decreasing trend with increasing ρ for both considered frictional systems. We note, however, that the results for ν are different for monodisperse and polydisperse system: for the reference (polydisperse) case and sufficiently high ρ, we find $\nu \approx 1.5$, consistently with [52]. However, $r_p = 0.0, \mu = 0.5$ gives $\nu \approx 2$. Note also that for $r_p = 0.0$, $\mu = 0.5$ system and for $\rho = 0.82$ rather large *err* is found, suggesting larger inaccuracy in the (very) large optimal value of ν.

Table 4.1 The Results are Shown for D_f, f_c and Scaling Exponent ν for the Frictional Systems; the Value of *err* Gives an Estimate of the Accuracy of the Collapse.

$r_p = 0.0$					$r_p = 0.2$					
0.82	0.84	0.86	0.88	0.90	ρ	0.82	0.84	0.86	0.88	0.90
0.76	0.96	0.96	0.96	0.96	f_c	1.06	1.0	0.98	0.98	0.98
13.94	2.72	2.12	1.98	1.84	ν	1.68	1.7	1.54	1.48	1.38
1.73	1.77	1.78	1.77	1.80	D_f	1.78	1.80	1.79	1.78	1.81
0.67	0.73	0.77	0.79	0.80	ϕ	0.72	0.75	0.80	0.78	0.80
0.13	0.09	0.06	0.04	0.04	*err*	0.06	0.05	0.02	0.03	0.03

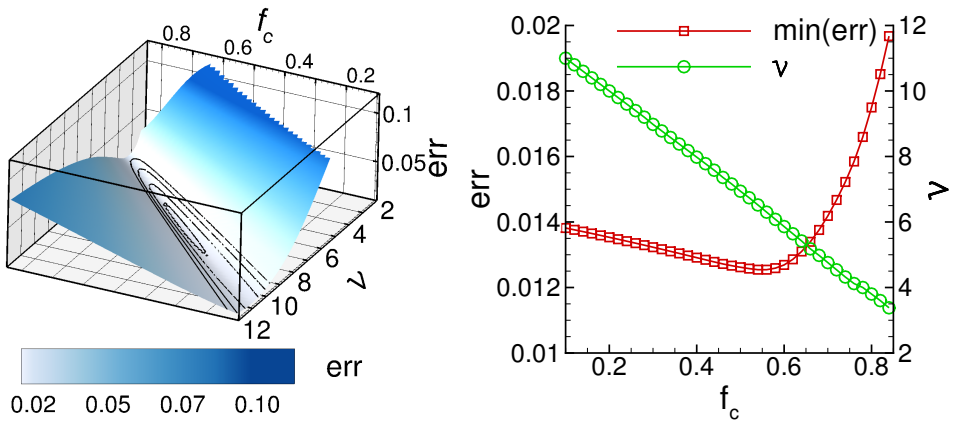

(a) (b)

Figure 4.10 Error plot for $r_p = 0.0, \mu = 0.0$ system at $\rho = 0.9$: (a) err as a function of f_c and ν; the black lines are slices through different values of err and (b) minimum of err (red line with squares) as a function of f_c; here for each f_c value we choose ν that minimizes err; the used values of ν are shown by the green line with circles. Note different range compared to Figure 4.4.

Next we proceed with discussing the scaling exponents for frictionless systems. As an example, Figure 4.10 shows err for the $r_p = 0.0$, $\mu = 0.0$ system at $\rho = 0.9$ (Figure 4.4 shows the corresponding plots for the reference system). Direct comparison of these two figures shows the following: (i) the collapse appears to be much better for the considered frictionless system (the minimum value of err is smaller); (ii) the optimal values of f_c, ν are significantly different: ν is much larger, and f_c is much smaller for $r_p = 0.0$, $\mu = 0.0$ system. We note that the minimum of err curve in Figure 4.10(b) is not as clearly defined as for the reference system, introducing some inaccuracy in the process of finding optimal values of f_c, ν. However, as it can be clearly seen in Figure 4.10(b), this inaccuracy still limits f_c to a very small value, $f_c < 0.6$, and ν to a very large value, $\nu > 6$.

Figure 4.10 suggests some significant differences between $r_p = 0.0$, $\mu = 0.0$ and the reference system at $\rho = 0.9$. Table 4.2 shows that the differences are present for other considered packing fractions as well. In particular, we always find large values of ν and very small values of f_c for $r_p = 0.0$, $\mu = 0.0$ system. Small overall values of

Table 4.2 The Results are Shown for D_f, f_c and Scaling Exponent ν for the Frictionless Systems; the Value of *err* Gives an Estimate of the Accuracy of the Collapse.

$r_p = 0.0$				
0.88	0.885	0.89	0.895	0.90
0.22	0.56	0.60	0.66	0.54
13.96	8.76	6.84	5.48	6.52
1.70	1.71	1.73	1.74	1.75
0.81	0.82	0.86	0.89	0.87
0.02	0.02	0.01	0.01	0.01

$r_p = 0.2$				
ρ	0.84	0.86	0.88	0.90
f_c	1.18	1.1	1.08	1.06
ν	1.58	1.44	1.28	1.22
D_f	1.68	1.70	1.73	1.76
ϕ	0.77	0.78	0.80	0.84
err	0.01	0.01	0.08	0.01

$r_p = 0.4$					
ρ	0.82	0.84	0.86	0.88	0.90
f_c	1.34	1.08	1.08	1.04	1.04
ν	5.56	1.38	1.04	1.2	1.06
D_f	1.71	1.72	1.74	1.74	1.75
ϕ	0.85	0.85	0.85	0.82	0.85
err	0.08	0.1	0.07	0.07	0.07

err are a sign of a good quality of the collapse. We note again that for the smallest ρ, the optimal values of f_c and ν are different from the rest, suggesting that scaling properties of force networks very close to jamming transition may differ.

One obvious question to ask is what causes a particularly large difference between f_c and f_p for $r_p = 0.0,\ \mu = 0.0$ system (recall that typically $f_p \in [1.05, 1.25]$). One possibility is that it may be caused by a finite system size. Note that the percolation threshold in a finite size system, f_p, is related to the one of the infinite size system, f_p^{∞}, by [69]

$$|f_p - f_p^{\infty}| \sim L^{-1/\nu} \tag{4.9}$$

and $f_p^{\infty} < f_p$. This relation suggests a strong influence of the system size on f_p for large values of ν, such as those we are reporting in Table 4.2 for $r_p = 0.0,\ \mu = 0.0$ system. Therefore, our conjecture is that the agreement of f_c and f_p could still be found if very large system size are considered. In particular, if we assume that f_c is close to f_p^{∞}, the values of $f_c,\ f_p$ would be for a very large system both in the range $[0.5, 0.7]$ for $r_p = 0.0,\ \mu = 0.0$ system (see Table 4.2).

We close this section by pointing out that ν could in principle be computed using alternative approaches. One avenue is to use Equation (4.9); the value of f_p is found as an average percolation threshold for each L and plotted against the natural logarithm $\log(L^{-1/\nu})$; the slope of the linear fit should correspond to $-1/\nu$. However, we find that the error of the linear fit is large, leading to the results that are less accurate than the ones already obtained. Alternatively, we could estimate ϕ from the Fisher exponent τ, see Equation (4.1), and the relation $\phi = (3 - \tau)/(\tau - 1)$. The results for ϕ obtained in this manner are again characterized by large error bars. We note that while both of the outlined approaches lead to the results that are inaccurate, they are still consistent with the ones found by scaling.

4.2.6 Physical Experiments: ϕ and Fractal Dimension

In this section we report the results of physical experiments carried out with photoelastic particles, made from the PSM-1 sheets obtained from Vishay Precision Group; details about the material properties of these particles could be found in [17]. Figure 4.1 shows the experimental setup that consists of two plexiglass plates with a thin gap in between. The size of the gap is slightly larger than the thickness of the particles. The domain is bounded by four walls, one of which is removable and can slide in and out. The experimental protocol consists of placing the particles in the gap, mixing them up, and than replacing the removable wall and gently applying desired pressure by a certain number (1 - 5) of rubber bands. The applied pressures

lead only to modest inter-particle forces. For each pressure, 5 realizations are carried out.

The stress on the particles is visualized using cross-polarizers (see Figure 4.1(b)). The photographs are processed using the Hough Transform [22] image processing technique to detect particles. From the brightness of the particles, the total stresses are computed via G^2 method used extensively by Behringer's group (see, e.g. [16]). The experiments are carried out using three particle sizes of diameters 0.58, 0.46 and 0.41 cm. We consider a monodisperse system (with medium particles only) and two bidisperse ones that use large/medium and large/small particles. For bidisperse systems, we always use equal area fraction of particles of different sizes. Approximately $1,000$ particles are used in total.

The obtained data are processed similarly to the ones resulting from the simulations, with the difference that here we focus on the magnitude of the total stress on a particle, instead on contact forces, as in simulations. Since only a single domain size is available, the domain is divided into 4, 8 and 16 smaller sub-domains of $1/4, 1/8$ and $1/16$ of the original domain size. D_f and ϕ are then computed using the box-counting method and by fitting the peaks of S-curves, respectively. In what follows we focus on these two quantities only, since they could be obtained with a reasonable accuracy using available resources.

Figure 4.11 shows D_f and $1 + \phi$ computed from the experimental data. We note that while D_f is consistent for the whole range of pressures applied and for all experimental setups, the value of $1 + \phi$ has a larger variation, similarly as for the results obtained from the simulations. Since the number of realizations used for the experiments is much smaller, relatively large standard error is observed in the results. Still, the experiments yield D_f and ϕ that are consistent with the results obtained from the simulations carried out with frictional particles. This is encouraging, in particular since the protocols in simulations and experiments differ (e.g., controlled

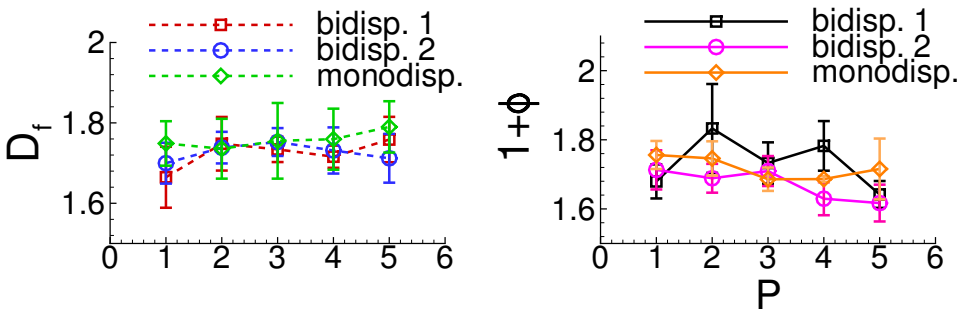

(a) (b)

Figure 4.11 (a) Fractal dimension, D_f, and (b) $1 + \phi$ obtained from experiments carried out with photoelastic particles as a function of the applied pressure. Bidisperse 1 and 2 refer to the systems of large/medium and large/small particles, respectively (see the text).

pressure versus controlled packing fraction, additional friction between the particles and the substrate in experiments, that is not present in simulations); in addition, we have not attempted to precisely match the simulation parameters with material properties of the particles. The consistency of the results therefore suggests that they are independent of the protocol and of the material properties, at least for the applied pressures considered. We emphasize in particular that both simulation and experimental results lead to D_f and ϕ that are significantly smaller than the previously proposed value of $\phi \approx 0.9$ [52].

4.3 Conclusions

In this chapter we focus on the scaling properties of force networks in compressed particulate systems in two spatial dimensions. To complement the results obtained by exploring scaling properties of the force networks, we also calculate the fractal dimension. For disordered frictional systems, we find that the scaling exponent, ϕ, and the fractal dimension, D_f, are consistent over a range of considered packing fractions, ρ. The computed values are, however, significantly lower than the previously proposed ones, and in particular we find that $D_f \approx 1.8$. This value is consistent with

the ones extracted from the physical experiments involving two dimensional systems of monodisperse and bidisperse frictional particles exposed to compression. We note that the reported experimental results are based on stresses, and not on the contact forces; it would be very much of interest to carry out additional experiments where individual contact forces would be resolved, and compare the results to the findings reported here.

Another significant finding is that the proposed universality of the force networks does not appear to hold for frictionless systems: in particular, for such systems the results for the scaling exponent, ϕ, and the fractal dimension, D_f, are not consistent. By considering strongly polydisperse frictionless systems that do not crystallize, we show that it is friction itself, and not partial crystallization (alone) that breaks universality. Therefore, we show that frictionless systems do not belong to the same (if any) universality class as the frictional ones. This being said, we have also shown that partial structure (that appears spontaneously for frictionless systems with sufficiently small range of the particle sizes, or can be induced 'by hand' for frictional ones) also leads to breakup of universality: therefore, *both friction and disorder are needed for force networks to show universality.*

These results open new directions of research, including working towards understanding the conditions under which scaling properties of force networks are at least consistent if not universal. Another question is how our findings extend to three dimensional systems. And finally, how the scaling properties of the force networks relate to the macroscopic properties of the underlying physical systems.

CHAPTER 5

CHARACTERIZING GRANULAR NETWORKS IN SHEARED SYSTEMS

5.1 Introduction

In preceding Chapters 3 and 4, we analyze compressed granular systems confined within a rectangular box. During the compression that starts at a low packing fraction (recall that we start the compression at $\rho \approx 0.64$), we observe a phase transition from a dilute to a dense state with many contacts per particle (typically > 4). In this chapter, we consider a different protocol that leads to a jammed state of the particulate system. Specifically, instead of compression, we apply shear to a granular system.

In [8] it is shown that sheared systems are particularly interesting since the phase transition from the unjammed to the jammed state can be invoked by shear alone while keeping the packing fraction constant. Before the jamming due to shear occurs, the force networks, composed of forces above mean force, start to form in the direction of shear. Such networks, referred to as fragile force networks, percolate and are able to support load in the compression direction. Any external load or infinitesimal shear in the dilational direction breaks the fragile force networks and causes particle rearrangement. If the system is further sheared, strong forces start to propagate in all directions and jamming occurs.

In this chapter, we consider statistical and topological properties of a linearly sheared granular system that undergoes shear jamming transition and characterize the evolution of the force networks and physical measures such as stress and pressure. First, we introduce alternative ways to characterize the force networks on the microscopic spatial scales and then we continue the discussion of the force network

properties in terms of the system-wide measures. We show that the force networks provide the connection between micro and macro properties. In the second part of this chapter, we focus particularly on the sensitivity of various topological and physical measures to small changes in the system. We present the key results from the experiments, performed at Duke University, and simulations that carefully reproduce the experimental conditions. As it turns out, the conventional measures, including stresses and contact numbers, are similar for the experiments and simulations, and are insensitive to small differences between the two. However, we find that the topological measures given by Betti numbers show high sensitivity to small differences between experiments and simulations. The computation of the Betti numbers is performed by the collaborative group at the Rutgers University, led by prof. Mischaikow.

To motivate the use of topological techniques, let us first consider the following situation for the compressed systems (analyzed in Chapters 3 and 4). At the beginning of the simulations we have a low packing fraction, $\rho \approx 0.64$, and we observe formation of many, mostly small, clusters in the system. As we compress the system further, the particles start to form larger clusters; the number of clusters is decreasing with increasing mean cluster size, S. In Chapter 4 we analyzed S as a function of force threshold, f_c, and probed the universality of the scaling law for S. A different approach to examine the clusters in the force networks is to use simple topological measures, also referred to as the Betti numbers. In topology, the zero-th Betti number, β_0, measures the number of connected components, which in granular systems are clusters of particle contact forces (possibly above given force threshold). The first Betti number, β_1, counts the number of holes in the network. It was shown [35] that β_0 and β_1, unlike traditional measures, are sensitive to small changes in the strong force structure evolution after the system is jammed and continues to be compressed to high packing fractions. Here, we use β_0 and β_1 to quantify the difference between the numerical simulations and experiments.

5.2 Linear Shear: Experiments and Simulations

The experimental setup [7] consists of ~ 1000 cylindrical photoelastic particles placed randomly within a rectangular box of length 622.3 mm and width 297 mm; the particles are of two different sizes, with diameters 15.9 mm and 12.7 mm, respectively. The ratio of the number of large to the number of small particles is $\approx 1 : 3$. The density of the photoelastic disks is 1.04 g/cm^3 and the particle stiffness is characterized by Young's modulus $E = 3.45 \times 10^6$ Pa. The interparticle friction coefficient is $\mu = 0.7$ and the coefficient of friction with the base is $\mu_b = 0.4$.

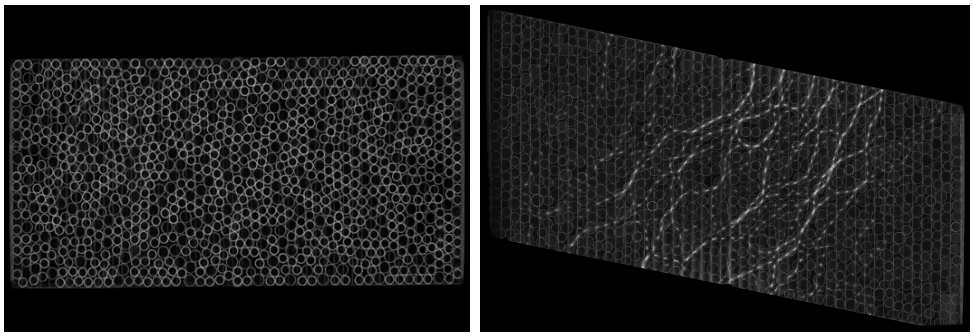

(a) (b)

Figure 5.1 Experimental setup of the linearly sheared system (a) prior to linear shear and for (b) sheared system [7].

The bottom surface of the rectangular box is divided into the slats that move in the direction of shear. The slat's purpose is to minimize the effect of boundaries and maximize the effect of shear; without their presence, the particles would bundle up in the corners of the box that encapsulates the whole system. During the experiment, the side walls are sheared by moving the left wall up and the right wall down. This causes upper and bottom walls to rotate around their centers during the shear. Shearing process is performed by 0.27% strain steps where the strain is defined as the ratio $\Delta x/L$ where Δx is a displacement of the bottom left endpoint of rectangle from its original position and L is the length of a side wall. After performing a shear step, the system is relaxed until the particles stop moving and a snapshot of the system is

taken for further analysis. This process of shearing and relaxing is performed up to the final maximum shear strain of 27%. Figure 5.1(a) shows the experimental system of the particles before shearing starts and Figure 5.1(b) shows the system at the shear strain $\approx 20\%$. In the latter, we can observe the strong forces (thick white segments between particles) and their directionality towards the compression direction. We note that the experiments cannot detect the contact forces below ≈ 0.1N and therefore (as described later in the text) we will need to adjust the results for numerical simulations by excluding the forces below this threshold.

In the following, we describe the numerical simulations that are set up to mimic the experiments as closely as possible in both protocol and physical parameters. The granular system in simulations has a rectangular shape with walls composed of monodisperse particles with a diameter $d = 12.7$ mm, corresponding to the size of the small particles in the experiments. The length of the top/bottom wall is $L = 47d$ and the distance between the top and bottom wall (height of the system) is $H = 27d$. System particles are bidisperse; the ratio of the numbers of small and large particles is kept the same as in the experiments; the diameter of the large particles is $15.9/12.7d$. We use the same force model for the particle-particle interaction as outlined in Appendix A, formulated in terms of the binary collision time, τ_c, typical system particle size, d, and mass, $\bar{m}$, here corresponding to the values for the smaller particles (matching the experimental values for photoelastic disks). The value of the force constant, k_n, can be determined from the Young's modulus, Y, and Poisson ratio, σ, set to the corresponding value from experiments, in the following way. From the expression for the binary collision time, τ_c, we have (see Appendix A) $k_n = 0.5\bar{m}\pi/\tau_c^2$ and from [33]

$$\tau_c = I(\beta)\left(1+\frac{\beta}{2}\right)^{1/(2+\beta)}\left(\frac{\bar{m}}{E(2R)^{1-\beta}}\right)^{1/(2+\beta)} v_0^{-\beta/(2+\beta)} \tag{5.1}$$

where $E = 2Y[3(1-\sigma^2)]$ and v_0 is the typical impact velocity of the particles during collision. For the linear force model, we have $\beta = 0$ [31] and $I(\beta) = I(0) = \pi$. Then, after substituting for E, β and $I(\beta)$, the value of τ_c is

$$\tau_c = \pi \left(\frac{\bar{m}}{4Y[3(1-\sigma^2)]R)} \right)^{1/2} \tag{5.2}$$

Note, that since $\beta = 0$, we lost dependence on v_0. Using the value of τ_c we compute k_n. The coefficient of restitution in the simulations is set to $e_n = \exp(-\tau_c \gamma_n/2) = 0.5$ where the value of γ_n measures the strength of viscous damping [33]. For the interparticle friction, μ, we use the experimental value of 0.7, and $k_t = 6/7 \times k_n$ (close to the value used in [25]).

To simulate the slats present in the experiments, we assume that the base moves with a linear velocity corresponding to the velocity profile of the moving walls. We also consider the friction between particles and the base as follows. The force between the particle and the base has a translational and a rotational component and the particle-base friction coefficient is $\mu_b = 0.4$ (corresponding to the experimental value). The magnitude of the deceleration of the particle in the translational direction due to the friction with the base is $\mu_b |\mathbf{g}|$ where $\mathbf{g}$ is a rescaled (dimensionless) gravitational acceleration. The magnitude of the rotational deceleration of the i-th particle due to friction with the base

$$|\alpha_i| = \frac{4}{3} \mu_b \frac{|\mathbf{g}|}{r_i} \tag{5.3}$$

is computed by integrating the torque arising from the friction with the base and using moment of inertia of the disk, $I = (m_i r_i^2)/2$, where m_i, r_i are the dimensionless values of mass and radius of the i-th particle, consecutively. For simplicity, we use $r_i = 2/3$ for both small and large particles.

In the simulations, the particles are initially placed on a rectangular lattice and are given random velocities. The domain is slowly compressed by moving the walls

inwards at a constant dimensionless speed, $v_0 = 2.5 \times 10^{-5}$. After reaching desired packing fraction, the system is relaxed until the average particle speed is smaller than $10^{-5}v_0$ and then sheared by moving the left wall in the positive and the right wall in the negative direction. Relaxation is interjected after each strain step of 0.27% until we reach the maximum strain amplitude of 27%. Figure 5.2 shows a granular system in the simulations for the packing fraction $\rho = 0.77$ at the $\approx 20\%$ strain. The particles are color coded according to the total normal force on each particle normalized by the average normal force, $\langle \mathrm{F^n} \rangle$.

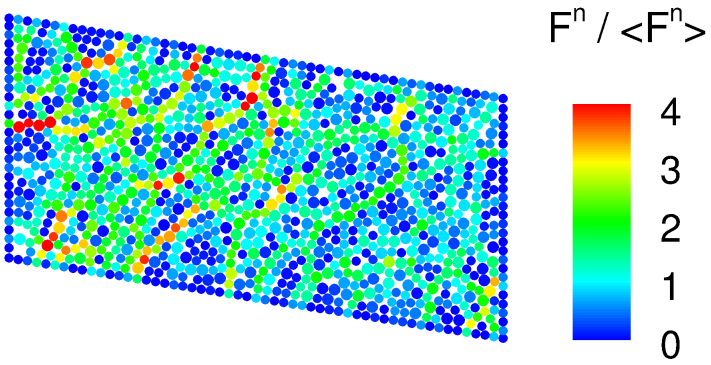

Figure 5.2 Linearly sheared granular system at $\rho = 0.77$; the strain is approximately 20%. Color scale shows the normalized magnitude of the total normal forces acting on the particles.

After each relaxation, we output all the information needed for comparing with the experiments. We compute the Cauchy stress tensor (defined by Equation 3.2 in Chapter 3), σ, average contact number, Z, and fraction of the non-rattlers, f_{NR}, defined as the ratio of the number of particles with at least two contacts and the total number of particles.

From the Cauchy stress tensor, we define the pressure, P, and the stress anisotropy, τ_a, as

$$P = \frac{\sigma_1 + \sigma_2}{2} \tag{5.4}$$

$$\tau_a = \frac{\sigma_1 - \sigma_2}{\sigma_1 + \sigma_2} \tag{5.5}$$

where σ_1, σ_2 are the principal eigenvalues of σ. In the simulations and also in the experiments, the initial condition for the granular system is random and stress free (and therefore unjammed before shear). In the case of experiments, the range of packing fractions below the jamming point that lead to the shear jamming is $\rho \in [0.75, 0.825]$. In the case of numerical simulations, we obtain a slightly different range, with $\rho \in [0.76, 0.775]$. This difference in relevant packing fractions between experiments and simulations is not clear at this point and should be explored in the future work. Shear jamming occurs when the system develops the non-zero stress and pressure [8]. The onset of the jamming is very sensitive to the interparticle friction; larger value of μ leads to smaller value of ρ_J (jamming point) [36] for compressed systems and therefore if we want to prepare the system in a stress free state, we are limited by ρ_J from above. It is, however, important to notice that we obtain a good agreement between the simulations and the experiments in terms of different measures (discussed below) if we shift (increase) the values for numerical simulations by $\rho = 0.02$. Therefore in what follows, we present the results with the value of ρ shifted by 0.02 in the simulations. Figure 5.3 shows the comparison of the force networks in experiments and simulations (note that by visual inspection, it is difficult to distinguish between the two). For each of the packing fractions, we carry out five different realizations with different initial conditions and average the results.

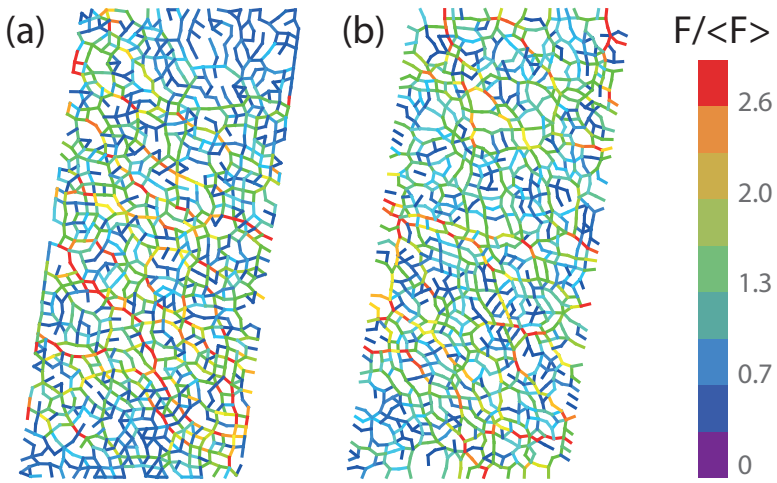

Figure 5.3 Force networks of the linearly sheared system for (a) experiments and (b) simulations at $\approx 15\%$ strain.

5.3 Direct Comparison of the Numerical and Experimental Results

We start the comparison between the simulations and experiments in terms of the traditional measures, such as the average contact number per particle, Z, and later, we show the pressure in the system, P, and the force network anisotropy. The simulation results shown in this section are found to describe well the experiments when we add a positive random noise to the contact forces chosen from a flat distribution $[0, 0.2$ N$]$. The reason for the noise addition is explained in detail in Section 5.4, where we analyze the topological measures of force networks. For now, we note that the traditional measures considered in this section are not significantly influenced by the addition of the random noise. Recall that in experiments, the forces below ≈ 0.1 N are not detected and therefore we also apply a force cutoff to the numerical results.

To motivate the choice of the contact number (as a traditional measure), we notice that using Z we can determine the minimum requirement for the particle stability; for the frictional particles, we need at least $D + 1$ contacts per particle to guarantee the isostaticity [68], where D is the system dimension. For 2D frictional disks, we therefore need $Z \geq 3$ to create a stable packing.

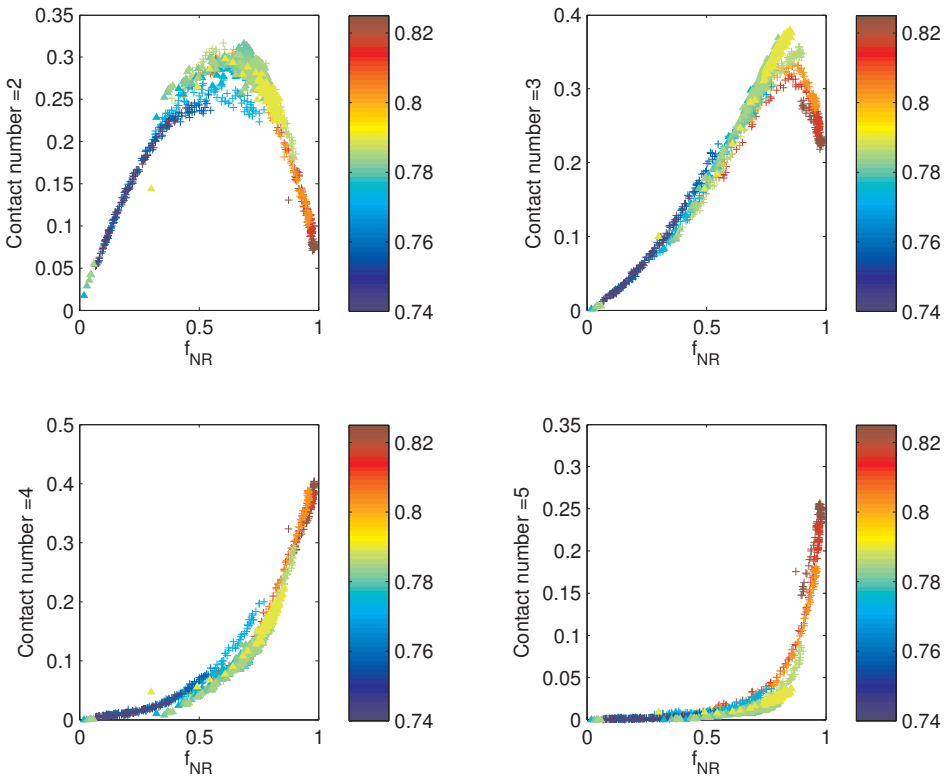

Figure 5.4 Comparison of contact numbers as a function of f_{NR} between the experiments (+) and simulations ($\triangle$) of the two dimensional sheared system. The packing fraction, ρ, is shifted by 0.02 in simulations; the colors correspond to the different values of ρ.

The force chains in the jammed (and unjammed) sheared systems contain particles that have two to six contacts. Therefore we do not measure Z, but we find $Z_n(\rho, \gamma)$, defined as the fraction of particles that have n contacts. In [8] it was shown that there is a universal curve that describes Z as a function of f_{NR} regardless of the value of ρ. In other words, for any ρ, we can determine Z if we know the value of f_{NR}. We show that the universality is also observed here in both the experiments and simulations for all $Z_n(\rho, \gamma)$.

Figure 5.4 shows the data for $Z_{2,3,4,5}$ as a function of f_{NR}. There are two outstanding features in this data:

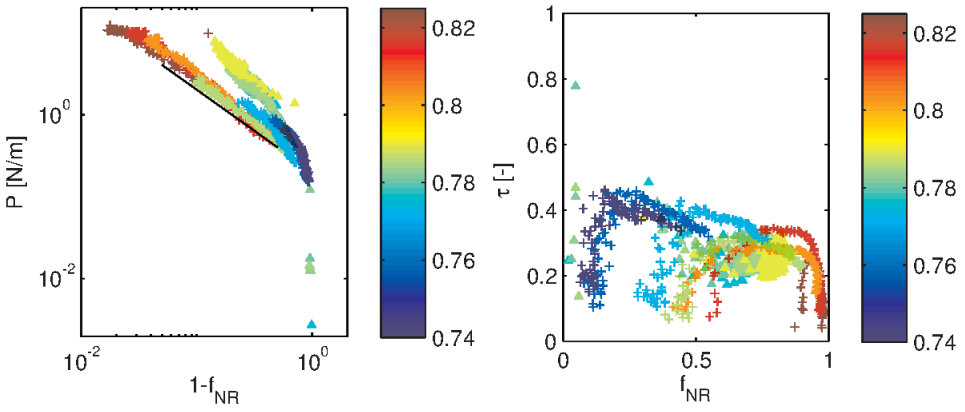

(a) (b)

Figure 5.5 (a) Pressure evolution versus 1-f_{NR} for both experiments (+) and simulations ($\triangle$). Numerical f_{NR} values have been corrected to account for the experimental cutoff of about 0.1N in the force detection. The black lines indicate a slope of -1. (b) The evolution of the anisotropy, τ_a, as a function of f_{NR}.

(i) the values for all Z_n collapse on a single curve when expressed as a function of f_{NR}

(ii) the agreement between experiments and simulations is quantitative (apart from a shift in ρ).

In addition, the evolution of the pressure and shear stress is also described very well in terms of f_{NR}, even though the range of mechanically different states probed in the experiments is large. That is, the data are obtained over a range of ρ's for which the stresses vary significantly, as shown in Figure 5.5 (a), (b) for both the experiments and simulations. We conclude that the simulations reproduce the experimental reality well, and also that in the current setup, f_{NR} can be used as a variable to describe the state of the system.

Our observations go beyond the results presented so far: the pressure, P, shows a power law behavior as a function of $1-f_{NR}$. Intuitively, the inverse relation between P and f_{NR} makes qualitative sense: the larger the fraction of rattlers, $1-f_{NR}$, the smaller the pressure. However, the power law nature of this relation is not trivial.

Quantitatively, we observe $P \propto (1 - f_{NR})^{\alpha}$ with $\alpha = -1 \pm 0.1$ for the experiments. For the simulations, we find an excellent collapse of P vs. $1 - f_{NR}$, via a power-law, although the exponent is higher than for the experiments. In Figure 5.5(a) we also note that P does not rescale for the experimental and simulation data sets for the smallest packing fractions when $\rho < 0.785$. One possible explanation for such behavior is that the properties of the systems at these low packing fractions differ. For $\rho > 0.78$ we observe fragile force networks immediately after the first shear step and the value of $f_{NR} \geq 0.5$. This is not the case for $\rho < 0.78$, where for the small strains the sheared system develops highly anisotropic isolated force clusters that do not percolate.

Figure 5.5 (b) shows the evolution of the stress anisotropy, τ_a. In experimental data, there is an initial transient increase of τ_a from the randomly prepared nominally isotropic initial state; in the simulations we observe only few data points in this regime. For larger values of f_{NR}, the anisotropy shows a slow decrease in both experiments and simulations. After the transient regime observed in the experiments, the anisotropy shows only a modest decrease with f_{NR} for both experiments and numerical data and it remains nonzero at all times. The decreasing trend is consistent with the observation that shear jammed states initially have a very anisotropic network, which evolves towards a more isotropic network with increasing strain. The agreement between the experiments and simulations is quantitative, and even though there is a modest scatter in the numerical data, the collapse with f_{NR} is obvious.

A useful microscopic measure is the probability distribution function (PDF) of the norm of the contact forces. Much work has been devoted to characterizing and understanding this distribution [28, 42, 70] although isotropically compressed packings have been the primary focus. Here we compare PDF's between experiments and simulations; more specifically, in Figure 5.6 we consider the probability of finding a contact force with magnitude $> 0.9\langle|\mathbf{F}|\rangle$, where $\langle|\mathbf{F}|\rangle$ corresponds to the average contact force magnitude. Two features are prominent: First, for both

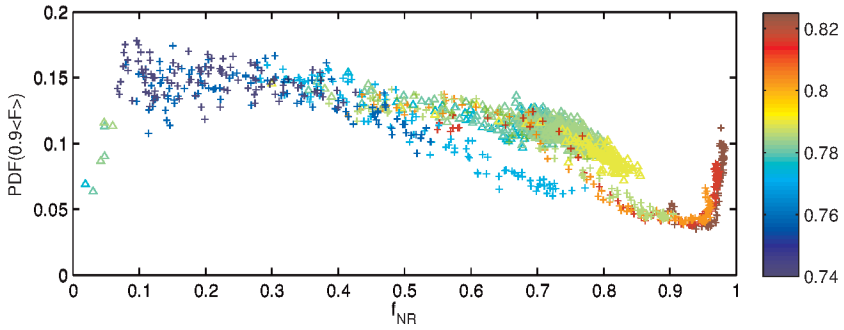

Figure 5.6 Probability distribution function of the contact force magnitude, PDF, as a function of f_{NR} for both experiments (+) and simulations ($\triangle$) with forces $> 0.9\langle|\mathbf{F}|\rangle$.

experimental and numerical data, there is a clear collapse of all data with f_{NR}. Second, experimental and numerical data are in quantitative agreement. The increase in the PDF at the largest f_{NR} may be an artifact of the experimental methods since the forces below force threshold ≈ 0.1 N cannot be detected accurately. Also, in the experimental measurement methods it is assumed that the deformations of the particles at contacts are small. This assumption ceases to be valid for large interparticle forces that occur when the value of f_{NR} is large (> 0.95) and we can expect inaccuracies in the experimental results. The collapse with f_{NR} is observed not only for the force threshold $0.9\langle|\mathbf{F}|\rangle$ but for other thresholds as well; for example, we have verified that the same features are observed for the force threshold $\approx 0.5\langle|\mathbf{F}|\rangle$ and $\approx 1.5\langle|\mathbf{F}|\rangle$.

5.4 Topological Measures for Sheared Granular Materials

The previous metrics have addressed either macro-scale or micro-scale structural properties. Neither is very sensitive to the structure of the force chain networks, such as those in Figure 5.3. These networks characterize the meso-scale properties of the system, and as such, they are sensitive to the intrinsic fluctuations induced by the shear strain.

In this section, we show simple topological measures that can provide a robust description of the force networks. Specifically, we compute the Betti numbers, β_0 and β_1. For a given force threshold, f_c, the β_0 is the number of connected components such that all forces between the particles are above f_c. For large f_c, $\beta_0 = 0$, since all particles experience forces below the threshold. As f_c goes to zero, β_0 tends to 1, because all non-rattler particles lie above the zero threshold and hence are connected. Consequently, we expect a maximum for an intermediate f_c. The second topological measure, β_1, quantifies the number of nontrivial loops defined as the sets of contact forces formed by more than three disks in mutual contact. Therefore, for a given threshold f_c, a nontrivial loop must be made up of at least four edges such that the associated forces are at least f_c.

Figure 5.7 shows the Betti numbers for the experiments (top row) and simulations (middle and bottom row). The difference between the two sets of simulations is that a random noise is applied to the contact forces for the results shown in the bottom row. Both Betti numbers in simulations with added noise (Figure 5.7 bottom row), further discussed below, match the evolution of $\beta_{0,1}$ in experiments well. This is not the case for the simulations without the noise. In fact, when we compare the results with and without the noise, we notice that the overall number of connected components, $\beta_0(f_{NR})$, is smaller by approximately a factor of 3 when the noise is not present.

The random noise that we use is chosen from a flat distribution $[0, 0.2]$ N. The amplitude 0.2 N is chosen to yield a match between the numerical and experimental data and it is consistent with the level of error in the experiments [20]. We note that after the noise is added to the contact forces, we do not require the force balance on the particles.

The non-zero mean of the added noise is motivated by the following. In the experiments, the contact force is measured as a norm of the force vector; since

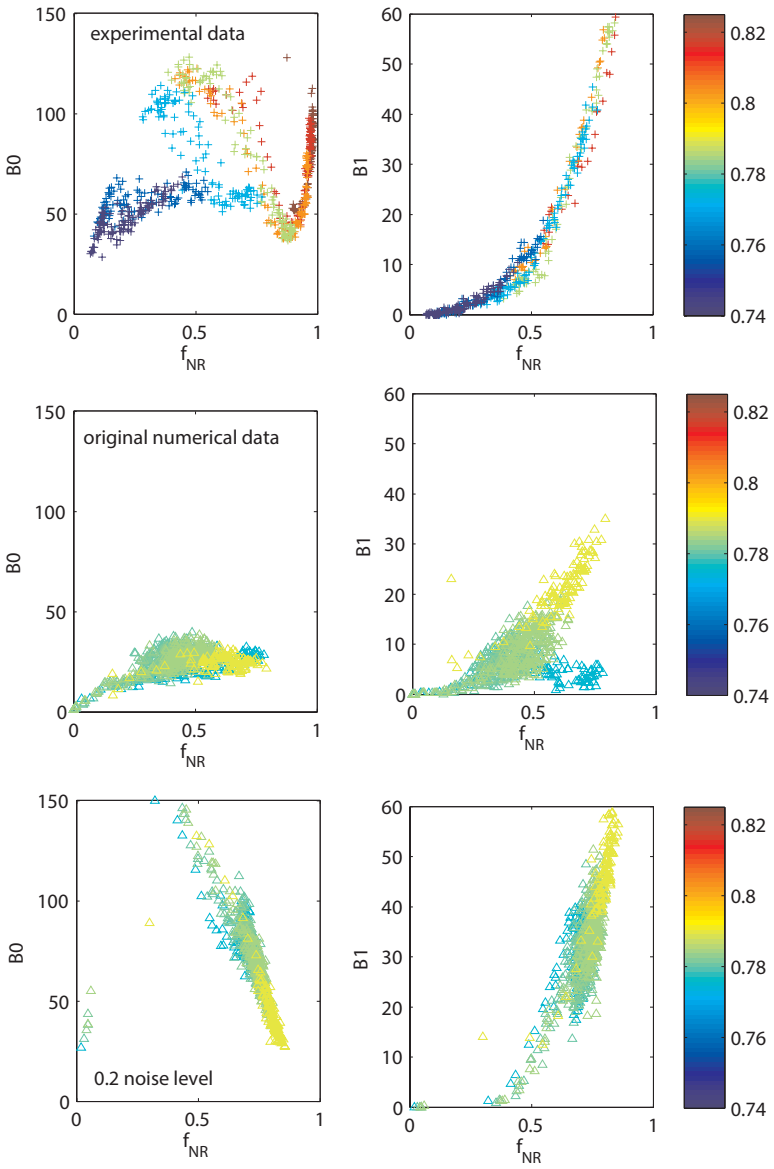

Figure 5.7 Experimental (top row) and numerical data with no noise added (middle row) and numerical data with the $0.2N$ additional noise (bottom row). The results for Betti numbers as a function of f_{NR} are shown for β_0 in the left column and for β_1 in the right column.

the norms are positive, the noise on the vector components is also positive and the resulting noise distribution has a non-zero mean. In the ongoing work [21], we consider different types of noise added to the simulation results, with different noise magnitudes, including the case where the added noise has mean approximately zero and the forces on the particles are balanced.

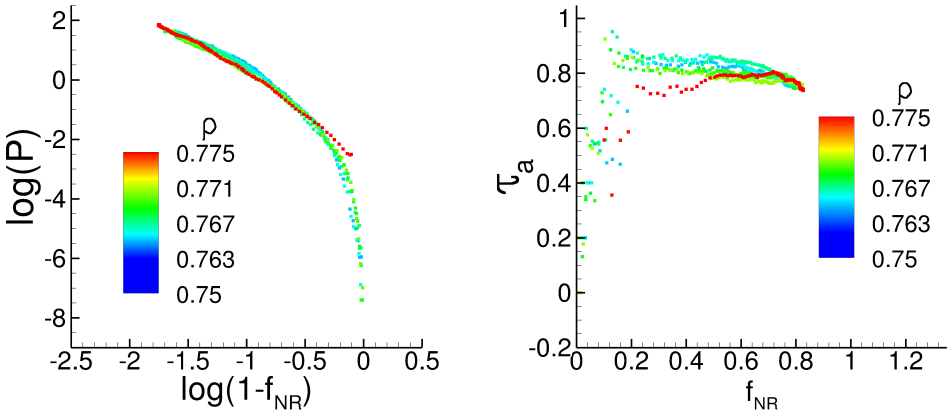

(a) (b)

Figure 5.8 (a) Pressure, P, as a function of $1 - f_{NR}$ and (b) anisotropy, τ_a, as a function of f_{NR} in sheared granular system with rolling friction included between the contacts. Plots show the results for different packing fractions, ρ.

The question then is, what causes such a dramatic quantitative difference in the experimental and numerical (without the noise) force network properties and why is the addition of noise important. The intuitive answer to this question is that there must be something in the experimental data that creates more connected components, possibly by breaking them apart. This can happen at places within a component where the forces are close to the threshold. The connections can be broken by a small decrease in one or more contact forces within a cluster, thus increasing the number of clusters. It seems that the noise added to the numerical results has the same effect (breaks clusters) and increases the number of connected components.

Finally, we discuss the influence of rolling friction on contacts in the numerical simulations. The following model [11, 73] is used for rolling resistance $\mathbf{F}_{\mathrm{i}}^{\mathrm{r}}$ between the particles $i,\ j$

$$\mathbf{F}_{\mathrm{i}}^{\mathrm{r}} = \mu_r |\mathbf{F}_{\mathrm{i,j}}^{\mathrm{n}}| \frac{\boldsymbol{\omega}_i \times \mathbf{n}}{|\boldsymbol{\omega}_i|} \tag{5.6}$$

where $\boldsymbol{\omega}_i$ is an angular velocity of the i-th particle and rolling resistance friction coefficient, denoted by μ_r, is set to the value $\mu_r = 0.02$.

Figure 5.8 shows the results for the pressure and anisotropy for the system with rolling friction at contacts. We do not notice a large influence of the rolling friction on the pressure (for comparison, see Figure 5.5). The evolution of τ_a changes dramatically, improving the agreement of this quantity with the experimental results. However, if we consider the evolution of the Betti numbers, we find a disagreement between the experiments and simulations (not shown). Therefore, the relevance of rolling friction is unclear since its inclusion does not contribute to improved agreement between the topology of the force networks in experiments and simulations; quite possibly improved models need to be developed for inclusion of this effect. We have not considered rolling friction in the results presented in this chapter.

In conclusion, in this chapter we compare the experimental and numerical results of the dynamics in sheared granular systems subject to simple shear for a range of packing fractions and shear strains near shear jamming. We probe the internal dynamics through force probability density function, and Betti numbers, β_0 and β_1. When these quantities are expressed as a function of the non-rattler fraction, f_{NR}, we obtain collapse onto master curve, capturing the dynamics over a wide range of conditions. The addition of noise with positive mean improves the match between the numerical and experimental results significantly. We propose a detail analysis of the influence of noise on the properties of force networks as a part of future work.

CHAPTER 6

ENERGY DISSIPATION IN SHEARED COHESIVE GRANULAR SYSTEMS

6.1 Introduction

In Chapter 3, we analyze how the cohesive force between the particles change the percolation and jamming properties of granular material. We find that addition of even a small amount of liquid between grains yields dramatically different results. In this chapter, the main focus will be on the analysis of the energy loss in granular materials that are either dry (with only repulsive forces between interacting particles) or wet (including attractive cohesive force). We assume that the granular system is sheared and compare the numerical simulations with the experiments performed by the collaborative group at Saarland University led by Prof. Seemann.

In this chapter, we introduce the experimental/numerical setup and shearing protocol and find the source of the energy dissipation. In numerical simulations, performed in 2D, for simplicity we use the same cohesive model as in Chapter 3 that was derived for 3D geometry. Our expectation, based on both results given in Chapter 3 and the results given here is that what really matters is inclusion of attractive forces, with their details not being crucial. In the Appendix C we propose a model for the cohesive interaction in 2D and discuss the difference from the 3D model used in simulations presented in this chapter.

6.2 Experimental Setup

In considered experiments, the granular system and the shearing protocol is set up to guarantee the spatial homogeneity of the shear rate over the whole ensemble. In particular, the following framework avoids the occurrence of the avalanches, arching and fault zones [29]. The experimental configuration consists of the set of roughly

spherical particles made from glass. The particles are confined within a shear cell described in [23, 29] and illustrated in Figure 6.1. The central part of the shear cell consists of a cylinder (inner radius $r = 5$ mm, height $H = 10$ mm) enclosed by two latex membranes which surround the glass beads. There are liquid reservoirs on the top/bottom of the shearing cell that are used to apply the pressures P_1 and P_2 to the membranes. The desired initial confining pressure $P_{\rm cf} = (P_1 + P_2)/2$ applied on the shear cell is adjusted by controlling the liquid amount in both reservoirs.

The average diameter of the glass beads is $d_{exp} = 140$ μm with a polydispersity of $\Delta d/d_{exp} \approx 0.10$. In the case of the cohesive system, the glass beads are prepared with a water content of $W = (0.025 \pm 0.05)V_g$ with V_g being the total granular volume. The surface tension of water is $\gamma \approx 70\,\mathrm{mN/m}$ [80] and the contact angle of water on the glass beads is $\theta = (7 \pm 2)^\circ$.

The granulates are sheared at constant cell volume by simultaneously adding and removing the liquid content from the reservoirs at constant rate (keeping their total volume constant in time), with the tensions of the latex membranes ensuring a roughly parabolic shear profile. Figure 6.1(a) shows the scheme of the experimental setup. The shear displacement, denoted by Δh, that results from changing the liquid volume in reservoirs, denoted by ΔV, is measured in the center of the cylindrical cell, and the shear angle, α, and the shear rate, γ, are calculated from Δh as $\alpha = \Delta h/r$ and $\gamma = \alpha/t$. The applied shear rate is $\gamma \approx 3 \times 10^{-3}\,\mathrm{s}^{-1}$.

Figure 6.1(b) shows the pressures P_1 and P_2 in the top panel for one shear cycle. The corresponding differential pressure, $\Delta P = P_2 - P_1$, and the confining pressure $P_{\rm cf} = (P_1 + P_2)/2$ are shown in the bottom panel. Note that $P_{\rm cf}$ varies during the shear. We restrict the analysis of the shear behavior to $|\Delta V| < 33$ μl, where $P_{\rm cf}$ can be safely considered as constant, as in the simulations discussed below.

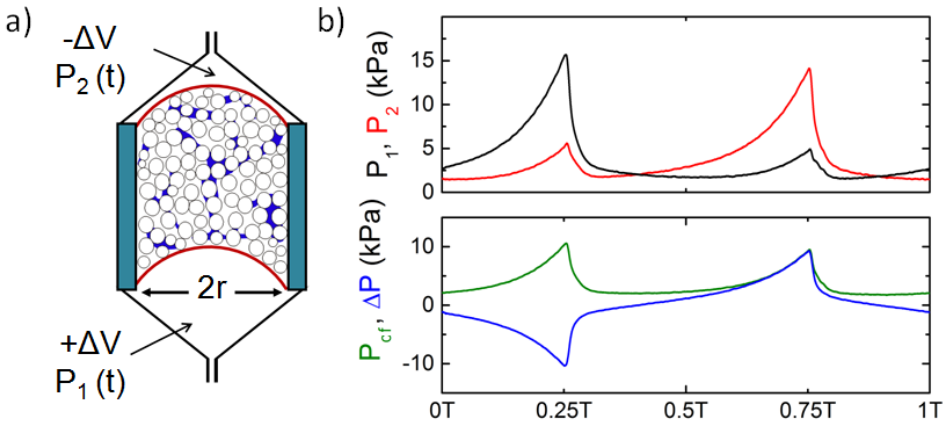

Figure 6.1 (a) Schematic plot of the experimental setup from [32] and (b) evolution of the confining pressure, P_{cf}, pressures on the top and bottom walls, P_1, P_2, and the differential pressure, ΔP, during a shear cycle.

6.3 Numerical Simulations of the Sheared Granular Systems

For computational simplicity we perform simulations in two dimensional (2D) setup with circular particles. The domain is initially rectangular and of the size $[47, 17]$, expressed in terms of the average particle diameter, d_{ave}. The walls of the box are composed of monodisperse particles. System particles are polydisperse with the diameters varying by $\pm 20\%$ from the average particle diameter d_{ave}.

The force model used in the simulations assumes that the particles are soft inelastic disks that interact via normal and tangential force. The scales in our model are the average particle diameter, $d_{ave} = 0.4$ cm, average particle mass, $m = 0.263$ g, and binary collision time, $\tau_c = \pi\sqrt{d_{ave}/(2gk_n)}$, with k_n being a spring constant as described in detail in Appendix A. For the interparticle friction, we use two different friction coefficients $\mu = 0.23,\ 0.29$ for the wet and dry systems, respectively. The aforementioned values of μ are estimated from the experimental measurements [62]. The time step used in simulations corresponds to $\Delta t = 0.02$ and the non-dimensional value of the linear spring is set to $k_n' = 4 \times 10^3$. The coefficient of restitution is set to

$e = 0.5$ and we assume a static friction model (see Appendix A) with the tangential spring constant $k'_t = 0.8\ k'_n$.

We use a 3D cohesive force model based on the attractive force between two spherical particles due to the presence of a liquid bridge. The amount of liquid is set to $\approx 4\%$ of the average particle area for every cohesive interaction. Cohesive bridges form after particles get in contact and break when bridge length exceeds the maximum one, s_c, that depends on the (constant) amount of the liquid and wettability [29, 79]. The contact angle, $\theta = 12^\circ$, is similar to the value in the experiments. For a detailed description of the cohesive force interaction, see Appendix B.

At the beginning of each simulation, we assign random velocity to each system particle. Then, the top and the bottom walls are moved inward by applying an initial pressure, P_{init}, expressed in terms of force per length, until equilibrium is reached. At this point, we start shearing the system by prescribing parabolic wall shape evolving in time. Similarly as in the experiments, α denotes the angle between the line connecting the endpoints of the left and right walls and the position of the center of the top wall. The maximum value of the shearing angle is $\alpha = 4^\circ$ and the motion of the top/bottom wall is periodic in time with period T'. At the beginning of a cycle, the system is sheared from the flat state ($\alpha = 0$) in the positive vertical direction. After reaching $\alpha = 4^\circ$, the shear continues in the opposite (negative) direction, until α reaches the value -4° and the direction of the shear is reversed. The cycle is complete when the system reaches $\alpha = 0$.

The motion of the top/bottom wall during the time $t \in (-T'/4, 3/4T']$, in dimensionless units, is given by

$$y(t) = \left(1 - \frac{2x^2}{47}\right) tv + C \qquad t \in (-T', T'] \tag{6.1}$$

$$y(t) = \left(1 - \frac{2x^2}{47}\right) (T' - t)v + C \qquad t \in (T', 3T'] \tag{6.2}$$

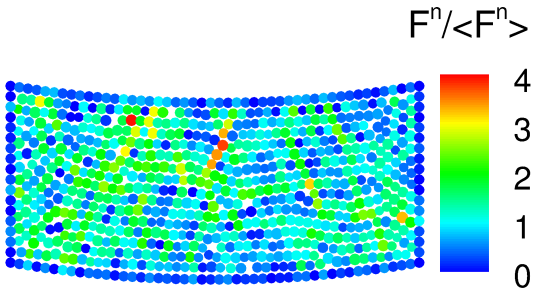

Figure 6.2 Example of the simulated system during shear. Particles are color coded according to the total normal force, normalized by the average normal force, $\langle \mathrm{F^n} \rangle$.

where x is the position of the wall particle with respect to the horizontal axis (assuming that $x = 0$ for the center of the top/bottom wall) and v has a cosine velocity profile. The average of $|v|$ over the shear cycle, denoted by v_s, is $v_s = \gamma' L = 10^{-4}$, where $\gamma' \approx 2 \times 10^{-6}$ and $L = 47$ are the rescaled values of shear rate and length of the system, respectively. The constant C assumes the appropriate value for the top and bottom wall particles. Figure 6.2 shows the granular system during the downward shear.

Due to the rearrangements of the particles during shear, the pressure inside of the system drops; to keep the pressure at the desired value, we let the top wall slide up and down until the system finds its new equilibrium. Then, we fix the end points of both walls and continue shearing until the pressure inside of the system, averaged over a shear cycle, reaches a constant value. In the discussion of energy loss that follows, we will use the average value of the pressure on the top and bottom wall exerted by the system particles, $P'_{cf} = 0.5(P'_1 + P'_2)$. Pressure P'_{cf} is a dimensionless confining pressure and P'_1, P'_2 correspond to the pressures on the top/bottom walls.

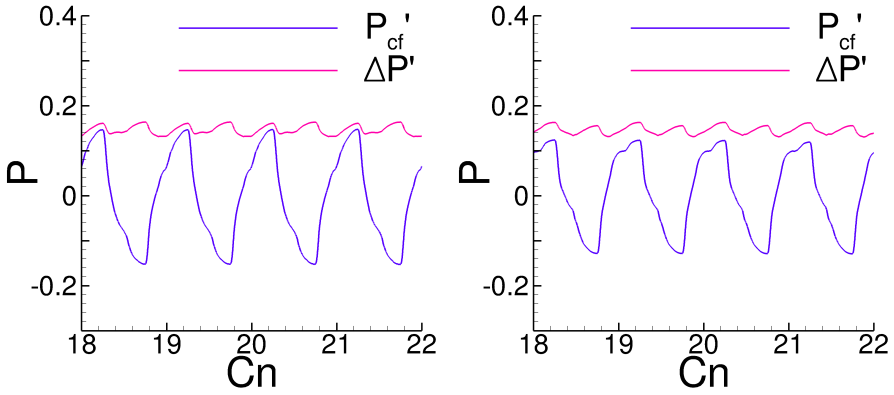

Figure 6.3 Evolution of the average, P'_{cf}, and differential pressure, $\Delta P'$, in simulations over the cycles (denoted by Cn) for (a) dry, and (b) wet system for the initial pressure $P_{init} \approx 0.4$.

6.4 Comparison of the Numerical and Experimental Results

In the Figure 6.3 (a), (b), we compare the average pressure on the top and bottom wall, P'_{cf}, and differential pressure, $\Delta P' = (P'_1 - P'_2)/2$, for the wet and dry systems in numerical simulations. The two pressures, P'_{cf} and $\Delta P'$, reach similar value at the turning point, when the shear is reversed. We notice that the results are similar to those in the experiments (Figure 6.1 (b) bottom panel); the local minima and maxima in $\Delta P'$ correspond to the peaks in P'_{cf}. Unlike experiments, the two curves do not touch.

Figure 6.4 (a), (b) shows the evolution of P'_1, P'_2 over several cycles for the wet and dry systems. The overall behavior of P'_1, P'_2 resembles P_1, P_2 in Figure 6.1 (b). Specifically, the pressures on the top and bottom walls show alternating local maxima and the second smaller peak in the pressures P'_1, P'_2 in the experiments corresponds to a small hump in P'_1. This smaller local maximum during a cycle occurs roughly during the time when P'_2 assumes its maximum. Similarly, the hump in P'_2 corresponds to the peak in P'_1.

Figure 6.5 shows the hysteresis loop during a shear cycle. In both experiments and simulations, we notice a difference between the wet and dry systems. The

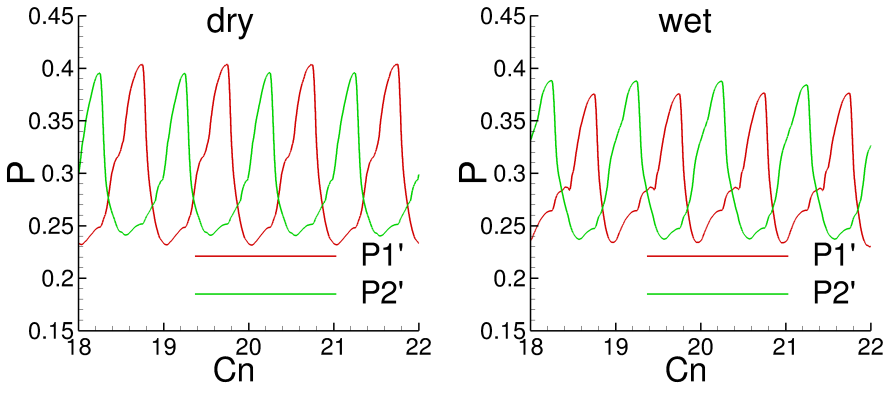

(a) (b)

Figure 6.4 Pressure on the top wall, P_1', and bottom wall, P_2', in simulations over the shear cycles (denoted by Cn) for (a) dry and (b) wet system for initial pressure $P_{init} \approx 0.4$.

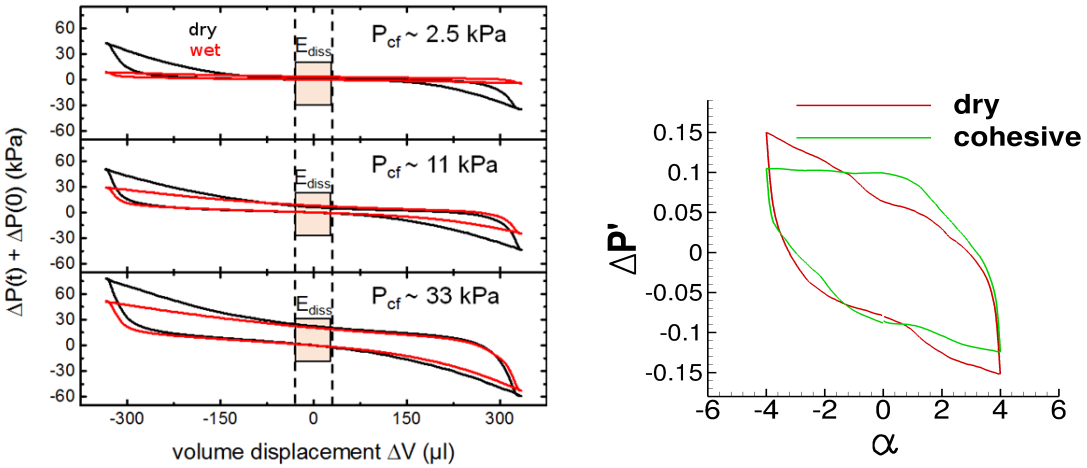

(a) (b)

Figure 6.5 (a) Hysteresis loop during one shear cycle as a function of the liquid volume change, ΔV, for different pressures, P_{cf}. $E_{\text{diss}} = \int pdV$ represents the energy that is dissipated in the system over a certain shear volume (experimental results). (b) Hysteresis loop in the numerical simulations with $\Delta P'$ as a function of α.

magnitudes of the pressures on one of the turning points, where the shear changes its direction, are much larger for the dry system. We also notice that in the simulations (for this specific P_{init}), the average opening of the hysteresis curve is larger for the wet system (in experiments, only the two smallest shown P_{cf}'s have the opening larger for

the wet system), which indicates larger energy dissipation when cohesion is present. We discuss the energy loss in detail in the next section.

6.4.1 Energy Balance and Dissipation

In this section, we analyze the energy dissipation in dry and wet granular systems. The energy dissipated during the shear is first discussed for the experiments and then we continue by finding the energies in the numerical simulations and writing the equation for the energy balance.

In the experiments, we estimate the total dissipated energy from the hysteresis loops. The enclosed areas in Figure 6.5(a) represent the energy that is dissipated in the system over a certain shear volume, $E_{\text{diss}} = \int pdV$ since the hysteresis loops are a result of the granular stiffness which opposes the applied shear deformation.

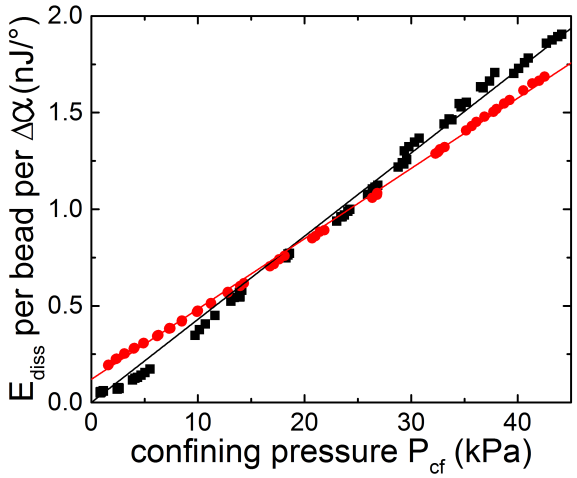

Figure 6.6 Dissipated energy, E_{diss}, in experiments normalized by the number of glass beads and the change in the sharing angle, $\Delta\alpha$ (corresponding to the change in α over which we integrate the volume of the hysteresis curve), as a function of P_{cf} for dry (closed squares) and wet (closed circles) granular systems.

Figure 6.6 shows the dissipated energy per bead and shear angle, $E_{\text{diss}}/\Delta\alpha$, as a function of P_{cf} for dry and wet systems. $\Delta\alpha$ corresponds to the change in α over which we integrate the volume of the hysteresis curve to find E_{diss}.

The dissipated energy increases faster with P_{cf} for the dry granulates than for the wet ones. However, in both cases, we can fit a straight line to the data with slope $\approx 0.043\mathrm{nJ}/(^\circ)$ kPa and $\approx 0.036\mathrm{nJ}/(^\circ)$ kPa, respectively. The linear fit for the dry systems has an intercept with the vertical axis at roughly zero value, and the intercept is $\approx 0.12\,\mathrm{nJ}/(^\circ)$ for the wet case. In other words, for a nearly zero confining pressure, P_{cf}, we observe a nearly zero energy dissipation in dry systems, while cohesion and possibly the breakup of the bridges causes a significant energy loss during a shear cycle.

To shed light on the origin of the observed energy dissipation, we first discuss the impact of capillary forces. Driven by the minimization of interfacial energies, liquid bridges form at mutual contacts of neighboring beads. For the considered liquid content of $W = 0.025 \pm 0.005$ and the chosen slow shear rate, the liquid bridges are assumed to have a constant Laplace pressure [60, 61]. The volume of a single capillary bridge is estimated to be $V = 0.058\,R^3$, corresponding to the largest possible value, that is determined from the geometrical properties of the spheres in the shearing granular cell [61].

The energy dissipation due to the number of the capillary bridges that break in experiments is explored by X-Ray tomography. From the images recorded during a full shear cycle, the breaking capillary bridges are determined in each time interval by numerical image analysis; the result for the number of ruptured bridges per bead, N_{rupt}, is shown in Figure 6.7 for the confining pressure $P_{\mathrm{cf}} = 6$ kPa. We note that for technical reasons (such as insufficient resolution of the tomography), the results in Figure 6.7 were obtained by using larger particles, with the average diameter $d'_{exp} = 282\ \mu$m. N_{rupt} varies around 0.25, and the maxima are close to the turning points of the shear movement, where the gradient of the velocity reaches its maximum. The regime between the local maxima is approximated linearly to obtain the number of breaking bridges per shear angle $\Delta\alpha$. The number of the rupture events per shear

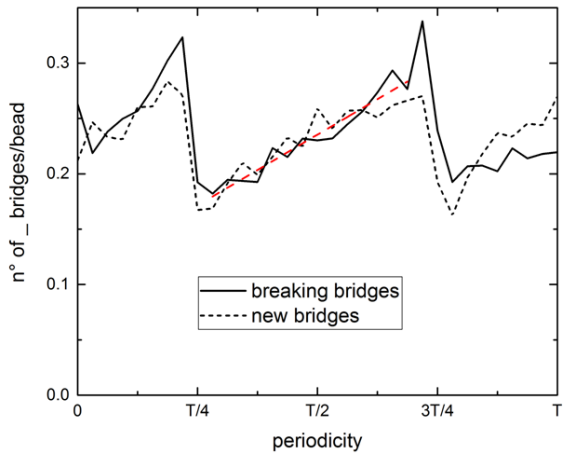

Figure 6.7 Broken bridges during the shearing cycle in experiments at a confining pressure $P_{\mathrm{cf}} = 6$ kPa.

angle is $N_{\mathrm{rupt,tot}} = \int N_{\mathrm{rupt}}(\alpha) d\alpha$ and the total dissipated energy equals $\Delta W_{\mathrm{d,tot}} = \Delta W_{\mathrm{diss}} \cdot N_{\mathrm{rupt,tot}}$, where $\Delta W_{\mathrm{diss}} = \int_0^{\bar{s}_c} \mathrm{F_c}(\bar{s}) \mathrm{d}\bar{s}$ is the energy stored in a capillary bridge at the critical separating distance, s_c, with $\mathrm{F_c}(\bar{\mathrm{s}})$ being the magnitude of cohesive force at distance $\bar{\mathrm{s}}$ (computed as shown in Appendix B).

For a quantitative comparison of the results obtained for $\Delta\alpha$ for the shear cell with beads of $d_{exp} = 140$ μm with the data for the large beads with $d'_{exp} = 282$ μm, we have to scale $\Delta W_{\mathrm{d,tot}}$ with the respective bead radius. For a constant shear angle the number of breaking bridges per bead is independent on the bead size. The dissipated energy can be scaled linearly with the number of beads in the granular volume assuming a constant packing density of ≈ 0.59 and the dissipated energy for a breaking bridge, ΔW_{diss}. The total dissipated energy due to breaking of the capillary bridges can be calculated as $\Delta W_{\mathrm{d,tot}} = (0.13 \pm 0.03)$ nJ/(°) for wet glass beads, with the error accounting for the uncertainty in the contact angle. Note that $\Delta W_{\mathrm{d,tot}}$ is consistent with the intercept of the linear fit to the $E_{\mathrm{diss}}/\Delta\phi$ vs. P_{cf} of $0.12 \pm 0.003\, nJ/(^\circ)$ shown in Fig. 6.6, i.e. for vanishing confining pressure.

To compare the numerical results with the experiments, we first find the energies in the system during shear, then we find the equation of the energy balance and

the corresponding dissipated energy. Note that the dissipated energy extracted in simulations is significantly more accurate than using hysteresis as the experiments do. We start by computing the energy that is added to the system by moving the top and bottom wall. To do this, we integrate the total force that acts on the walls

$$\begin{aligned} E &= \int_{\delta S} \mathbf{F} \mathrm{d}\mathbf{s} \\ &= \int \mathbf{F}\mathbf{n}_{\mathrm{s}} \mathrm{ds} \end{aligned} \tag{6.3}$$

where $\mathbf{n}_{\mathrm{s}}$ is the unit vector normal to the boundary. The total energy added to the system by the moving walls is

$$\begin{aligned} E_w &= \sum_j \mathbf{F}_{\mathrm{j}}\mathbf{n}_{\mathrm{j}} \mathrm{ds} \\ &= \sum_j \frac{(-2ax_j, 1)}{\sqrt{1+4a^2x_j^2}} \mathbf{F}_{\mathrm{j}} \mathrm{ds} \end{aligned} \tag{6.4}$$

where the vector multiplying the force terms in Equation 6.4 represents the normal to the parabolic top/bottom boundary. To find the total energy stored in a capillary bridge between particles i, j, we need to integrate the cohesive force (see Appendix B for details) over the separating distance $\bar{s}$ (smaller than the critical separating distance, s_c). We denote the energy stored in a capillary bridge by E_b and integrate

$$\begin{aligned} E_b &= \int_0^{\bar{s}} |\mathbf{F}_{\mathrm{b}}| \mathrm{ds} \qquad (6.5) \\ &= \int_0^{\bar{s}} \frac{2\pi\bar{r}\cos\theta}{1+1.05s\sqrt{\bar{r}/V}+2.5s^2\bar{r}/V} \mathrm{ds} \\ &= 4\pi\cos(\theta)\sqrt{\frac{\bar{r}V}{8.8795}}\left[\arctan\left\{5\bar{s}\sqrt{\frac{\bar{r}}{V8.8795}}+\frac{1.05}{\sqrt{8.8795}}\right\}\right. \\ &- \left.\arctan\left\{\frac{1.05}{\sqrt{8.8795}}\right\}\right] \end{aligned}$$

The total energy stored in all capillary bridges is

$$E_b = \sum_{i,j;i\neq j} E_{b_{ij}} \tag{6.6}$$

for all pairs of particles i, j that interact via the cohesive force.

The energy that is dissipated during the rupture of capillary bridges is equal to the cohesive energy, E_{bb}, at the critical distance of each two interacting particles i, j

$$\begin{aligned} E_{bb} &= \sum_{i,j} \int_0^{s_c} |\mathbf{F}_\mathrm{b}| \mathrm{ds} \\ &= \sum_{i,j} \int_0^{s_c} \frac{2\pi\bar{r}\cos\theta}{1 + 1.05s\sqrt{\bar{r}/V} + 2.5s^2\bar{r}/V} \mathrm{ds} \end{aligned} \tag{6.7}$$

Note, that this energy loss corresponds to ΔW_{diss} in experiments.

During the evolution of the system, all the energy has to be accounted for and therefore we can write the energy balance equation. The energy input comes from the moving walls and therefore we assume that E_w is positive. First, consider the regime where there is no breakup of capillary bridges. In this case, the energy balance gives

$$E_w(t) = \Delta E_{el}(t) + \Delta E_k(t) + \Delta E_b(t) + E_l(t) \tag{6.8}$$

where

- $E_w(t)$ = energy which entered the system between the times $t - \delta t$ and t; call this time period a "previous" time step. We need to use the previous time step since the energy needed to enter the system can be used during the current time step (time period from t to $t + \delta t$).
- $\Delta E_{el}(t) = E_{el}(t + \delta t) - E_{el}(t)$ is the change of elastic energy of the particles.
- $\Delta E_k(t) = E_k(t+\delta t) - E_k(t)$ is the change of total kinetic energy of the particles.
- $\Delta E_b(t) = E_b(t + \delta t) - E_b(t)$ is the change of total energy stored in the capillary bridges.
- $E_l(t)$ is the energy dissipated due to inelasticity and friction. This energy is computed using the above equation.

Energy due to the breakup of the bridges introduces complications. As a bridge breaks up, all the energy that was accumulated in this bridge during the previous time steps is released, or more precisely, transformed to either elastic or kinetic degrees of freedom (it is not lost). So a correction of the above equation is needed to keep energy balance satisfied during any given time step. Let us call by $E_{bb}(t)$ the energy released by breakup of capillary bridges between t and $t + \delta t$ (this energy should be positive). Then, corrected conservation of energy is

$$E_w(t) = \Delta E_{el}(t) + \Delta E_k(t) + \Delta E_b(t) + E_l(t) + E_{bb}(t) \tag{6.9}$$

The reason for the positive sign in front of E_{bb} in Equation 6.9 is easily seen from the following special case study.

Let us have a system with only two particles, p_1 and p_2, that are not in contact with the walls or with each other. Suppose that there is a cohesive bridge between p_1 and p_2 and that at a time step $t + \delta t$, the cohesive bridge between particles breaks. Since the particles do not have any contacts, $E_w = E_{el} = 0$ at both time steps t and $t + \delta t$. Also note that at the time step $t + \delta t$ the bridge breaks and the kinetic energy does not change since the particles p_1 and p_2 were not in contact. Therefore, $\Delta E_k(t) = 0$ in the energy balance Equation 6.9. All the energy from the cohesive bridge is released and so $E_b(t + \delta t) = 0$. The energy of $E_b(t)$ at the time step t was very close to that for a bridge at separating distance s_c. We have $E_b(t) \sim E_{bb}$. Finally, $\delta E_b(t) \sim -E_{bb}(t)$ and from the Equation 6.9

$$\begin{aligned} E_w(t) &= \Delta E_{el}(t) + \Delta E_k(t) + \Delta E_b(t) + E_l(t) + E_{bb}(t) \\ 0 &= 0 + 0 - E_{bb}(t) + E_l(t) + E_{bb}(t) \\ 0 &= E_l(t) \end{aligned} \tag{6.10}$$

Note, that $E_l(t)$ is the energy in the system dissipated due to effects other than cohesion. Therefore, $E_l(t) = 0$ in Equation 6.10, as it should.

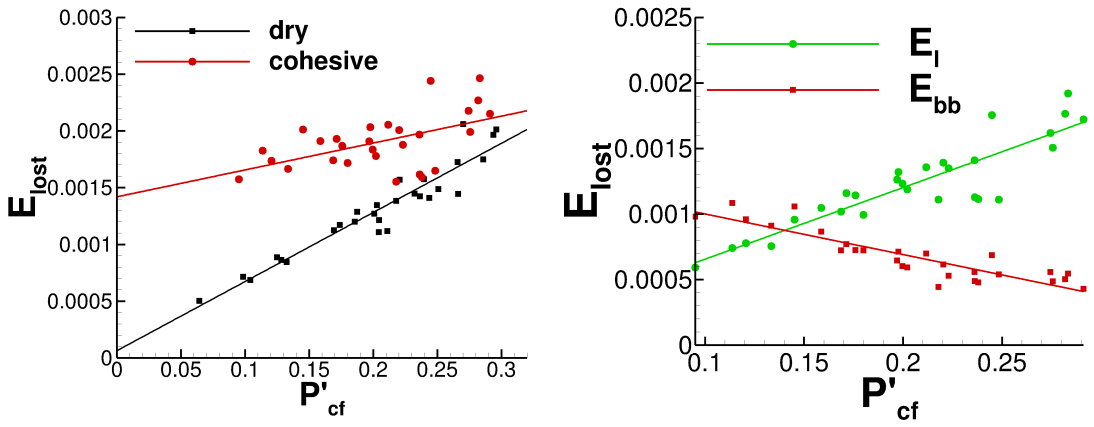

(a) (b)

Figure 6.8 Influence of the cohesion on the dissipated energy: (a) comparison of the dissipated energy, E_l for the wet and dry system for different P'_{cf}, (b) comparison of the energy dissipated due to a breakup of the cohesive bridges, E_{bb}, and the energy lost from other dissipative effects, $E_l - E_{bb}$.

We continue the discussion by analyzing the dissipated energy in simulations found by using the force balance Equation 6.9. Figure 6.8(a) shows a comparison of the dissipated energies in the wet and dry systems. The linear fit though the data shows different trends with different slopes for the dry and wet systems; the value is lower for the wet and larger for the dry granulates. Similarly as in the experiments, the linear fit through the data for the dry systems crosses the vertical axis at approximately zero value for the zero confining pressure, P'_{cf}, while for the wet systems, the energy loss is non-zero as $P'_{cf} \to 0$. The only significant difference from the experiments is the absence of the crossover of the two lines for the considered P'_{cf}; the maximum value of P'_{cf} corresponds here to the largest possible packing fraction, $\rho = 0.91$.

Figure 6.8(b) shows the energy dissipated due to breaking of the bridges, E_{bb}, and the energy dissipated from other effects, $E_l - E_{bb}$. We observe a crossover around the average pressure $P'_{cf} = 0.25$. Above $P'_{cf} = 0.25$ the dissipative non-cohesive effects

dominate the lost energy, while below $P'_{cf} = 0.25$ the most of the dissipated energy is due to bridge breakups.

The question is why the energy dissipated due to the breaking bridges is a decreasing function of the confining pressure, P'_{cf}. One possible explanation is that the particles move less relative to each other under the larger pressure and so there are less particles that would collide and then separate by a distance larger than s_c. Therefore, in the next section, we analyze the non-affine motion of the particles during the shear.

6.4.2 Non-affine Motion

During shear, particles move in the direction of moving walls and also relative to each other. The relative motion of the particles, also referred to as the non-affine motion, is the reason for breaking of the cohesive bridges and subsequently the loss of energy tied to the cohesive effects, E_{bb}. We investigate the non-affine motion of the particles as a function of P'_{cf}, friction and inelasticity to find the dependence of our results on different parameters. To compute the non-affine motion, we follow the approach described in [34]. First, for every particle p, we find the affine deformation matrix, $A(t)$, at time t, with the property

$$A(t)\mathbf{r}_0(t) = \mathbf{r}_0(t + \delta t) \tag{6.11}$$

where $\mathbf{r}_0(t)$ is the position of the particle p at time t. The non-affine motion is defined as the minimum of the mean squared displacement, D^2

$$D^2 = \sum_{n=1}^{m} ||\mathbf{r}_n(t) - \mathbf{r}_0(t) - [A(t)\mathbf{r}_n(t) - A(t)\mathbf{r}_0(t)]||^2 \tag{6.12}$$

where m is the number of particles within the distance of $2.5d_{ave}$ from the particle p and $\mathbf{r}_n(t)$ is the position of the n-th particle within this distance.

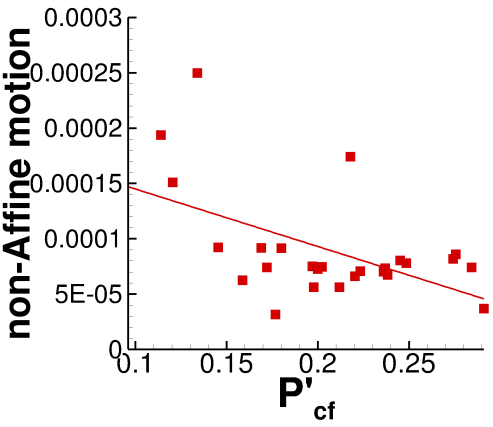

Figure 6.9 Non-affine motion as a function of confining pressure, P'_{cf}, averaged over 12 cycles.

Figure 6.9 shows the non-affine motion as a function of P'_{cf}. We notice that for the larger pressure, particles move less relative to each other. Since larger applied pressure causes particles to move less relative to each other, we expect that the energy loss due to cohesion decreases as the pressure increases.

To complete the analysis of the non-affine motion, we find the effect of the friction and inelasticity of the particles on the total dissipated energy and E_{bb}. We

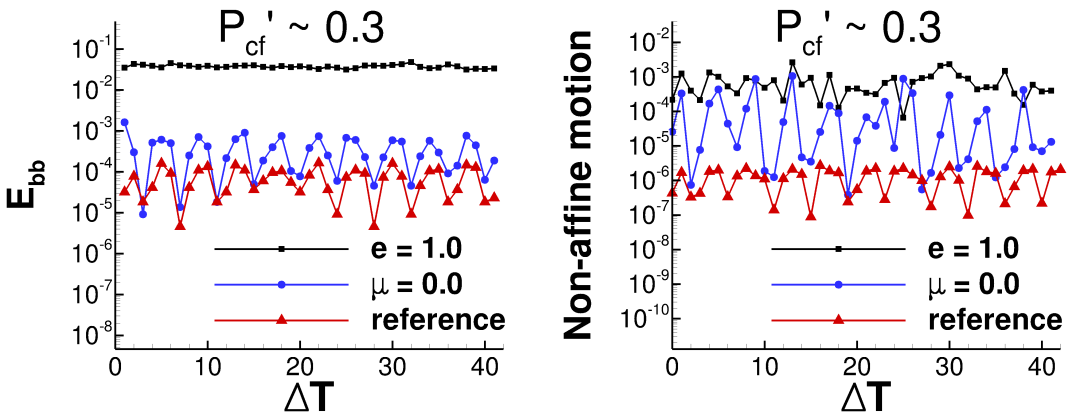

Figure 6.10 (a) Energy dissipated due to breaking of the bridges and (b) non-affine motion as a function of time intervals, ΔT, for the elastic and frictionless particles.

compare the results obtained with the parameters as considered so far (reference simulations) to the system with frictionless and elastic particles. Figure 6.10 shows

E_{bb} and non-affine motion as a function of time intervals, ΔT, that corresponds to $\approx 7 \times 10^4$ time steps. We again observe that the smaller non-affine motion for any of the systems considered corresponds to the smaller E_{bb} while the larger value of non-affine motion corresponds to larger values of E_{bb}.

6.5 Conclusions

In this chapter we discuss the origin of energy dissipation in sheared wet and dry granulates. For increasing confining pressures, the energy dissipation of various granular samples increases linearly as a result of increasing friction between the particles. For small applied pressures in the experiments (and all confining pressure in the simulations), wet granulates are stiffer than dry ones due to the internal capillary cohesion by virtue of capillary forces and in particular due to the energy dissipated by breaking capillary bridges. The energy that is dissipated by breaking bridges found in the tomography experiment is in good agreement with the energy dissipation for vanishing confining pressures. Above a certain confining pressure the energy dissipation in experiments for dry and wet granulates is dominated by the friction between the individual particles. We find that the number of broken bridges decreases with the increasing confining pressure due to restricted non-affine motion during the shear.

CHAPTER 7

BIAXIAL SHEAR OF THE THREE DIMENSIONAL SYSTEM OF SPHERICAL PARTICLES

In this chapter, we present the numerical simulations of a three dimensional (3D) granular system composed of spherical particles and subject to a biaxial shear. In the case when a 3D granular system is dense (jammed), the particles have in average at least 4 contacts (for frictional particles, we need at least 4 contacts per particle to have a stable packing [68]). Due to deformation of the particles, the force on an individual contact may be influenced by the forces on all other contacts of the particle. Therefore, the classical force model in the dense $3D$ granular system might not be accurate [12]. Here, we present the numerical simulations for two different force models and compare the results. The first force model is based on the classical approach when the force on the contact is computed as outlined in Appendix A; to find the force we take into account only the collision with another particle at the contact itself. In the second force model [12], described in the next section, the contact force is influenced by all interactions (collisions) of a particle with other particles.

7.1 Force Model Based on Multiple Contacts

The force model that takes into account mutual interaction of all contacts of a spherical particle is given in [12]. It is shown [12] that such "multiple contact" (MC) force model matches the experiments better for the dense granular packings with long lasting contacts in comparison with the traditional "single contact" (SC) force model approach.

The force model in [12] is based on the modeling of the mutual influence of the contacts of a particle. For each contact, c, we know the deformation of the particle, δ_c, at c. We compute the deformations, $\delta_{k\to c}$, of the particle on the contact c due to

other contacts k of the particle. The deformation $\delta_{k\to c}$ is given by [12]

$$\delta_{k\to c} = -1.19\frac{(1+\nu)\mathbf{F}_{\mathrm{k}}}{2\pi E d_{kc}}\left\{(\mathbf{n}_k.\mathbf{u}_{kc})(\mathbf{n}_c.\mathbf{u}_{kc}) + (3-4\nu)\mathbf{n}_k.\mathbf{n}_c - (1-2\nu)\frac{(\mathbf{n}_k+\mathbf{u}_{kc}).\mathbf{n}_c}{1+\mathbf{n}_k.\mathbf{u}_{kc}}\right\} \tag{7.1}$$

where the force $\mathbf{F}_{\mathrm{k}}$ is the force at contact k, ν and E are the Poisson ratio and Young's modulus, respectively. $\mathbf{n}_k$, $\mathbf{n}_c$ are the vector normals at the corresponding contacts $k,\ c$, pointing towards the center of the particle i, $\mathbf{u}_{kc}$ is the unit vector pointing from the contact k to the contact c and d_{kc} is the distance between the contacts $k,\ c$.

The total deformation of the particle is then $\delta = \delta_c + \sum_k \delta_{k\to c}$ and we find the total force on the particle at c

$$|\mathbf{F}_c| \propto \delta_c + \sum_k \delta_{k\to c} \tag{7.2}$$

7.2 Force Networks and Pressure Comparison of the Single and Multiple Contacts Force Model Simulations

According to [12], using the MC force model in the simulations of granular spheres should lead to an improvement of the match between the results for the numerical simulations and experiments for dense packings. We compare the MC and SC force models for the system of spherical particles under the biaxial shear. To quantify the difference between MC and SC we compare the pressure exerted by the particles on the top and bottom walls of a box (that encloses the granular system) during shear.

The system parameters and geometry is set up to mimic the experiments performed by the Duke experimental group, where the setup is similar to the one described in [12]. The particles are soft elastic spheres, with the Young's modulus $E = 23$ kPa and Poisson ratio $\sigma = 0.5$. The friction coefficient is set to the value $\mu = 0.03$ and the particles are assumed to be immersed in a liquid, so that the effective gravity is $0.01\mathbf{g}$ where $|\mathbf{g}|$ is the gravitational constant.

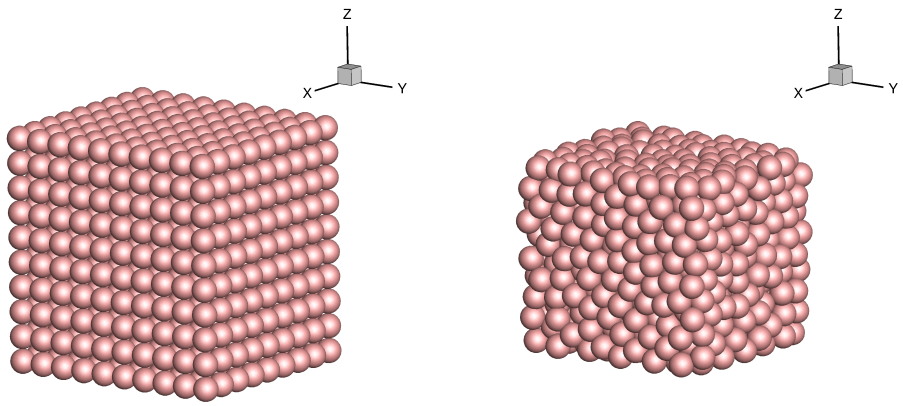

(a) (b)

Figure 7.1 3D granular system of spheres (a) before shear (initial condition) and (b) during shear. The plot shows the snapshots of the granular system with the single contact force model.

The system dimensions, expressed in d_{ave} (the average particle diameter) are $11 \times 12 \times 12$ and there are 882 particles confined within the box. Box walls are also composed of the spherical particles of diameter d_{ave} and with the same properties as the system particles. The wall particles do not interact with each other. The diameters of the system particles are chosen from Gaussian distribution with the mean particle size $d_{ave} = 17.35$ mm and the variance of 1 mm, as in the experiments.

The initial condition for the simulations is set up as follows. First, the particles are placed on the cubic grid and we assign to each of them a random initial velocity. Then, the box is slowly compressed up to a packing fraction $\rho = 0.64$. After reaching the desired packing fraction, we continue with a bi-axial shear as follows.

The shear is periodic and consists of compressing the box by moving the top wall down while the four side walls are expanded equally by 2.5% of the system width. The volume of the box is kept constant. After reaching the maximum shearing amplitude, the box is sheared in a reverse fashion back to the initial shape. Figure 7.1(a) shows the granular system at the initial configuration and Figure 7.1(b) shows the system during the shear (wall particles are not shown). Due to the high packing fraction, ρ, we

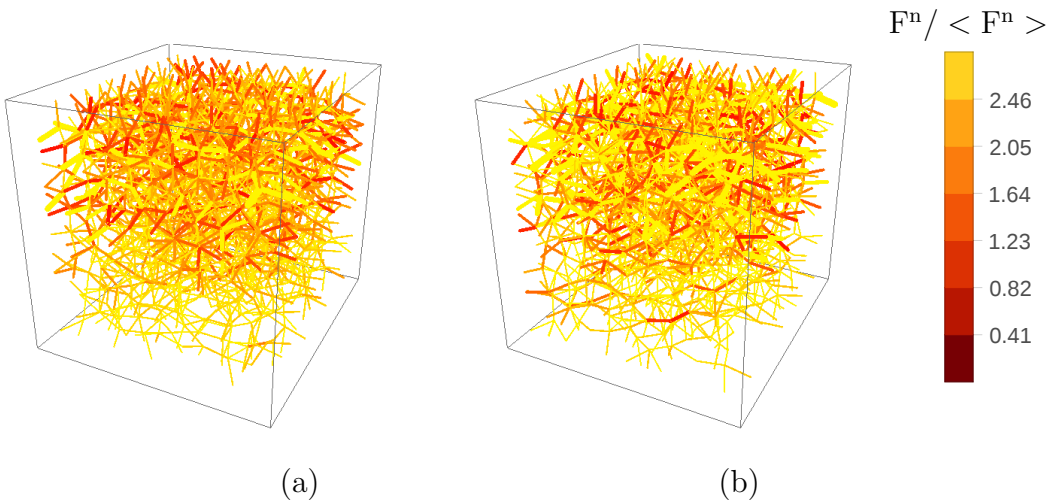

(a) (b)

Figure 7.2 Force network for 3D granular system with (a) single (SC) and (b) multiple contacts (MC) force model. The forces are color-coded.

can expect that the particles have long lasting contacts during the shear. According to [12], we can expect that the MC force model is appropriate in such a case.

Figure 7.2 (a), (b) shows the network of forces between the colliding spheres of the sheared system for the SC and MC force models. The force networks shown in Figure 7.2 (a), (b) correspond to the same time step in the simulations. During this time step, the top wall is moving down while the bottom wall is fixed and so we can observe a more dense force network close to the top wall. The contact forces are color coded according to the total normal force between the particles, normalized by the average force, $\langle F^n \rangle$. The widths of the lines also represent the force contact magnitudes: the wider the line representing the contact force is, the larger is the force magnitude. We notice a difference between the two networks - for the system corresponding to the SC model, the force network is more concentrated towards the top wall and less dense at the bottom wall, while the force network corresponding to the MC force model is more spread out over the whole domain. These observations (that there is a difference between MC and SC), however, need to be quantified and so we continue to study the pressure on the top and bottom walls during the shear. Figure 7.3 shows the pressure, P, on the top and bottom walls

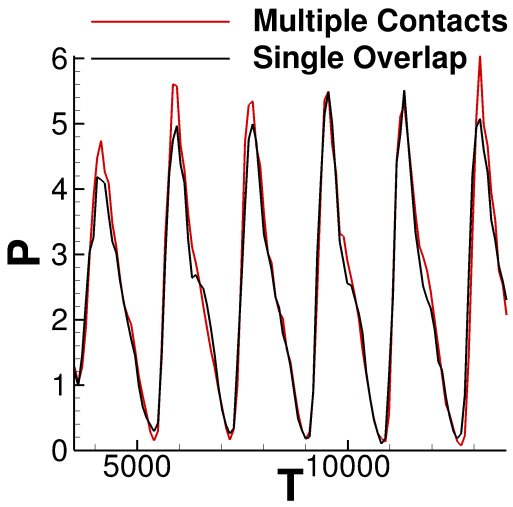

Figure 7.3 Pressure on the top and bottom walls during the shear of the 3D granular system.

$$P = \frac{1}{A_t + A_b} \sum_{p \in \{w_t,\ w_b\}} |\mathbf{F}_{\mathrm{p}}^{\mathrm{n}}| \tag{7.3}$$

where $\{w_t,\ w_b\}$ and $A_t,\ A_b$ denote the set of the wall particles and the areas of the top and bottom walls, respectively (in this geometry, $A_t = A_b$). The total normal force on the particle p is denoted by $\mathbf{F}_{\mathrm{p}}^{\mathrm{n}}$; recall that the wall particles do not interact with each other, therefore the force $\mathbf{F}_{\mathrm{p}}^{\mathrm{n}}$ is non-zero only if there is a system particle colliding with the particle p.

The pressure on the top and bottom wall for the different force models is not significantly different. In the case when the pressure assumes its local maximum, the observed amplitude is slightly larger in the case of the MC force model. Therefore, we conclude that the pressure on the walls in not strongly dependent on the models used.

In this chapter, we presented preliminary results of simulations of sheared granular system in 3D. In particular, we compared two different force models and discussed their influence on the system pressure during bi-axial shear. The main

finding is that for the considered material parameters and shearing rates, there are no significant differences for the force models considered.

The formulation of 3D simulations now opens the door for considering the properties of force networks in this more realistic geometry. The analysis of force networks in 3D along the lines discussed in Chapters 3-6 will provide significant new information both about the properties of force networks, and about physical properties of the underlying granular systems. Such analysis is left for future work.

CHAPTER 8

SUMMARY AND CONCLUSIONS

In this work, we focus on the analysis and numerical simulations of the dense granular systems, ranging from the one dimensional (1D) chain of the particles to the 2D and 3D systems under compression and shear.

In Chapter 2, we discuss wave propagation from an initial impulse in a granular stochastic chain, where the randomness is introduced in the particle masses. Specifically, the initial impulse propagates as a wave with additional noise characterized by $\epsilon\sqrt{\eta}N(0,1)$, with the parameter ϵ measuring the magnitude of the randomness of the masses and η characterizes the spatial scale of the randomness. Our results, obtained jointly with prof. Bal from Columbia University, set a stage for future work that should consider in more detail the influence of η and ϵ on the wave propagation, both in 1D considered here, and in higher dimensions.

Chapters 3 - 6 focus on 2D systems, and in particular on the properties of force networks in these systems. Specifically, in Chapter 3 we consider percolation and jamming transitions during compression. One significant and new finding is that, for repulsive systems, the two transitions converge to one in the quasistatic limit. This convergences, however, disappears in the presence of a non-vanishing shear rate. The fact that the transitions differ even for very small shear rates suggests that in any evolving system differences between these transitions may be observed. Furthermore, if additional attractive interaction between the particles is included, we find that the percolation and jamming transitions occur for significantly different packing fractions. It will be of interest to explore whether and how these findings propagate to the 3D geometries.

In Chapter 4, the force networks in compressed granular systems are further studied by analyzing the numbers and sizes of the clusters composed of the contacts in a force network involving the forces above given force threshold, f_{th}. As we vary f_{th}, the mean cluster size, S, evolves. We find that S rescales to the same universal "master" curve for the systems made out of frictional particles, in agreement with the existing results. However, universality is found to disappear for the systems of particles with different friction or a different level of structural disorder. Our results suggest that frictionless and ordered systems are a part of different scaling class than the disordered frictional ones.

Chapter 5 considers sheared granular systems, that go through shear jamming (or jamming by shear) transition. We find that jamming by shear occurs only for systems characterized by sufficiently large packing fraction. For such systems, we have performed a direct comparison of the numerical results with the experimental ones (carried out by the experimental group at Duke University led by prof. Behringer) and find a good agreement when either microscopic (such as contact numbers) or system wide (such as the pressure or stress anisotropy) are considered. To reach a good agreement on mesoscale, however, we have discovered that we need to include the fact that the experimental results include a certain degree of noise. With the noise added, the topological measures, in particular the first two Betti numbers, show a reasonable degree of agreement between the experimental and computational results. The topological analysis has been carried out jointly with the collaborative group at Rutgers University, let by prof. Mischaikow. We hope that this work, that provides first direct comparison of the properties of force networks in experiments and simulations, will lead to further research projects considering this comparison for other systems, both in 2D and 3D.

Chapter 6 discuses the source of energy loss in sheared granular systems for the particles that interact by either purely repulsive forces (typical for dry granular

systems) or by repulsive/attractive forces, that are relevant for wet granular particles, for which attractive forces result from cohesion due to capillary bridges that form as particles get in contact. The question is whether the energy is lost due to breakup of the capillary bridges, or due to other loss mechanisms, such as particle inelasticity and friction. To answer these questions, we simulate the systems both with and without cohesive effects, and find significant influence of cohesive effects on energy loss. The simulations results are found to compare favorably with the experiments carried out by the collaborative group at Saarlandes University led by prof. Seemann. This research project, still in progress, aims to further quantify the importance of cohesion in the systems exposed to variable external pressure.

Chapter 7 discusses modeling granular systems in 3D, and in particular the influence of multiple simultaneous collisions on particle dynamics and global system evolution. We have considered both established models, that treat each collision independently, and the newly proposed one, that accounts for interaction between collision events. Our finding is that, at least for the regimes considered, and for the quantities computed, the differences between the models are minor. However, the question of the influence of modeling techniques on the results in other settings, or their influence on the properties of underlying force networks remains open. More generally, the simulation setup that we prepared now allows for detailed analysis of the properties of force networks in three spatial dimensions.

APPENDIX A

FORCE MODEL

System particles are either soft inelastic spheres when we perform the simulations in 3D or disks in 2D case. The particles interact via normal and tangential forces, including static friction, μ (as in [35, 38]). The particle-particle (and particle-wall) interactions include normal and tangential components. Note, that the linear and non-linear model presented here is valid in both 2D and 3D.

The normal force between particles i and j is considered to be either linear (based on the Hooke's law and denoted by $\mathbf{F}_{\rm hl}$), or non-linear (based on the Hertz's law and denoted by $\mathbf{F}_{\rm hz}$).

A.1 Linear Force Model

For the linear force model, the normal force between the particles during the collision is

$$\begin{aligned} \mathbf{F}^{\rm n}_{\rm hl,i,j} &= k_n \delta \mathbf{n} - \gamma_n \bar{m} \mathbf{v}^n_{i,j} \qquad \text{(A.1)} \\ r_{i,j} = |\mathbf{r}_{i,j}|, \quad \mathbf{r}_{i,j} &= \mathbf{r}_i - \mathbf{r}_j, \quad \mathbf{n} = \mathbf{r}_{i,j}/r_{i,j} \end{aligned}$$

where $\mathbf{v}^n_{i,j}$ is the relative normal velocity. The amount of compression is $\delta = d_{i,j} - r_{i,j}$, where $d_{i,j} = (d_i + d_j)/2$, d_i and d_j are the diameters of the particles i and j. All quantities are expressed using the average particle diameter, d_{ave}, as the lengthscale, the binary particle collision time $\tau_c = 2\pi\sqrt{d_{ave}/(2gk_n)}$ as the time scale, and the average particle mass, m, as the mass scale. $\bar{m}$ is the reduced mass, k_n (in units of mg/d_{ave}) is set to a value corresponding either to photoelastic disks (corresponding to the simulations in 2D) [24] when not specified, or is set to a value given by the experimental measurements depending on the simulated system. γ_n is the damping

coefficient [33]. The parameters entering the force model can be connected to physical properties (Young modulus, Poisson ratio) as described e.g. in [33].

We implement the commonly used Cundall-Strack model for static friction [18], where a tangential spring is introduced between particles for each new contact that forms at time $t = t_0$. Due to the relative motion of the particles, the spring length, $\boldsymbol{\xi}$ evolves as $\boldsymbol{\xi} = \int_{t_0}^{t} \mathbf{v}_{i,j}^{t}\ (t')\ dt'$, where $\mathbf{v}_{i,j}^{t} = \mathbf{v}_{i,j} - \mathbf{v}_{i,j}^{n}$. For long lasting contacts, $\boldsymbol{\xi}$ may not remain parallel to the current tangential direction defined by $\mathbf{t} = \mathbf{v_{i,j}^{t}}/|\mathbf{v_{i,j}^{t}}|$ (see, e.g,. [10]); we therefore define the corrected $\boldsymbol{\xi'} = \boldsymbol{\xi} - \mathbf{n}(\mathbf{n} \cdot \boldsymbol{\xi})$ and introduce the test force

$$\mathbf{F}_{\mathrm{hl}}^{\mathrm{t*}} = -k_t \boldsymbol{\xi'} - \gamma_t \bar{m} \mathbf{v}_{i,j}^{t} \tag{A.2}$$

where γ_t is the coefficient of viscous damping in the tangential direction (we assume $\gamma_t = \gamma_n$). To ensure that the magnitude of the tangential force remains below the Coulomb threshold, we set the force to the following

$$\mathbf{F}_{\mathrm{hl}}^{\mathrm{t}} = min(\mu|\mathbf{F}_{\mathrm{hl}}^{\mathrm{n}}|, |\mathbf{F}_{\mathrm{hl}}^{\mathrm{t*}}|)\mathbf{F}_{\mathrm{hl}}^{\mathrm{t*}}/|\mathbf{F}_{\mathrm{hl}}^{\mathrm{t*}}| \tag{A.3}$$

and redefine $\boldsymbol{\xi}$ if appropriate.

If the force between the particles is based on the Hertz interaction, then for the total force between the particles

$$\mathbf{F}_{\mathrm{hz}} = \sqrt{\frac{d_i d_j}{d_i + d_j}} \sqrt{\delta} \mathbf{F}_{\mathrm{hl}} \tag{A.4}$$

and for the normal and tangential component of the force

$$\begin{aligned} \mathbf{F}_{\mathrm{hz}}^{\mathrm{n}} =& \sqrt{\frac{d_i d_j}{d_i + d_j}} \sqrt{\delta}\, [(k_n\ \delta\ \mathbf{n}_{ij} - \bar{m}\ \gamma_n\ \mathbf{v}_{ij,n})] \\ \mathbf{F}_{\mathrm{hz}}^{\mathrm{t}} =& min(\mu|\mathbf{F}_{\mathrm{hz}}^{\mathrm{n}}|, |\mathbf{F}_{\mathrm{hz}}^{\mathrm{t*}}|)\mathbf{F}_{\mathrm{hz}}^{\mathrm{t*}}/|\mathbf{F}_{\mathrm{hz}}^{\mathrm{t*}}| \end{aligned}$$

with

$$\mathbf{F}_{\mathrm{hz}}^{\mathrm{t}*} = \sqrt{\frac{d_i d_j}{d_i + d_j}} \sqrt{\delta} \left[(k_t \, \boldsymbol{\xi} + \bar{m} \, \gamma_t \, \mathbf{v}_{ij,t}) \right]$$

APPENDIX B

COHESIVE FORCE MODEL IN THREE DIMENSIONS

Cohesive forces are modeled using the approach outlined in [29], and are assumed to arise from the capillary bridges that form when particles get in contact. The functional form of the force is given by

$$F_b = 2\pi R\gamma \cos\theta/(1 + 1.05\hat{s} + 2.5\hat{s}^2) \tag{B.1}$$

where $\hat{s} = s\sqrt{R/V}$ and $s = r_{ij} - (d_i + d_j)/2$ (taken to be ≥ 0) is the particle separation. Here, $1/R = 1/2(1/d_1 + 1/d_2)$ [79] (for simplicity we do not account here for polydispersity and use $d_1 = d_2 = 1$ in dimensionless units), and V is the volume of a capillary bridge between particles. In the present work we assume that all capillary bridges are of the same volume. For contact angle, θ, we use $\theta = 12^\circ$, comparable to the value for (deionized ultra-filtered) water and (clean) glass [26]. For the surface tension, γ, we use the value corresponding to water, 72 dyn/cm, scaled appropriately. The critical separating distance, s_c, at which a bridge breaks is given by [29]

$$s_c = (1 + \theta/2)(V^{1/3}/R + V^{2/3}/R^2) \tag{B.2}$$

APPENDIX C

COHESIVE FORCE MODEL IN TWO DIMENSIONS

Here we focus on developing a 2D model of cohesive interaction between circular particles. A closed form solution is a modification of the capillary force model in 3D between spheres presented in [13].

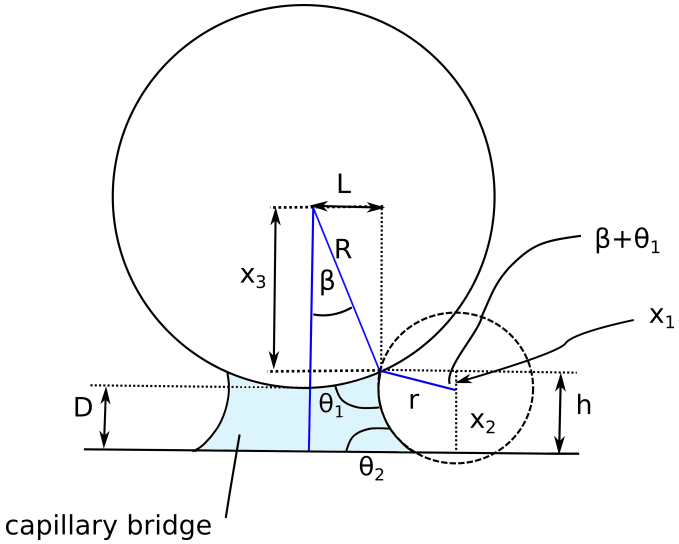

Figure C.1 Scheme of a capillary bridge formed between the particle and a plane. θ_1, θ_2 are the contact angles between the liquid and particle and liquid and a plane, respectively.

We start by considering the capillary force between the circle and a half-plane and find a model for the cohesive force; later we use this model to find the cohesive force between two circular particles with possibly different radii. Figure C.1 shows a 2D circular particle, half-plane and the cohesive bridge between the particle and a plane. We denote the contact angles between the particle and liquid and half-plane and liquid by θ_1, θ_2 , respectively. The radius of the particle is denoted by R and the radius of the liquid surface curvature and surface tension are denoted by r and γ, respectively. The angle β is the angle between the line through the particle center

perpendicular to the half-plane and the line through the particle center and the point of the contact of the particle, air and liquid.

In the modeling the cohesive force, we make the following assumptions. First, we assume that the liquid content with the area denoted by A is small (as specified below) which means that β is small (≈ 0) and the radius of the liquid curvature, $r \ll R$. In our model, we assume that $A^2 \ll 32 S_d^3 R$ where S_d is a critical separating distance at which the cohesive bridge between particles breaks; we make this assumption to simplify our computations of S_d. Hence, the cohesive force model is valid whenever and $A \ll 2^8/3R^2[\cos(\theta_1) + \cos(\theta_2)]$.

We start by finding the Laplace pressure ΔP between the particle/plane and the liquid due to the surface tension

$$\Delta P = \gamma(-1/r) \tag{C.1}$$

The negative sign in front of $1/r$ is due to the concavity of the liquid surface since we assume that the contact angles $\theta_1,\ \theta_2 \leq \pi/2$. The overall Laplace pressure is therefore negative, which means that the pressure in the liquid is smaller than in the air. The Laplace pressure acts upon the cross-section of the liquid area; at the point of contact of the particle, liquid and air, the length of the cross-section is $2L$. The capillary force acting on the particle at this point is

$$\begin{aligned} F_{lap} &= -2L\Delta P \\ &= \frac{\gamma}{r} 2L \\ &= 2\frac{\gamma}{r} R \sin(\beta) \end{aligned} \tag{C.2}$$

The force due to the surface tension, γ, acts upon the point of the contact of the liquid and particle in the direction tangent to the liquid [75], given by $\cos(\pi/2 - \theta_1 - \beta) = \sin(\theta_1 + \beta)$. The resulting force is

$$F_{st} = \gamma \sin(\theta_1 + \beta) \tag{C.3}$$

and the total cohesive force is the sum of the force due to the Laplace pressure and surface tension

$$F_c = F_{lap} + F_{st} = 2\gamma\left[\frac{R}{r}\sin(\beta) + \sin(\theta_1 + \beta)\right] \tag{C.4}$$

In order to obtain a closed-form expression for the capillary force, we first need to find β in terms of the known quantities. From Figure C.1

$$\begin{aligned} h &= x_1 + x_2 \\ x_1 &= r\cos(\beta + \theta_1) \\ x_2 &= r\cos(\theta_2) \\ \Rightarrow h &= r(\cos(\theta_2) + \cos(\beta + \theta_1)) \end{aligned} \tag{C.5}$$

For the distance h we also have

$$\begin{aligned} h &= R + D - x_3 \\ x_3 &= R\cos(\beta) \\ \Rightarrow h &= R(1 - \cos(\beta)) + D \end{aligned} \tag{C.6}$$

From Equations C.5 and C.6

$$r = \frac{R(1 - \cos(\beta)) + D}{\cos(\theta_1) + \cos(\theta_2 + \beta)} \tag{C.7}$$

If we set $c = (\cos(\theta_1) + \cos(\theta_2))/2$ and assume that $\beta \ll 1$ such that $\cos(\beta + \theta_1) \approx \cos(\theta_1)$, we find

$$1 - \cos(\beta) = \frac{2rc - D}{R} \tag{C.8}$$

$$\begin{aligned} \Rightarrow \cos^2(\beta) &= \left[1 - \frac{2rc - D}{R}\right]^2 \\ &\approx 1 - \frac{4rc - 2D}{R} \end{aligned} \tag{C.9}$$

In the last equation we assumed that $x = (2rc - D)/R \ll 1$. Equation C.4 then gives

$$F_c = 2\gamma\left(\frac{R}{r} + c\right)\sqrt{\frac{4rc - 2D}{R}} + 2\gamma\frac{R - 2rc + D}{R}\sqrt{1 - c^2} \tag{C.10}$$

In the following, we use the assumption that the time required for a liquid bridge to

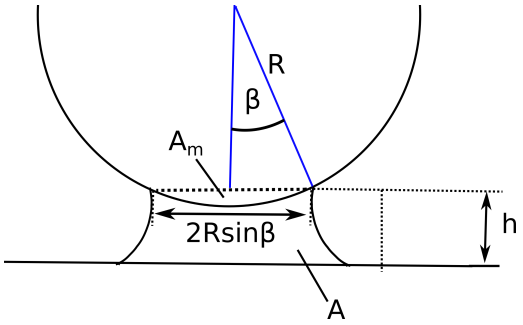

Figure C.2 Cohesive bridge liquid area between the circular particle and a half-plane.

evaporate is much larger than a time scale on which particle separates. Therefore, the area of the liquid bridge, A, is a constant. A is estimated as an area of the rectangle with the length $2R\sin(\beta)$ and height h minus the area of the meniscus of the particle, $A_m = R^2[\beta - \sin(\beta)\cos(\beta)]$. We neglect the fact that the bridge is curved, since the menisci of the liquid bridge are small. We find the expression for A

$$\begin{aligned}
A &= 2hR\sin(\beta) - A_m \\
&= 2hR\sin(\beta) - R^2[\beta - \sin(\beta)\cos(\beta)] \\
&= 2\underbrace{[R(1-\cos(\beta)) + D]}_{h} R\sin(\beta) - R^2\beta + R^2\sin(\beta)\cos(\beta) \\
&= 2R^2\sin(\beta) - 2R^2\sin(\beta)\cos(\beta) + 2DR\sin(\beta) - R^2\beta + R^2\sin(\beta)\cos(\beta) \\
&= R^2(2\sin(\beta) - \beta - \sin(\beta)\cos(\beta)) + 2DR\sin(\beta) \\
&= R^2\left(2\sin(\beta) - \beta - \sin(\beta)\sqrt{1 - \sin^2(\beta)}\right) + 2DR\sin(\beta) \\
&\approx R^2[2\sin(\beta) - \sin(\beta) - \sin(\beta)(1 - 1/2\sin^2(\beta))] + 2DR\sin(\beta)
\end{aligned} \tag{C.11}$$

In the last equation we used the fact that for $\beta \ll 1$ we have $\beta \approx \sin(\beta)$ and for $x \ll 1$ we can write $\sqrt{1-x^2} \approx 1 - x^2/2$.

Finally,

$$A = 1/2R^2 \sin^3(\beta) + 2DR\sin(\beta) \tag{C.12}$$

Now, let k be defined by the following equation

$$1/2R^2 \sin^3(\beta) = k2DR\sin(\beta) \tag{C.13}$$

Since β is assumed to be small and is always non-zero for $A > 0$, we have that $\sin(\beta) > 0$. Here we assume that D is non-zero such that k always exists and $k > 0$ (we will discuss the case when $D = 0$ later in the section). From Equation C.13

$$\begin{aligned} D &= \frac{1}{4k} R \sin^2(\beta) \\ &= \frac{1}{4k} R \frac{4rc - 2D}{R} = \frac{2rc - D}{2k} \end{aligned} \tag{C.14}$$

From the previous Equation

$$\begin{aligned} \frac{2k+1}{2k} D &= \frac{rc}{k} \\ \Rightarrow D &= \frac{2rc}{2k+1} \end{aligned} \tag{C.15}$$

After substitution of D in the expression for $\sin(\beta)$ in Equation C.11, we can rewrite the area, A, as

$$\begin{aligned} A &= \overbrace{1/2R^2 \sin^3(\beta)}^{2kDR\sin(\beta)} + 2DR\sin(\beta) \\ &= 2(k+1)DR\sin(\beta) \\ &= 2(k+1)\frac{2rc}{2k+1} R \sqrt{\frac{8krc}{R(2k+1)}} \end{aligned} \tag{C.16}$$

For the squared area A we find

$$A^2 = \frac{4^2 2^3 k(k+1)^2 r^3 c^3 R}{(2k+1)^3}$$

We use the last expression to find the curvature of the liquid bridge

$$r = \frac{A^{2/3}(2k+1)}{4^{2/3}2k^{1/3}(k+1)^{2/3}cR^{1/3}} \tag{C.17}$$

and for the capillary force, we have the following

$$F_c = 2\gamma\left[\sqrt{\frac{8Rkc}{r(2k+1)}} + \sqrt{\frac{8krc^3}{R(2k+1)}} + \sqrt{1-c^2}\left(1 - \frac{4krc}{R(2k+1)}\right)\right] \tag{C.18}$$

Now we need to express k in the terms of known quantities, A, D, R. From the definition of k we have

$$k = \frac{2R}{D4^{5/3}}\frac{k^{2/3}}{(k+1)^{2/3}A^{2/3}R^{-4/3}} \tag{C.19}$$

In the last equation, we made a substitution for $\sin(\beta)$ and r, D. After some algebra, we obtain the following quadratic equation

$$k^2 + k - \frac{A^2}{2^7D^3R} = 0$$

which leads to the solution for k

$$k = -1/2 \pm 1/2\sqrt{1 + \frac{A^2}{32D^3R}} \tag{C.20}$$

In the last expression we choose the positive solution, since Equation C.13 does not allow $k \leq 0$ for $\sin(\beta) > 0$. We substitute Equations C.20 and C.17 into Equation C.18 to obtain the final expression for the cohesive force between the particle and a plane

$$\begin{aligned} F_c &= \frac{8A^{1/3}(-\sqrt{32D^3R} + \sqrt{A^2+32D^3R})^{1/3}c\gamma R^{2/3}}{2^{1/3}\sqrt{32D^3R+A^2}} \\ &+ 2\gamma\left[B\sqrt{2c^3} + (B^2-1)\sqrt{1-c^2}\right] \end{aligned} \tag{C.21}$$

where

$$B = \frac{2^{1/3}(-\sqrt{32D^3R} + \sqrt{A^2+32D^3R})^{2/3}}{2^{1/2}R^{2/3}A^{1/3}}$$

Recall that in the derivation of the cohesive force we assumed that $D > 0$. In the case when the distance between the plane and the particle is zero, we simply put $D = 0$ in the Equation C.21.

C.1 Two Circular Particles

In the preceding section, we compute the cohesive force between a circular particle and a plane. Now, we find the force between two circular particles with possibly different radii. When the two particles have radii R_1, R_2, we can use Equation C.21 with R^* being the effective radius [13] defined by

$$R^* = \frac{R_1 R_2}{R_1 + R_2} \tag{C.22}$$

Moreover, $\cos(\theta_1) = \cos(\theta_2) = \cos(\theta)$, since we assume that the particles have the same wetting properties. The capillary force between two particles is given by

$$\begin{aligned} F_c &= \frac{8A^{1/3}\left(-1/2\sqrt{32D^3R^*} + 1/2\sqrt{A^2 + 32D^3R^*}\right)^{1/3}\cos(\theta)\gamma R^{*2/3}}{\sqrt{32D^3R^* + A^2}} \\ &+ 2\gamma\left[B^*\sqrt{2\cos(\theta)^3} + (B^{*2} - 1)\sin(\theta)\right] \end{aligned} \tag{C.23}$$

where

$$B^* = \frac{2^{1/3}(-\sqrt{32D^3R^*} + \sqrt{A^2 + 32D^3R^*})^{2/3}}{2^{1/2}R^{*2/3}A^{1/3}}$$

C.2 Separating Distance

In the model of the cohesive interaction, we assume that the cohesive bridges form after the particles come into a contact. After the formation of a bridge, the particles can separate while the cohesive bridge is still present. After the particles separate by a sufficient distance, the bridge breaks. The simplest way to compute the critical separating distance at which the bridge breaks, is to assume that at such distance, the "neck" of the bridge has a zero width.

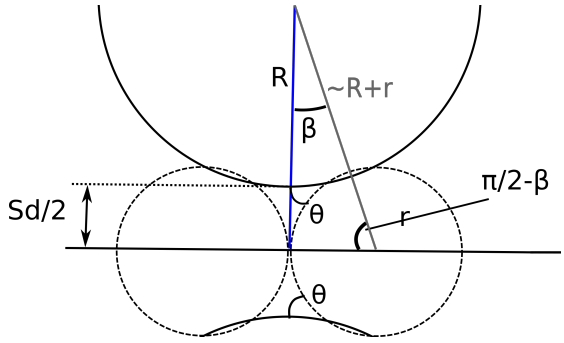

Figure C.3 Two particles at the critical separating distance, S_d.

Figure C.3 shows two particles at the critical separating distance at which the bridge breaks, denoted by S_d. Recall, that θ is the contact angle between the particle and liquid. To find the value of S_d, we use the trigonometric sine identity

$$\frac{R + S_d/2}{\sin(\pi/2 - \beta)} = \frac{r}{\sin(\beta)} \tag{C.24}$$

$$\frac{R + S_d/2}{\cos(\beta)} = \frac{r}{\sin(\beta)} \tag{C.25}$$

We assume that the line connecting the center of the particle and center of the liquid curvature is $\approx R + r$ and $\beta \ll 1$ which yields $\cos(\beta) \approx 1$ and for the sine of β

$$\sin(\beta) \approx \frac{r}{R + r} \tag{C.26}$$

Substitution of Equation C.26 into Equation C.12 yields

$$\begin{aligned} A &= R^2 1/2 \frac{r^3}{(R+r)^3} + 2S_d R \frac{r}{R+r} \\ &\approx \frac{2S_d R r}{R+r} \\ &\approx 2S_d r \end{aligned} \tag{C.27}$$

In the last two equations we used the fact that $r \ll R$. From the Equation C.27 we have

$$S_d = \frac{A}{2r} = \frac{A 4^{2/3} 2k^{1/3}(k+1)^{2/3}\cos(\theta) R^{1/3}}{2A^{2/3}(2k+1)}$$

If we now substitute for k and simplify the expression for S_d, we obtain

$$\begin{aligned} S_d &= A2^{2/3}R^{1/3}\frac{\cos(\theta)}{(32S_d^3R+A^2)^{1/3}} \\ \Rightarrow S_d^3 &= \frac{4A^3R\cos(\theta)}{32RS_d^3+A^2} \end{aligned} \tag{C.28}$$

In the last set of equations, we assume that $A^2 \ll 32S_d^3R$ such that we can approximate $\sqrt{32S_d^3R} \approx \sqrt{32S_d^3R+A^2}$ (calculations not shown for brevity). Let us denote $Y = S_d^3$. Then we solve for the following quadratic equation

$$\begin{aligned} 32Y^2R + A^2Y &= 4A^3R\cos(\theta) \\ Y &= \frac{-A^2}{64R} + 1/2\sqrt{\frac{A^4}{2^{10}R^2} + \frac{A^3\cos(\theta)}{2}} \\ \Rightarrow S_d &= \left[\frac{-A^2}{64R} + 1/2\sqrt{\frac{A^4}{2^{10}R^2} + \frac{A^3\cos(\theta)}{2}}\right]^{1/3} \end{aligned} \tag{C.29}$$

In the last equation, we choose the positive solution.

Recall that we assume that $r \ll R$ and $A^2 \ll 32S_d^3R$. These assumptions yield

$$A \ll \frac{2^9}{3}\cos(\theta)R^2 \tag{C.30}$$

Using the Inequality C.30, we can immediately check whether the parameters in the simulations satisfy such condition and if the cohesive force model is thus valid.

Figure C.4(a) shows the cohesive force as a function of the distance between particles, D, up to a critical separating distance, S_d, for different values of contact angle $0 \leq \theta < \pi$. The cohesive force, F_b, separating distance, D, and liquid area, A, are shown in dimensionless units and $A = 0.01R^2$. The scales in the force model, d_{ave}, τ_c and m are set to the corresponding values used in Section 6.3. We notice that the cohesive force decreases with the increasing contact angle, which is expected since we are approaching $\theta = \pi/2$; when $\theta > \pi/2$, the liquid bridge is convex and the resulting force is repulsive.

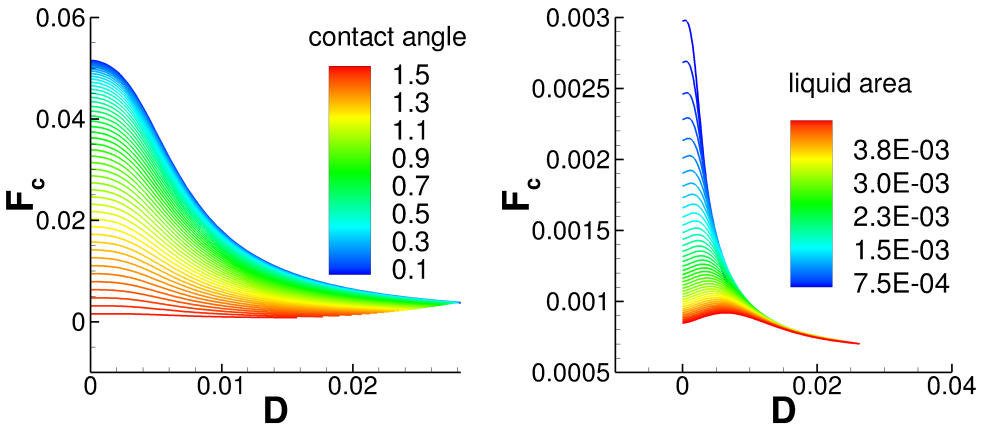

(a) (b)

Figure C.4 (a) Cohesive force, F_c, for different contact angles θ (expressed in radians) for $A = 0.01R^2$ and (b) F_c for varying liquid area, A, with $\theta = 0.49\pi$ as a function of the separating distance, D.

Figure C.4(b) shows the cohesive force for varying liquid area when $\theta = 0.45\pi$. This value of θ was chosen to show that the cohesive force model admits a solution that is non-monotonous as in [75]. We note that the larger amount of liquid results in a maximum in F_c for larger separating distances D. In [75], the force is found by taking a derivative of the computed energy of the capillary bridge and so the functional form is different from that presented here. The results in [75] are shown for the amount of liquid that is typically large (the value of r is $\approx R/4$) compared to the case analyzed in this section. Therefore, we do not aim to directly compare our force model with the one presented in [75].

In comparison with the model of cohesive interaction in 3D (see Appendix B), it is important to note that in 3D, the cohesive force is not dependent on the liquid volume when the particle separating distance $S_d = 0$. Therefore, the cohesive interactions in 2D and 3D are essentially different. To obtain a cohesive force that would be comparable in 2D and 3D, we would need to pick a specific value of A.

The reasoning behind the fact that in 3D the cohesive force does not depend on the liquid volume [29] is the following. For the complete wetting, defined such that

$\theta = 0$, the radius of the liquid curvature $r = L^2/(2R)$. The cohesive force is then $F_c \approx \pi L^2 \Delta P$, since the Laplace pressure is acting on the area of the particle with the radius L. Under assumption $L \gg r$, we have $\Delta P \approx \gamma/r$ and the cohesive force then becomes $F_c = 2\pi R\gamma$. In 2D we have $F_c = -2L\Delta P$ for $S_d = 0$ with $\Delta P = -\gamma/r$ and $r = L^2/(2R)$ for complete wetting. The final form of the force is $F_c = 4\gamma R/L$ which is dependent on L and therefore on the liquid area.

APPENDIX D

HIERARCHY OF THE CODE FOR THE SIMULATIONS OF THE GRANULAR MATTER IN THREE DIMENSIONS

The code for the numerical simulations in 3D is written in Fortran version 90 and implements techniques partially resembling object oriented programming. The code is divided into several parts and includes modules and functions.

Figure D.1 shows the structure of the directory for the code. The directory `BUILD` is used as a destination for temporary files during the compilation of the code. Directory `details` contains descriptions of the various force models and important modifications and additions to the code; directory `postprocessing` contains the codes used to post-process the basic output from the code. In the directory `develop`, we have the codes that are currently under development and directory `examples` contains tested codes that can be immediately run and serve as the basic examples of different geometries. The most crucial directory is the directory `src` that contains all source files used to compile and run the simulations. There are three subdirectories:

- `Common`: contains all the code files that are common for simulations in both serial and parallel type of processing.
- `MPI/OpenMPI`: contains the codes that are compiled when user wants to run a parallel code.
- `Serial`: contains the codes that are compiled when running the code in serial.

D.1 Compiling the 3D Code

To compile the code, we have several options: we can compile the code written to support parallel computing, or serial computing. Then, we can specify the code that

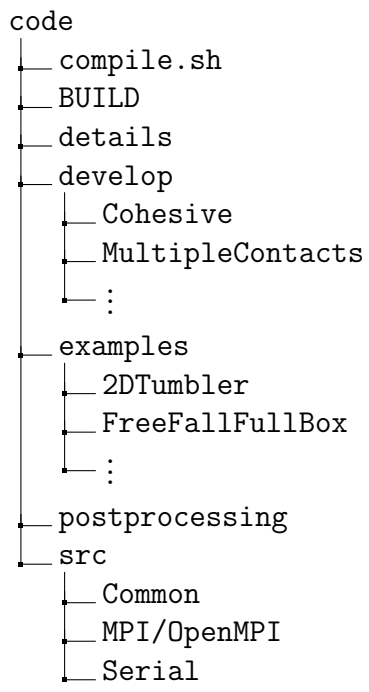

Figure D.1 3D granular particle simulations: code directory structure.

is compiled - for example, if we want to run the simulations for a 2D tumbler from examples, we need to specify the folder such that the compiler fetches the codes from the corresponding directory `examples/2DTumbler`. This folder contains either modified codes present in the `src/Common` directory, or some extra codes needed for specific purposes of the current simulation. Then the script in `compile.sh` compares the files in `Common` with the files in `examples/2DTumbler` and uses only the proper version. Example of compiling the code: `./compile serial examples/2DTumbler` The executable file is present in the `examples/2DTumbler` folder.

BIBLIOGRAPHY

[1] E. Aharonov and D. Sparks. Rigidity phase transition in granular packings. *Physical Review E*, 60:6890, 1999.

[2] S. Alexander. Amorphous solids: Their structure, lattice dynamics and elasticity. *Physics Reports*, 296:65, 1998.

[3] R. Arévalo, L. A. Pugnaloni, I. Zuriguel, and D. Maza. Contact network topology in tapped granular media. *Physical Review E*, 87:022203, 2013.

[4] R. Arévalo, I. Zuriguel, and D. Maza. Topology of the force network in jamming transition of an isotropically compressed granular packing. *Physical Review E*, 81:041302, 2010.

[5] R. A. Bagnold. *The Physics of Blown Sand and Desert Dunes*. Methuen, London, Great Britain, 1941.

[6] D. S. Bassett, E. T. Owens, K. E. Daniels, and M. A. Porter. Influence of network topology on sound propagation in granular materials. *Physical Review E*, 86:041306, 2012.

[7] R. P. Behringer, D. Bi, B. Chakraborty, A. Clark, J. Dijksman, J. Ren, and J. Zhang. Statistical properties of granular materials near jamming. *Journal of Statistical Mechanics: Theory and Experiment*, 2014:06004, 2014.

[8] D. Bi, J. Zhang, B. Chakraborty, and R. P. Behringer. Jamming by shear. *Nature*, 480:355358, 2011.

[9] D. L. Blair, N. W. Mueggenburg, A. H. Marshall, H. M. Jaeger, and S. R. Nagel. Force distributions in three-dimensional granular assemblies: Effects of packing order and interparticle friction. *Physical Review E*, 63:041304, 2001.

[10] L. Brendel and S. Dippel. *Lasting Contacts in Molecular Dynamics Simulations*. Kluwer Academic Publishers, Dordrecht, Netherlands, 1998.

[11] N.V. Brilliantov and T. Pöschel. Rolling as a "continuing collision". *European Physical Journal B*, 12:299, 1999.

[12] N. Brodu, J. A. Dijksman, and R. P. Behringer. Multiple-contact discrete-element model for simulating dense granular media. *Physical Review E*, 91:032201, 2015.

[13] H.-J. Butt and M. Kappl. *Surface and Interfacial Forces*. Wiley, Weinheim, Germany, 2010.

[14] R. Carretero-Gonzalez, D. Khatri, M. A. Porter, P. G. Kevrekidis, and C. Daraio. Dissipative solitary waves in granular crystals. *Physical Review Letters*, 102:024102, 2009.

[15] X. Cheng. Experimental study of the jamming transition at zero temperature. *Physical Review E*, 81:031301, 2010.

[16] A. H. Clark, L. Kondic, and R. P. Behringer. Particle scale dynamics in granular impact. *Physical Review Letters*, 109:238302, 2012.

[17] A. H. Clark, A. J. Petersen, L. Kondic, and R. P. Behringer. Nonlinear force propagation during granular impact. *Physical Review Letters*, 114:144502, 2015.

[18] P. A. Cundall and O. D. L. Strack. A discrete numerical model for granular assemblies. *Géotechnique*, 29:47, 1979.

[19] C. Daraio, V.F. Nesterenko, E.B. Herbold, and S. Jin. Energy trapping and shock disintegration in a composite granular medium. *Physical Review Letters*, 96:058002, 2006.

[20] J. A. Dijksman. Wageningen, Netherlands. Private communication, 2016.

[21] J.A. Dijksman, J. Ren, R. P. Behringer, M. Kramár, K. Mischaikow, L. Kovalcinova, and L. Kondic. Characterizing granular networks using topological metrics. In preparation, 2016.

[22] Richard O. Duda and Peter E. Hart. Use of the Hough transformation to detect lines and curves in pictures. *Communincations ACM*, 15:11, 1972.

[23] Z. Fournier, D. Geromichalos, S. Herminghaus, M. M. Kohonen, F. Mugele, M. Scheel, M. Schulz, B. Schulz, Ch. Schier, R. Seemann, and A. Skudelny. Mechanical properties of wet granular materials. *Journal of Physics: Condensed Matter*, 17:S477, 2005.

[24] J. Geng, R. P. Behringer, and G. Reydellet. Green's function measurements of force transmission in 2D granular materials. *Physica D*, 182:274, 2003.

[25] C. Goldenberg and I. Goldhirsch. Friction enhances elasticity in granular solids. *Nature*, 435:188, 2005.

[26] Y. Gu. Glass surfaces: Electrokinetic and wetting properties. In P. Somasundaran, editor, *Encyclopedia of Surface and Colloid Science*, volume 4, page 2711. Taylor & Francis, New York, NY, 2nd edition, 2006.

[27] E. Guyon, S. Roux, and A. Hansen. Non-local and non-linear problems in the mechanics of disordered systems: application to granular media and rigidity problems. *Reports on Progress in Physics*, 53:373, 1990.

[28] S. Henkes, C. S. O'Hern, and B. Chakraborty. Entropy and temperature of a static granular assembly: An ab initio approach. *Physical Review Letters*, 98:038002, 2007.

[29] S. Herminghaus. Dynamics of wet granular matter. *Advances in Physics*, 54:221, 2006.

[30] M. Herrera, S. McCarthy, S. Slotterback, W. Losert, and M. Girvan. Path to fracture in granular flows: Dynamics of contact networks. *Physical Review E*, 83:061303, 2011.

[31] H. J. Herrmann, J.-P. Hovi, and S. Luding, editors. *Physics of dry granular media - NATO ASI Series E 350*. Kluwer Academic Publishers, Dordrecht, Germany, 1998.

[32] S. Karmakar, M. Schaber, A.-L. Hippler, M. Scheel, M. DiMichiel, S. Herminghaus, M. Brinkmann, R. Seemann, L. Kovalcinova, and L. Kondic. Energy dissipation in sheared cohesive granular systems. In preparation, 2016.

[33] L. Kondic. Dynamics of spherical particles on a surface: Collision-induced sliding and other effects. *Physical Review E*, 60:751, 1999.

[34] L. Kondic, X. Fang, W. Losert, C.S. O'Hern, and R.P. Behringer. Microstructure evolution during impact on granular matter. *Physical Review E*, 85:011305, 2012.

[35] L. Kondic, A. Goullet, C.S. O'Hern, M. Kramár, K. Mischaikow, and R.P. Behringer. Topology of force networks in compressed granular media. *Europhysics Letters*, 97:54001, 2012.

[36] L. Kovalcinova, A. Goullet, and L. Kondic. Percolation and jamming transitions in particulate systems with and without cohesion. *Physical Review E*, 92:032204, 2015.

[37] L. Kovalcinova, A. Goullet, and L. Kondic. Scaling properties of force networks for compressed particulate systems. *Physical Review E*, 93:042903, 2016.

[38] M. Kramár, A. Goullet, and L. Kondic. Persistence of force networks in compressed granular media. *Physical Review E*, 87:042207, 2013.

[39] M. Kramár, A. Goullet, L. Kondic, and K. Mischaikow. Evolution of force networks in dense particulate media. *Physical Review E*, 90:052203, 2014.

[40] G. Lois, J. Blawzdziewicz, and C. S. O'Hern. Jamming transition and new percolation universality classes in particulate systems with attraction. *Physical Review Letters*, 100:28001, 2008.

[41] T. S. Majmudar and R. P. Behringer. Contact force measurements and stress-induced anisotropy in granular materials. *Nature*, 435:1079, 2005.

[42] T. S. Majmudar and R. P. Behringer. *Contact forces and stress induced anisotropy.* A. A. Balkema, Leiden, Germany, 2005.

[43] T. S. Majmudar, M. Sperl, S. Luding, and R. P. Behringer. The jamming transition in granular systems. *Physical Review Letters*, 98:058001, 2007.

[44] M. Manciu, S. Sen, and A. J. Hurd. The propagation and backscattering of soliton-like pulses in a chain of quartz beads and related problems. *Physica A*, 274:588606, 1999.

[45] M. Manciu, S. Sen, and A. J. Hurd. Impulse propagation in dissipative and disordered chains with power-law repulsive potentials. *Physica D*, 157:226, 2001.

[46] M. Manjunath, Amnaya P. Awasthi, and Philippe H. Geubelle. Wave propagation in random granular chains. *Physical Review E.*, 85:031308, 2012.

[47] R. M. Miura, C. S. Gardner, and M. D. Kruskal. Korteweg-de Vries equation and generalizations. II. Existence of conservation laws and constants of motion. *Journal of Mathematical Physics*, 9:12041209, 1968.

[48] D. M. Mueth, H. M. Jaeger, and S. R. Nagel. Force distribution in a granular medium. *Physical Review E*, 57:3164, 1998.

[49] V. F. Nesterenko. A new type of collective excitations in a "sonic vacuum". *Acoustics of Heterogeneous Media*, page 228, 1992.

[50] V. F. Nesterenko. *Dynamics of Heterogenous Media.* Springer, New York, NY, 2001.

[51] V.F. Nesterenko. Propagation of nonlinear compression pulses in granular media. *Journal of Applied Mechanics and Technical Physics*, 24:733, 1983.

[52] S. Ostojic, E. Somfai, and B. Nienhuis. Scale invariance and universality of force networks in static granular matter. *Nature*, 439:828, 2006.

[53] S. Ostojic, T. J. H. Vlugt, and B. Nienhuis. Universal anisotropy in force networks under shear. *Physical Review E*, 75:030301, 2007.

[54] R. Pastor-Satorras and M.-C. Miguel. Percolation analysis of force networks in anisotropic granular matter. *Journal of Statistical Mechanics*, 2012:02008, 2012.

[55] J.P. Peters, M. Muthuswamy, J. Wibowo, and A. Tordesillas. Characterization of force chains in granular material. *Physical Review E*, 72:041307, 2005.

[56] F. Radjai, J. J. Moreau, and S. Roux. Contact forces in a granular packing. *Chaos*, 9:544, 1999.

[57] F. Radjai, D. E. Wolf, M. Jean, and J. J. Moreau. Bimodal character of stress transmission in granular packings. *Physical Review Letters*, 80:61, 1998.

[58] A. Réka and A.-L. Barabási. Statistical mechanics of complex networks. *Reviews of Modern Physics*, 74:47, 2002.

[59] A. Rosas and K. Lindenberg. Pulse dynamics in a chain of granules with friction. *Physical Review E.*, 68:041304, 2003.

[60] M. Scheel, R. Seemann, M. Brinkmann, M. Di Michiel, A. Sheppard, B. Breidenbach, and S. Herminghaus. Morphological clues to wet granular pile stability. *Nature Materials*, 7:189, 2008.

[61] M. Scheel, R. Seemann, M. Brinkmann, M. Di Michiel, A. Sheppard, and S. Herminghaus. Liquid distribution and cohesion in wet granular assemblies beyond the capillary bridge regime. *Journal of Physics: Condensed Matter*, 20:494236, 2008.

[62] R. Seemann. Saarbrücken, Germany. Private communication, 2016.

[63] S. Sen, J. Hong, J. Bang, E. Avalos, and R. Doney. Solitary waves in the granular chain. *Physics Reports*, 462:21, 2008.

[64] S. Sen, M. Manciu, and J. D. Wright. Solitonlike pulses in perturbed and driven hertzian chains and their possible applications in detecting buried impurities. *Physical Review E*, 57:2386, 1998.

[65] T. Shen, C. S. O'Hern, and M. D. Shattuck. Contact percolation transition in athermal particulate systems. *Physical Review E*, 85:011308, 2012.

[66] L. E. Silbert. Force heterogeneities in particle assemblies: From order to disorder. *Physical Review E*, 74:051303, 2006.

[67] R. S. Sinkovits and S. Sen. Nonlinear dynamics in granular columns. *Physical Review Letters*, 74:2686, 1995.

[68] C. Song, P. Wang, and H. A. Makse. A phase diagram for jammed matter. *Nature*, 453:629, 2008.

[69] D. Stauffer and A. Aharonov. *Introduction to Percolation Theory.* Taylor & Francis, Philadelphia, PA, 2003.

[70] B. P. Tighe, J. H. Snoeijer, T. J. H. Vlugt, and M. van Hecke. The force network ensemble for granular packings. *Soft Matter*, 6:2908, 2010.

[71] A. Tordesillas, D. M. Walker, G. Froyland, J. Zhang, and R. P. Behringer. Transition dynamics and magic-numberlike behaviour of frictional granular clusters. *Physical Review E*, 86:011306, 2012.

[72] A. Tordesillas, D. M. Walker, and Q. Lin. Force cycles and force chains. *Physical Review E*, 81:011302, 2010.

[73] A. Tordesillas and D. C. S. Walsh. Incorporating rolling resistance and contact anisotropy in micromechanical models of granular media. *Powder Technology*, 124:106, 2002.

[74] T. M. Truskett, S. Torquato, S. Sastry, P. G. Debenedetti, and F. H. Stillinger. Structural precursor to freezing in the hard-disk and hard-sphere systems. *Physical Review E*, 58:3083, 1998.

[75] M. E. D. Urso, C. J. Lawrence, and M. J. Adams. Pendular, funicular, and capillary bridges: Results for two dimensions. *Journal of Colloid and Interface Science*, 220:42, 1999.

[76] A. R. T. van Eerd, W. G. Ellenbroek, M. van Hecke, J. H. Snoeijer, and T. J. H. Vlugt. The contact force distribution in static granular materials. *Phys. Rev. E*, 75:060302, 2007.

[77] D. M. Walker and A. Tordesillas. Taxonomy of granular rheology from grain property networks. *Physical Review E*, 85:011304, 2012.

[78] J. F. Wambaugh. Simple models for granular force networks. *Physica D*, 239:1818, 2010.

[79] C. D. Willett, M. J. Adams, S. A. Johnson, and J. P. K. Seville. Capillary bridges between two spherical bodies. *Langmuir*, 16:9396, 2000.

[80] G. Wypych, ed. *Handbook of Solvents*. ChemTec Publishing, Ontario, Canada, 2001.

[81] J. Zhang, T. S. Majmudar, M. Sperl, and R. P. Behringer. Jamming for a 2D granular material. *Soft Matter*, 6:2982, 2010.